Master's thesis

NTNU
Norwegian University of Science and Technology
Faculty of Natural Sciences
Department of Materials Science and Engineering

Mustafa Stanikzai

The effect of heat treatments on the formation of intermetallic compounds in clad composites of Al-Mg alloys and steel

Cladding of AA5083 and AA6082 with 316L and 355

Master's thesis in MTKJ
June 2019

NTNU
Kunnskap for en bedre verden

Mustafa Stanikzai

The effect of heat treatments on the formation of intermetallic compounds in clad composites of Al-Mg alloys and steel

Cladding of AA5083 and AA6082 with 316L and 355

Master's thesis in MTKJ
June 2019

Norwegian University of Science and Technology
Faculty of Natural Sciences
Department of Materials Science and Engineering

NTNU
Norwegian University of
Science and Technology

Preface

This work is based on activities within the centre for research-based innovation, SFI Manufacturing in Norway and is partially funded by the Research Council of Norway under contract number 237900.

My heartfelt gratitude goes to my supervisors: Ida Westermann and Siri Marthe Arbo for their availability, guidance and patience throughout this project and Bjørn Holmedal for advising me to take this exciting project.

17th June 2019, Trondheim
Mustafa Stanikzai

Abstract

This thesis investigates the formation of intermetallic compounds in aluminium and steel composites. Aluminium alloys AA6082 and AA5083 were cold roll bonded with two types of steel grades: 316L and 355. The dimensions of the samples were in order of 120 × 15 × 1 mm. The samples were stacked in three layers with steel comprising the outer layer and aluminium in the middle. Surface preparations of the samples included degreasing with acetone, wire brushing with a rotating steel wire brush and heat treatment for 10 minutes at 185 °C. The samples were quenched in water immediately after they were fed into rollers. The four combinations were heat-treated at different temperatures and durations. After heat treatments, the samples were cut and moulded into epoxy moulds for characterization.

The Energy dispersive spectroscopy (EDS), electron probe microanalyzer (EPMA), scanning electron microscopy (SEM), nanoindentation, and optical microscopy were used as characterization methods.

Intermetallic phases of the form $FeAl_3$ and Fe_2Al_5 were detected at the intermetallic layer. However, the intermetallic compounds for all combinations were not successfully identified due to thin intermetallic layers and compositional errors caused by the pear-shaped electron beam depth in EDS measurements. Mg and Ni segregation was observed at the interface of steel and aluminium. To find the mechanism behind this observation, TEM and Atom Probe Tomography could be employed.

Aluminium alloy with the highest Si concentration was found to impede the formation of intermetallic compounds. Alloying elements in 316L such as Ni and Cr were observed in the intermetallic phase and had suppressing effect on intermetallic layer growth.

Sammendrag

Denne masteroppgaven undersøker formasjon av intermetalliske komponenter i aluminium- og stålsammensetninger. Aluminiumslegeringer AA6082 og AA5083 ble kaldvalset med to typer stållegeringer: 316L og 355. Dimensjonene av prøvene var i størrelsesorden 120 x 15 x 1 mm. Prøvene ble stablet i tre lags laminater med stål som ytre lag og aluminium i mellom dem. Overflate av prøvene ble først avfettet med aceton, stålbørstet med en roterende stålbørste og forvarmet i 10 minutter ved 185 °C. Prøvene ble bråkjølt i vann rett etter valsing. De fire laminat kombinasjonene ble deretter varmebehandlet ved forskjellige temperaturer og varigheter. Etter varmebehandlingen ble prøvene delt og formet inn i epoxy former for karakterisering.

Energy dispersive spectroscopy (EDS), electron probe microanalyzer (EPMA), scanning electron microscopy (SEM), nanoindentering, og optisk mikroskopi ble brukt som karakteriseringsteknikker.

Intermetalliske faser på formen $FeAl_3$ og Fe_2Al_5 ble detektert på det intermetalliske laget. Identifikasjonen av de intermetalliske komponentene for alle kombinasjonene ble imidlertid ikke vellykket på grunn av tynne intermetalliske lag, og sammensetningsfeil som følge av den pære-formede elektronstråledybden i EDS målingene. Mg og Ni-segeragering ble observert i intermetalliskelaget mellom stål og aluminium. For å finne mekanismen bak observasjonen kan eksempelvis TEM og Atom Probe Tomography benyttes.

Aluminiumlegering med den høyest Si-konsentrasjon ble funnet til å sinke dannelsen av intermetalliske forbindelser. Legeringselementer i 316L, som Ni og Cr, ble observert i intermetalliske fasen og hadde dempende effekt på veksten av intermetalliske fasen.

Contents

Chapter 1.

Introduction

Aluminium 6xxx and 5xxx series offer the top range of strength-to-weight ratio and excellent properties such as formability, corrosion resistance, and weldability. Aluminium alloys from these two series are widely in use for both defence and civil purposes. The primary purpose of their usage is because of their lightweight. It reduces, for example, fuel consumption in cars, they can be used in heat-exchanger and thus their contribution results in decreased CO_2 emissions. Although, there exists many strengthening mechanisms for aluminium like solid solution strengthening, work hardening, and precipitation hardening but their strength is unmatchable to that of steel. Hence, methods for manufacturing materials with the same properties as of steel and lighter becomes imminent.

In the past few decades, the industrial demand for such materials has steered the research towards clad materials of steel and aluminium alloys. These materials combine the properties of both in one material. Their fabrication method is mainly done by solid-state welding, among them the cold roll bonding – which is the main focus of this work. For the automotive and aerospace industry, these composite materials could increase fuel efficiency and reduce fatigue induced damages [1]. The severe plastic deformation during their fabrication method refines the grains in the material, increases strength and retains their ductility in ambient temperature.

Bonding of low carbon steel and pure aluminium is a well-established process in industry [2, 3] but methods for joining aluminium alloys with low carbon steels are still under development. A reliable and dependable adhesion process of steel and aluminium alloys has limited its potential and usage in the industry. Among many welding or bonding processes of clad materials, cold roll bonding (CRB) has proved to reduce detrimental reactions originating in high-temperature welding – due to its lower operating temperature, low cost, and indifference to stringent cleanliness in production environment [4].

The broad consensus on adhesion or bonding mechanism of clad materials in solid-state welding is by film theory [5–7]. A way to measure the functionality and practicality of such bonding is measured by biaxial bending tests and peel tests. Bond strength of clad clean surface materials can be approximated to the applied normal stress [8]. In cold roll bonding, bimetal sheets are stacked together with rivets to ensure alignment, and during severe

plastic deformation the packed sheets are bonded metallurgically together after a threshold reduction in thickness has been achieved.

Several process parameters affect the bond strength. They involve surface preparations and pre and post-rolling heat treatments. This work mainly focuses on post-rolling heat treatments and their effect on the formation of brittle intermetallic compounds (IMC) at the interface. IMCs are detrimental to bond strength. Composite materials joined by CRB working under high thermal load produce sufficient energy for the formation of brittle intermetallic compounds (IMC) which in turn reduces the bond strength. Under peel tests, it has been shown that the crack propagates at the interface of the clad metal – through the brittle IMC layer.

Scope and objective of this thesis

The scope of this project is on the growth of IMCs during heat-treatment of roll bonded materials made with steel and aluminium alloys, specifically steel grades: S355 & 316L with aluminium alloys: AA5083 & AA6082. This work sheds light on different temperature and duration of heat treatments and the average layer of IMC formed at the interface of the samples. The result of this work would deliver material data on these composites, such as temperature and time ranges for the formation of IMCs – a time-temperature-formation diagram. With this data, one can control the thermodynamically unavoidable formation of IMCs at the interface of composite materials joined by CRB. The samples comprised of an aluminium alloy: AA6082 or AA5083, stacked between a steel grade: 316L or S355, which were cold roll bonded in autumn 2018 during the specialisation project. The samples were then cut, heat treated and then analysed.

This work will also look into the influence of the alloying elements found in the different steel grades and aluminium alloys on the IMC formation and growth.

Chapter 2.

Theoretical background and literature review

2.1. Cold roll bonding

Solid-state welding or bonding is a process used to produce coalescence of the faying surfaces at temperatures below the melting point, T_m, of the base metals being joined, without any filler metal [9]. Cold roll bonding is solid-state welding where a pressure is applied by rollers at normal ambient conditions to produce coalescence of metals with substantial plastic deformation at the weld [4].

There are several parameters in the manufacturing procedure affecting the efficiency and usefulness of bond strength in clad materials. They include lattice structure, surface preparations, hardness ratio between the metals, stacking fault energy (SFE) of the materials, symmetrical/asymmetrical rollers, rolling temperature and post-rolling heat treatments [5].

In the subsections below a brief theory on concepts in cold roll bonding and literature survey of current methods and procedures are given.

2.1.1. Bonding mechanism

The widely accepted bonding mechanism in CRB is the film theory [5, 7]. The film theory states that when pressure is applied, the oxide layer, being very brittle breaks. As the specimen is subjected to increasing normal pressure, it deforms in the rolling direction and the oxide unable to follow. Subsequently, islands of oxide layer form and they expose fresh material which is then a prerequisite for the formation of adhesive bonds [7]. When pressure is applied on bimetal strips of dissimilar metals the following is the case [10]:

- Dislocations most favourably oriented with respect to the applied stress start to migrate on their slip planes
- The migration of the slip planes is continued until their loops reach the innermost surface of the oxide film. The oxide film acts as a barrier to their emergence and at the

same time stress concentration of the pile-ups increases

- The pile-ups of dislocations generate new dislocations in the oxide layer, move into pre-existing dislocations or they get relieved by opening of a crack in the oxide layer, depending on its hardness.

All metals, except gold, have an oxide layer comprising of 20 – 100 Ångstroms [10]. The oxide layer in pure aluminium has a hardness of approximately 2150 $kg\,mm^{-2}$. The oxide layer breaks in a brittle manner at tensile strains ranging in between 0.0006 – 0.0008 [7]. As the strain increases, the oxide layer breaks in a brittle tensile manner. The propagation of the crack is observed to be normal to the applied stress. Oxide-free metal is extruded between the crack gaps. The newly formed crack gap area, at a certain deformation, is equal to the surface extension at that deformation. Undoubtedly, the dislocation pile-ups at both sides of the interface would be unlikely to have equal distribution or facing each other each time. Some shear displacement of the two surfaces is therefore required so that the extruding oxide-free metals come into contact.

Shear displacement at the surface of metals is required in CRB because it impairs the continuity of any adsorbed oxygen layer, arising from trapped air, and increases the contact area for the extruded oxide-free metal to bond to the adjacent metal surface.

Since bonding in CRB is obtained by plastic deformation of the metals, it implies that a threshold surface expansion or deformation should be met for the bonding to occur. This threshold deformation is dependent on the metal combination and the temperature of rolling. Since the necessary pressure to both plastic and creep deformation are synergistic [9].

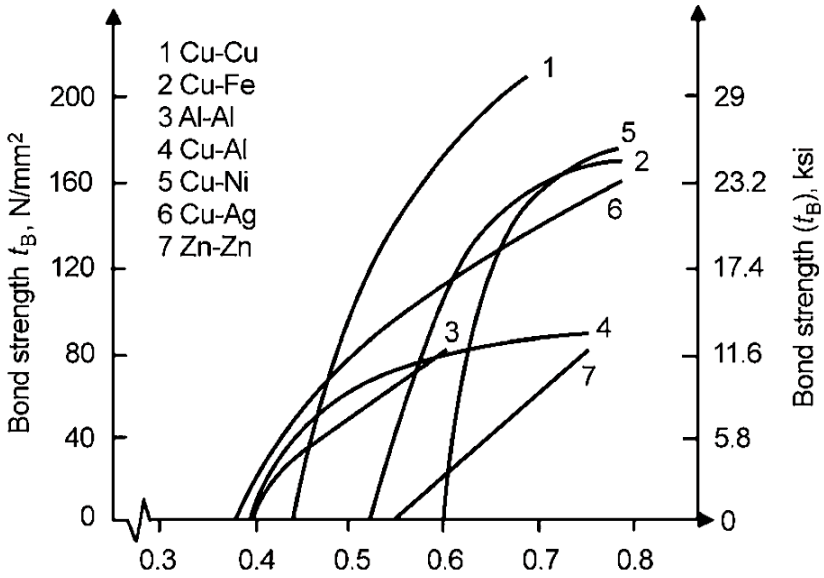

Figure 2.1.: Bond shear strength versus surface reduction in CRB [9].

In face-centred cubic metals (fcc), the formation of partial dislocations, the probability of cross slip, and the formation of twin boundaries are phenomena which are all affected by the stacking fault energy [11]. A material with high SFE has a restricted space between the two Shockley partial dislocations, and therefore separation of the partial dislocations is constrained. [12]. In simpler words, SFE tells about the ability of a metal to deform.

In CRB, the severe plastic deformation facilitates cross-slip and dislocation climb to occur and allows to form three dimensional dislocation substructures like cells or subgrains [13]. Here, the stacking fault energy (SFE) of the metal plays a role in CRB because the higher the SFE, the easier it is for oxide-free metal to extrude or flow between the fragmented oxide layer islands. The ratio of the hardness of metal and its oxide, H_{metal}/H_{oxide}, determines the bond quality since a smaller ratio indicates higher hardness and brittleness of the oxide layer [10].

2.1.2. Surface preparations

Surface preparations have a considerable impact on bond strength. Degreasing the metal surface with acetone to remove contaminants is also beneficial for the bond strength. The thickness of oxide layer has also been shown to affect bond strength. As a consequence, after brushing the surface of aluminium and steel sheets, they should not be exposed to the atmosphere, because it has been shown to decrease bond integrity significantly after 15 minutes [10, 14].

By implementing the broadly used method of scratch brushing with rotating steel brush, immediately before rolling, leaves a heavily work-hardened layer and rough surface. It also removes contaminants from the metal surface like dust particles, grease, moisture and adsorbed ions. Scratch brushing promotes fracture at work hardened surface due to localised plastic deformation on the outer layers. Scratch brushing has been found to produce large scatter in bond strength, due to uneven roughness in preparation of samples [9, 15, 16].

2.1.3. Pre-rolling annealing

Pre-rolling annealing treatment 200–400 °C was found to increase the bond strength between steel and aluminium in the master thesis done by Solhaug [17]. The increase in bond strength can be from the weakening of the bonds between the oxide layer and the parent metal, which facilitates the breakage of the oxide layer and the formability of the oxide-free layer, this way the oxide-free metal is extruded easily through the cracked layer [18].

Another advantage of pre-rolling annealing treatment is reduction in threshold deformation. It is reduced with increasing pre-heating temperature. Results obtained by Nezhad and Ardakani [18] gives weight to the energy barrier theory of bonding mechanism in CRB. They reported that thermal energy (pre-rolling annealing) and plastic deformation provides enough energy to atoms at the interface to overcome the activation energy of bond formation. If thermal energy is increased, the threshold deformation decreases since the atoms at

the interface have already attained activation energy to initiate bonding between the metals [17, 19, 20].

2.1.4. Post-rolling annealing

Post-rolling annealing treatment modifies several characteristics of the rolled composites. It reduces hardness, reduces residual stresses, and promotes atomic diffusion at the interface, through which bond toughness and bond strength are increased. It can also be said that post-rolling annealing treatment completes the bonding between partially bonded extruded material with the adjacent metal. The enhancement of bond strength and toughness are only limited at lower thickness reductions.

The major issue with post-rolling annealing treatments is the formation of intermetallic compounds (IMCs) or brittle phases at the interface. These brittle IMCs has been found to have detrimental effects on bond strength. The formation of IMCs are temperature dependent and depends on the chemical composition of the alloys. Therefore an optimum time and temperature treatment are needed for each composite combination to reduce the extent of their formation [20, 21].

The type and form of IMCs are naturally dependent on the chemical composition of alloys. In the next section, we describe some of the IMCs formed between the major alloying elements of metals discussed in this work. Because of their importance in CRB composites, we have allocated a separate section for them.

2.2. Intermetallic Compounds (IMCs)

Intermetallic compounds or stoichiometric compounds are phases which are formed due to limited solid solubility of one element into the other around a stoichiometric composition. The Hume-Rothery rules well explain the reason for their formation, e.g. the large difference between the electronegativity of the constituent elements [22]. Intermetallic compounds are inherently brittle. Their brittleness is mainly attributed to insufficient deformation modes, low dislocation mobility and high yield strength, lack of cross slip and effects of the environment, among many [23]. The main difference between an alloy and IMC is that the former has a fixed compositional range, a long-range order to the arrangement of atoms within the lattice, and a limited number of slip systems available for plastic deformation [24]. Therefore, control of the formation of these IMCs are essential in improving bond strength.

2.2.1. Intermetallic phases in Fe-Al system

Intermetallic compounds are generally the phases which are formed due to limited solid solubility of one element into the other around a stoichiometric composition. They have a narrow range of homogeneity, narrow compositional ranges, different crystal structure

than their constituents and have simple stoichiometric ratios such as MAl, M_3 Al, MAl_3, and $(M_{1-x}\,Y_x)$ Al [25, 26]. Figure 2.2 shows the binary phase diagram of iron and aluminium. From the phase diagram in 2.2, three phases are present in the Al-rich corner: $FeAl_3$, Fe_2Al_5, $FeAl_2$ and at the Fe-rich corner FeAl and Fe_3Al [27, 28], see Table 2.1 for composition.

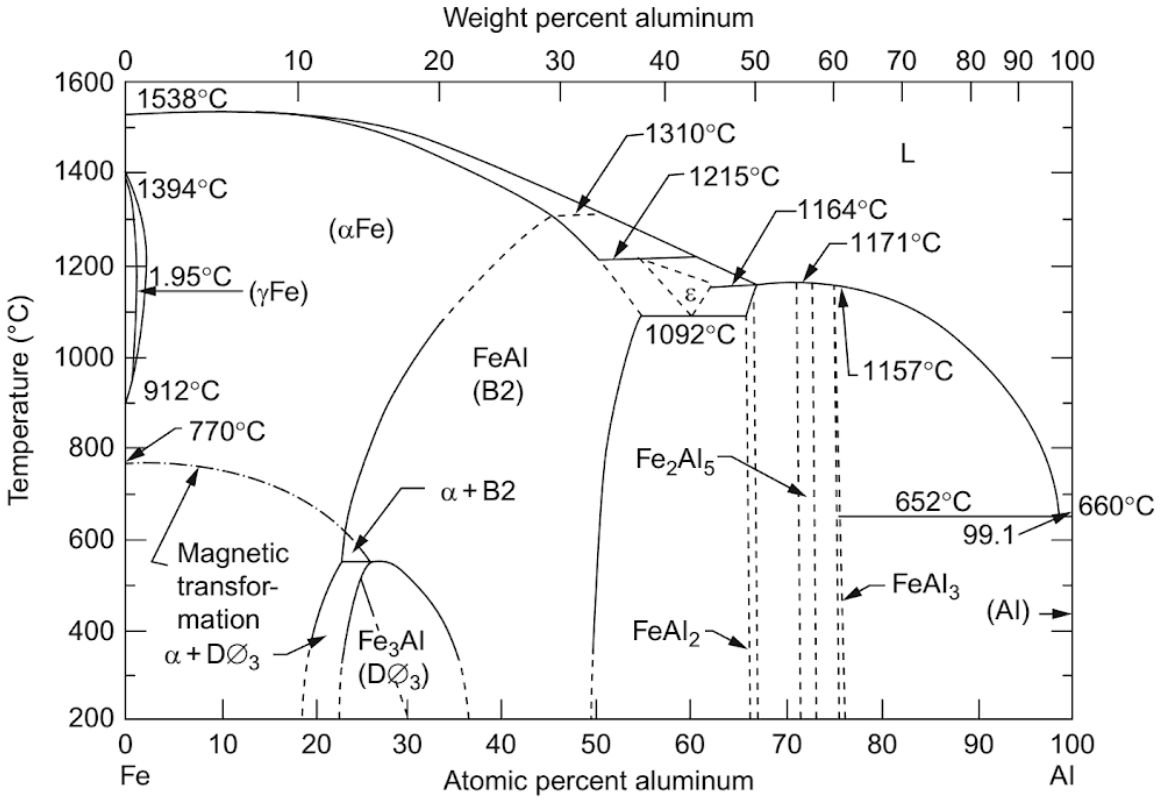

Figure 2.2.: Phase diagram of Fe – Al system with undetermined solubility lines plotted with dashed lines [29]

Table 2.1.: Composition (weight & atomic % aluminium), crystal structure and heat of formation of the intermetallic compounds in Fe-Al phase diagram under 550 °C [30, 31]

IMC	Crystal Structure	Composition wt.% Al	Composition at.% Al	ΔH_{298} kJ mol^{-1}
FeAl(β2)	BCC (order)	12.8 to ~37	23.3 - 54.9	-51.24
Fe_3Al(β1)	$D0_3$	~13 to ~20	23.6 - 34.1	-57.37
$FeAl_2$(ζ)	Triclinic	48 to 49.4	65.6 - 66.9	-81.9
Fe_2Al_5(η)	Orthorhombic	53 to 57	70.0 - 73.3	-194.04
$FeAl_3$(θ)	Monoclinic	58.5 to 61.3	74.5 - 76.6	-112.56

A proposed cause of iron aluminides' brittleness and environment embrittlement is their reaction with atmospheric water vapour at the metal surface, see equation (2.1). Generation

of atomic hydrogen drives into the metal and causes crack propagation [32]. Iron aluminides (40% at. Al) fail by intergranular fracture with little tensile ductility [33].

$$2\,Al + 3\,H_2\,O \longrightarrow Al_2O_3 + 6\,H^+ + 6\,e^- \tag{2.1}$$

FeAl is the most brittle of Fe-Al IMCs with 0% ductility. However, Fe_3Al has 4% ductility. They all display low strength above 550 °C. FeAl has the lowest creep strength due to excess equilibrium vacancies [34].

The formation of intermetallic phases between steel and aluminium alloys are dependent on the chemical potentials, nucleation conditions, mobilities of the constituent elements and duration and temperature of annealing, meaning not all intermetallic compounds from the phase diagram are formed in solid-state bonding [35].

Through using first-principles calculation Liu et al. [36] found that Fe_3Al has the largest bulk modulus, FeAl the largest Young's modulus and shear modulus. They also found that FeAl was the hardest. The appearance of microcracks in a material is always connected with the anisotropy; therefore it is essential to have an outline of the most anisotropic compounds in the Fe-Al-system because they are detrimental to the bond strength in CRB composites. Lui et al. [36] found mechanical anisotropy of Fe-Al compounds to be, in descending order $Fe_3Al > FeAl > Fe_2Al_5 > FeAl_2 > FeAl_3$ [36].

In studies done by Springer et al. [37] and Silvayeh et al.[38], they found that the dominant intermetallic compounds at the interface of solid iron/steel and liquid pure Al/Al-alloys are Fe_2Al_5 as the major phase and $FeAl_3$ (also called Fe_4Al_{13}) as the minor phase. The accelerated formation of Fe_2Al_5 is due to accelerated diffusion along its [001] direction [39]. It should be mentioned that a variety of solid-state joining methods, other than CRB, have been used in the studies referred here.

Springer et al. [35], Silvayeh [38], Dybkov [40], Bouayad et al. [41] and Bouché [42] have reported the growth rate of the most common intermetallic compounds to be the following:

- Fe_2Al_5 to have a parabolic growth after a non-parabolic transient period
- $FeAl_3$ to have a linear growth after a non-linear period
- The growth rate of Fe_2Al_5 is higher than $FeAl_3$ due to its tongue-like morphology which is thicker than serrated $FeAl_3$-sublayer.

Growth kinetics

The thickness of IML follows power-law relationship. This relationship is empirical and can decide the exponent,n, in equation (2.2). The value of n governs the rate controlling process in the growth of IML. If the IML growth is controlled by interface reaction then ($n = 1$), the volume diffusion of the constituent elements ($n = 0.5$), grain boundary diffusion ($n < 0.5$),

and mixed mechanism of growth ($0.5 < n < 1$) [43].

$$y = k\left(\frac{t}{t_0}\right)^n \tag{2.2}$$

$$\ln y = n \ln\left(\frac{t}{t_0}\right) + \ln k \tag{2.3}$$

where y is the IML thickness, t is time in seconds, t_0 is 1 second to ensure that the fraction in (2.3) is dimensionless. The value of n can be found by plotting $\ln y$ against $\ln t/t_0$ and determine n by least square method. Similarly, the temperature dependent growth rate constant can be determined by plotting y vs.$\sqrt{t}$ [44].

2.2.2. Alloying additions in Al-alloys and formation of IMCs

There has been little research on alloying additions to aluminium and their effect on the intermetallic layer in CRB. Hot dipping of Fe in molten Al-alloys and friction stir welding is the closest we can come to find similar characteristics or effect of these alloying additions to Al. The operating temperatures in the experiments referred below are near or over the melting temperature of aluminium but are still applicable in CRB experiments to some degree because they give a slight hint of compounds to expect at the intermetallic layer.

Recently, the addition of Si to Al has been found to attenuate the growth and change the composition of the intermetallic layer. Kurakin in 1970 [45] investigated intermetallic compounds formed in roll bonding of Al-1.2 wt.% Si-alloy with Fe in temperatures ranging from 250-600°C [35]. He detected compounds like Fe_2Al_8Si, Fe_4Al_{13} and porous Fe_2Al_5-phase. He found that addition of Si impedes the growth of intermetallic layer.

Similarly, Takata et al.[46] and Kailiang et al.[47] came to the same conclusion as Kurakin, when they investigated the role of Si in hot dipping of pure Fe into Al-8.2Mg-4.8Si (wt.%) and Zn-11Al-3Mg (wt.%) alloys, respectively. However, Kailiang [47] discovered that at 0.2 wt.%Si the thickness of the intermetallic layer was at a minimum. The mechanism by which Si content in Al-alloys impede the intermetallic layer is related to Si atoms penetrating the vacancy inFe_2Al_5 phase, causing lattice distortion [48]. The newly formed ternary compound, Fe_2Al_8Si, then acts as a diffusion barrier for Al [39].

On another instance Liu et al. [49] detected intermetallic phase of Fe_4Al_{13}, and Cr_2Al_{13} based γ phase in composite materials (CRB) of 430 stainless steel and 1100 aluminium. Recently, Arbo et al. [19] detected α-FeAlSi at the intermetallic layer of cold roll bonded composites of AA6082 and IF steel through transmission electron microscopy (TEM), Figure 2.3 shows their findings.

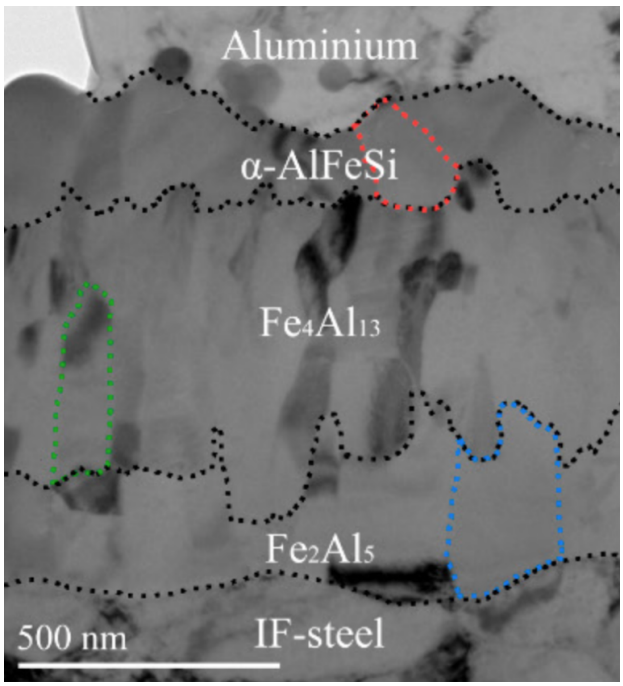

Figure 2.3.: Bright field TEM image of the interface between AA6083/IF steel, showing distinct intermetallic compounds [19]. Electron diffraction patterns are omitted.

2.2.3. Alloying additions in steel grades and formation of IMCs

Up to date, not much research has been done on the effect of alloying elements in steel grades and their influence on intermetallic growth. By utilizing thermodynamical models combined with electronic theory in pseudopotential approximation, Akdenic and Mekhrabov [50], calculation predicted which kind of substitutional impurities could affect on the Fe-Al diffusion layer. They calculated pairwise interatomic interaction potentials together with partial ordering energies to predict the activity of Al atoms in $\alpha - Fe_{0.98}(Al_{1-n}X_n)_{0.05}$ where X is an alloying element.

Their calculation predicted two groups of substitutional impurities, which could affect the activity coefficient of Al atoms in iron. Group I, reduced the the thickness of Fe-Al intermetallic diffusion layer and Group II increased.

Group I X_I = Si, Ti, Ge, Sb, Mg, Cu, Ca, Ag, Cd and Cr

Group II X_{II} = Co, Zn, Mn, Ni, Pb and Bi

Dangi et al.[51], devised an experiment setup to study kinetic aspects, such as diffusivities, of substitutional impurities in iron against pure iron. In his experiments of hot dipping of Fe-X alloys (X=Mn, Ni, and Si) in AA6061 aluminium alloy, they found that all the alloying elements in iron reduced the growth of the intermetallic layer. They found that the elements which reduced the intermetallic growth the most were Si > Ni > Mn.

The contradiction in the predictions of Akdenic and Mekhrabov and the findings of Dangi et al. is based on the diffusivities of alloying elements in the intermetallic layer or iron. Dangi et al. conclude that interdiffusion flux of alloying elements inside Fe_2Al_5 layer affects the growth of the intermetallic layer. For example in the case of Si: since the growth of Fe_2Al_5 layer in iron takes place along its [001] c-axis, Si solute occupies the excess vacancies in the the Fe_2Al_5 layer. This occupancy of vacancy by Si atoms reduces the vacancy concentration along the c-axis and thereby impedes the growth of Fe_2Al_5 layer [51].

2.3. Aluminium Alloys

In the quest for superior materials, alloys are added to improve the qualities of individual metals. Four general strengthening mechanisms can strengthen aluminium alloys: solid solution, work hardening, grain boundary, and precipitate strengthening. Solid solution strengthening is a process where solute atoms impart elastic strain in the solvent lattice and become obstacles to dislocation motion, thus increasing material strength. In the case of Al, solute atoms usually are substitutional. Fleischer [52] and Kocks [53] studied the degree of distortion caused by the solute on the fcc-Al lattice and the role of temperature in strengthening Al-alloys. Therefore elements with the largest difference in radii with Al would give best strengthening effect, e.g. $r_{Mn} - r_{Al} = -11.3\%$ and $r_{Mg} - r_{Al} = 11.7\%$. However, the strengthening potentials of these elements rely on their solubility in Al, see Figure 2.4.

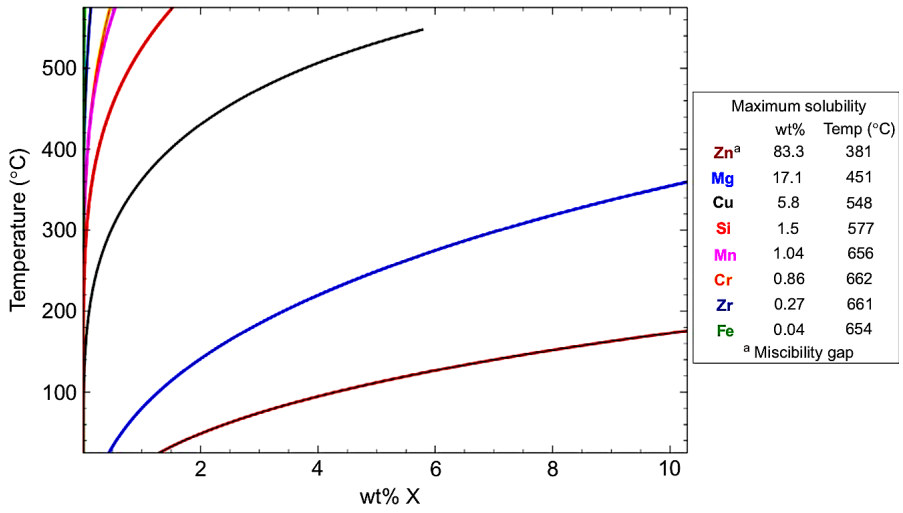

Figure 2.4.: Solubility lines of various solutes in Al, calculated by Thermo-Calc Software [54]

Precipitation hardening is another process by which Al-alloys are hardened. In this process, hardening is achieved by precipitation of dispersed precipitates of solutes in a supersaturated matrix by heating the alloy above the solvus temperature. Thereafter quenching and aging is

followed. The degree of hardening is through the size and interaction of dispersed precipitates with the dislocations. The interaction of dislocations with precipitates can be described by Orowan looping, bypass slip, or particle shearing. For more information about these interactions the reader is referred to [55].

Aluminium alloys are classified into two main categories: wrought- and cast composition. Their primary mechanism of property development additionally differentiates Al-alloys. These categories are heat-treatable (i.e. solution heat treatment, quenching, precipitation hardening) and non-heat-treatable (i.e. work hardening) Al-alloys [56]. Since cast aluminium alloys are out of the scope of this work, we will be concentrating on the Al wrought alloys. Table 2.2 shows standard designations of wrought aluminium alloys and their series.

Table 2.2.: Wrought Al alloy standard designation [57]

Series	Designation	Strengthening method
1xxx	Commercially pure aluminium ($>$99 wt.%)	Cold work
2xxx	Al-Cu and Al-Cu-Mg alloys	Heat treat
3xxx	Al-Mn alloys	Cold work
4xxx	Al-Si alloys	Cold work
5xxx	Al-Mg alloys	Cold work
6xxx	Al-Mg-Si alloys	Heat treat
7xxx	Al-Zn-Mg and Al-Zn-Mg-Cu alloys	Heat treat
8xxx	Al-Li-Cu-Mg alloys	Heat treat
9xxx	Unused series	-

[x] **first digit**:principle alloying element, **second digit**: variations of initial alloy, **third** and **fourth digits**: individual alloy variations.

The degree to which an Al-alloy has been given thermal or mechanical treatments to change its properties is called *temper designation.* The Aluminum Association has the following temper designations [58]:

F As fabricated

O Annealed

H Strain hardened with or without heat treatment

W Solution heat treated

T Solution heat treated for products with prior strengthening by heat treatment.

There are several degrees to strain hardening and heat treatments. A number after the letter characterizes their degree. For more comprehensive details on temper designation see [56].

The aluminium alloys used in this work are mainly from the series 5xxx and 6xxx. Sections below will give a brief description of their properties, usage and the role of alloying elements

in them.

2.3.1. 5xxx Al-Mg-Mn alloys

The 5xxx series resides in the category of non-heat-treatable alloys. They have a non-equilibrium degenerate eutectic reaction which disappears upon T6 treatment [59]. Alloys from this series show excellent strength and toughness capability and are used in marine application, storage tanks and pressure vessels. The main alloying element is magnesium and with its atomic radii being 11.7% bigger than the Al, provides excellent solid solution strengthening effect.

Magnesium gives this series its formidable corrosion resistance however simultaneously decreasing its formability. Magnesium giving its strength remains in solid solution and partially precipitated as Al_8Mg_2 cite here. The content of Mg in 5xxx alloys are kept between 2-5 wt.%. These alloys (>3 wt.% Mg wt. and $>50\,^{\circ}C$) are susceptible to grain boundary corrosion due to the formation of β phase, Al_3Mg_2, segregating towards grain boundaries (sensitization process), and acting as a galvanic couple between the grain boundary and interior –causing intergranular corrosion (IGC). The β phase precipitation reaction begins in the range of 50-200 °C; the reaction is given in the equation below [60, 61].

$$\text{Solid solution}\,\alpha \rightarrow \text{GP zones} \rightarrow \beta'' \rightarrow \beta' \rightarrow \beta \tag{2.4}$$

Micro-alloying elements, such as Zn, Cu, are added to improve ICG resistance. Micro-alloying elements, such as Zn, Cu, are added to improve IGC resistance. It does so by forming (less detrimental) τ-Mg(Al, Zn, Cu) phase. Mn is added to form supersaturated solid solutions under non-equilibrium solidification and is found as Al_6(Mn, Fe). Other dispersoids found in 5xxx series are of the form AlMg(Mn, Cr), Al(Mn, Cr), and Al(Mn, Fe)Si. Small additions of Si has detrimental effects since it pulls Mg out of solution by forming a stable phase Mg_2Si [54, 56, 59].

2.3.2. 6xxx Al-Mg-Si alloys

The 6xxx series is precipitation hardenable with silicon and magnesium as main alloying elements. In precipitation hardenable alloys, the strength and hardness of them can be enhanced by the formation of uniformly dispersed second-phase particles within the initial phase matrix [62]. The 6xxx alloy series is a popular choice for automotive parts for their workability and they provide a good compromise between the mechanical characteristics and corrosion resistance [63].

The main elements which provide strengthening to the 6xxx series are Mg, Si and small quantities of Cu. The additions of these elements with a combination of heat treatments utilize all four strengthening mechanisms in metals. The central equilibrium precipitated phase is β-Mg_2Si [54, 64]. The Al-Mg-Si system has the precipitation sequence which can be represented generally as:

$$\text{SSSS} \rightarrow \text{Mg, Si clusters} \rightarrow \text{GP zones (spherical)} \rightarrow \beta''\text{(needle)} \rightarrow \beta'\text{(rod)} \rightarrow \beta \qquad (2.5)$$

where SSSS is supersaturated solid solution, Mg, Si clusters are $Mg_2Si_3Al_{17}$,GP-zones[1] structure depends qualitatively on the Mg/Si ratio of the alloy [64], β'' is Mg_5Si_6, β' is Mg_9Si_5 and β is Mg_2Si [66]. For more information about the structure of these precipitates the reader is referred to van Huis' work [66].

The maximum strength of the material is achieved when the dispersed phase is of β''. A balanced Mg:Si ratio in the alloy composition increases the volume fraction and stability of β'' precipitates. Other than β'', subsequent particles in equation 2.5 are associated with over-ageing of the material, resulting in a reduction in hardness. The needle shaped β'' precipitates along $[100]_{Al}$ matrix. Artificial ageing, i.e. heat treatments promote β'' formation from the supersaturated solid solution of Mg and Si. Age hardening is achieved through three mechanisms [62]:

- Coherency strain hardening: interaction of dislocations with strain fields around GP zones and precipitates.
- Chemical hardening: the increase applied stress for a dislocation to cut through a precipitate.
- Dispersion hardening: formation of incoherent particles and an increase in shear stress required for dislocations to by-pass them.

[1] "A Guinier-Preston zone. A small precipitation domain in a supersaturated metallic solid solution. A GP zone has no well defined crystalline structure of its own and contains an abnormally high concentration of solute atoms. The formation of GP zones constitutes the first stage of precipitation and usually is accompanied by a change in properties of the solid solution in which they occur" [65].

Chapter 3.

Methods and procedures

This section provides a description of experimental procedure, materials used, and instruments used for characterization. The experimental procedure is the same as used in the work by Sverdrup [67].

3.1. Materials

For this thesis, two types of steel and aluminium alloys were selected. This section outlines the type of materials used, their chemical composition and dimensions.

3.1.1. Steel grades

316L

Iron-based metals containing more than 10% chromium are called stainless steels (St). An oxide layer of CrO is created on the surface by contact with the atmosphere, which functions as a barrier against oxygen and water. Chromium gives the metal corrosion resistance. The stainless steel grade used in this project is 316L. From now on, 316L will be referred to as 316. This material has high creep resistance, excellent formability and has corrosion and pitting resistance. The chemical composition and mechanical properties of 316L is described in Tables 3.1 and 3.2. The sheets of $120 \times 30 \times 1$ mm were cut by Struers Lobotom-5 stationary disc cutter to dimensions of $120 \times 15 \times 1$ mm.

SSAB DOMEX 355 MC E

The 355 is a high-strength low-alloy steel. It was received as in 5 mm thick sheets and were rolled down to 1 mm. The sheets were work-hardened due to rolling, therefore they were recovered and recrystallized at 750 °C for 4 hours in argon-atmosphere and quenched in room-tempered water to revert the mechanical properties to initial state. The sheets of

steel were cut to dimensions similar to 316L. The chemical composition and mechanical properties of 355 is described in Tables 3.1 and 3.2

Table 3.1.: Chemical composition of steel grades given as weight percent. C_{eq} is carbon equivalent.

	Fe	C	Al	Si	Ni	Mn	Nb	Cr	Mo	C_{eq}
355	Bal.	0.069	0.046	0.01	0.03	0.62	0.023	-	-	0.18
316	Bal.	0.022	-	0.336	10.060	1.298	-	16.645	2.025	-

Table 3.2.: Mechanical properties of steel grades as in pre-rolled state. Values obtained for 355 are after initial thickness reduction and heat treatment.

	Yield strength [MPa]	Ultimate tensile strength [MPa]	Vickers hardness [HV]
355	174	450	98
316	315	611	160±3.6

3.1.2. Aluminium alloys

AA6082

AA6082 is a precipitation hardenable alloy from the Al-Mg-Si family. For the work, the aluminium sheets were rolled down from 1.5 mm to 1.0 mm. The alloy was tempered to O-T4 (soft, solution treated and naturally aged to substantially stable condition). After rolling the alloy had a hardness of $68.22 \pm 0.93 HV$. Chemical composition in Table 3.3

AA5083

The AA5083 is considered to have the highest strength of the non-heat treatable alloys. Work-hardening increases their strength. The main alloying elements in AA5083 is Mg. As it was rolled to 1 mm, its hardness was measured to be $134.5 \pm 2.5 HV$. After heat treatment in a salt bath at 340 °C for 15 minutes, its hardness was measured to be $82,8 \pm 0.2 HV$ and it was cut to dimensions $120 \times 15 \times 1$ mm. The chemical composition of this alloy is given in table 3.3.

Table 3.3.: Chemical composition of aluminium alloys in weight percent [68]

	Al	Si	Fe	Cu	Mn	Mg	Zn	Ti	Cr
AA6082	Bal.	0.70 - 1.30	0.50	0.1	0.40 - 1.00	0.6 - 1.20	0.20	0.10	0.25
AA5083	Bal.	0.40	0.40 max	0.10 max	0.4 - 1.00	4.00 - 4.90	0.10	0.05 - 0.25	0.05 - 0.25

3.2. Experimental procedure

The experimental procedure was comprised of four steps:

1. Material arrangement
2. Pre-rolling
    a) Degreasing with acetone
    b) Brushing with steel wire
    c) Pre-heating
3. Rolling
    a) Roll bonding
    b) Quenching
4. Heat treatments
5. Analysis
    a) Scanning electron microscopy (SEM)
    b) Electron-dispersive X-ray spectroscopy (EDS)

3.2.1. Material arrangement

The arrangement of the St and Al composites were such that aluminium alloys served as the core between two steel sheets. This arrangement made four different types of composites of combinations: $St_x - Al_y - St_x$, where x is either 316 or 355 and y the designated aluminium alloy – AA5083 or AA6082.

3.2.2. Pre-rolling

The pre-rolling procedure involved degreasing the surface of each material with acetone and was brushing with 0.3 mm steel wire brush mounted on a hand-held grinder. The brushing was conducted once over each side of the aluminium sheet, and only at one side of steel samples - the side facing aluminium sheets. The hand-held grinder was swayed over the surface with force enough to make visible scratch marks on it, in transverse to the rolling direction. After brushing, the surfaces of the samples were blown over with compressed air to remove any remaining debris from the brushing. Figure 3.1 depicts the stacking order. The sheets were secured with rivets with aluminium sheets extending a little at the front end to make a precursor for the rollers. Rivets were used to hold the sample together so that sheets are not disbanded during rolling. All the procedure was conducted while wearing latex gloves.

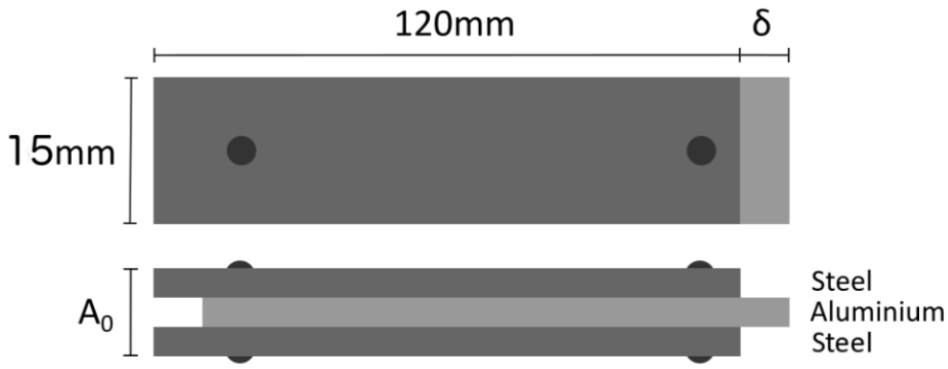

Figure 3.1.: Top and side view of the stacking order. The offset δ is a precursor for the rollers for better grip [67]. The thickness A_0 is ≈ 3 mm (*precise values of thickness are used in calculations*)

.

3.2.3. Rolling

All the samples were heated at 185 °C for 10 minutes to increase the temperature of the core to 150 °C and ease the flow of stresses during rolling – by making them softer. The time necessary for the samples to reach an internal temperature of 150 °C was based on work done by Solhaug [17]. The samples were quenched in water immediately after them were fed into symmetric diameter rollers of 205 mm Ø and with a speed of 6.6 m min^{-1}. A sketch of cold rolling process is shown in figure 3.2.

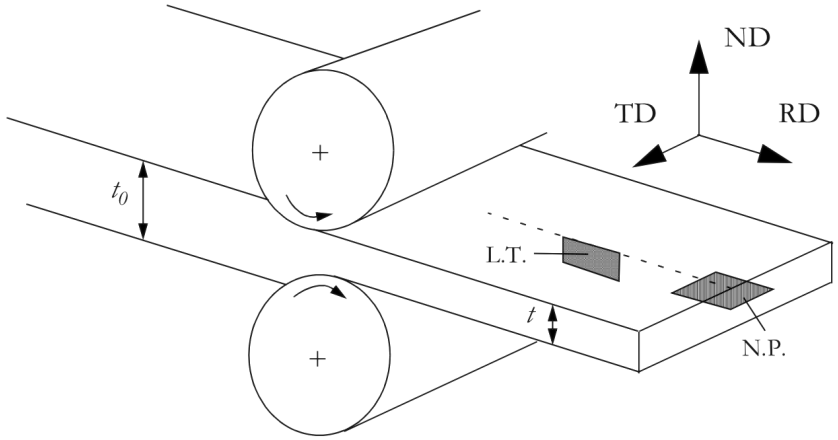

Figure 3.2.: Sketch of the cold rolling process. The initial and final thickness is indicated by t_0 and t, the longitudinal transverse section (L.T.) is the face for mechanical measurements and microscopy [69].

3.2.4. Heat treatments

After rolling, small pieces of the samples were cut on a stationary disc cutter to reveal the rolling direction surface, lengthwise, see figure 3.2. To get an idea of intermetallic layer formation arbitrary heat treatment temperatures and durations were chosen for each composite combination. After that, heat treatment temperatures and durations were finely tuned to find the starting temperature on which the intermetallic layer starts to form.

For the ease of convenience, the nomenclature of samples is chosen as described below with an example:

$$\overbrace{355}^{\text{Steel grade}} - \underbrace{5083}_{\text{Al alloy}} - \overbrace{400C}^{\text{Temperature°C}} - \underbrace{2\,\text{min}}_{\text{Duration}} \tag{3.1}$$

$$\text{All the samples from one combination, e.g. : } 355 - 5083 \tag{3.2}$$

The heat treatment durations and temperatures for all the samples is given in Figure 3.3.

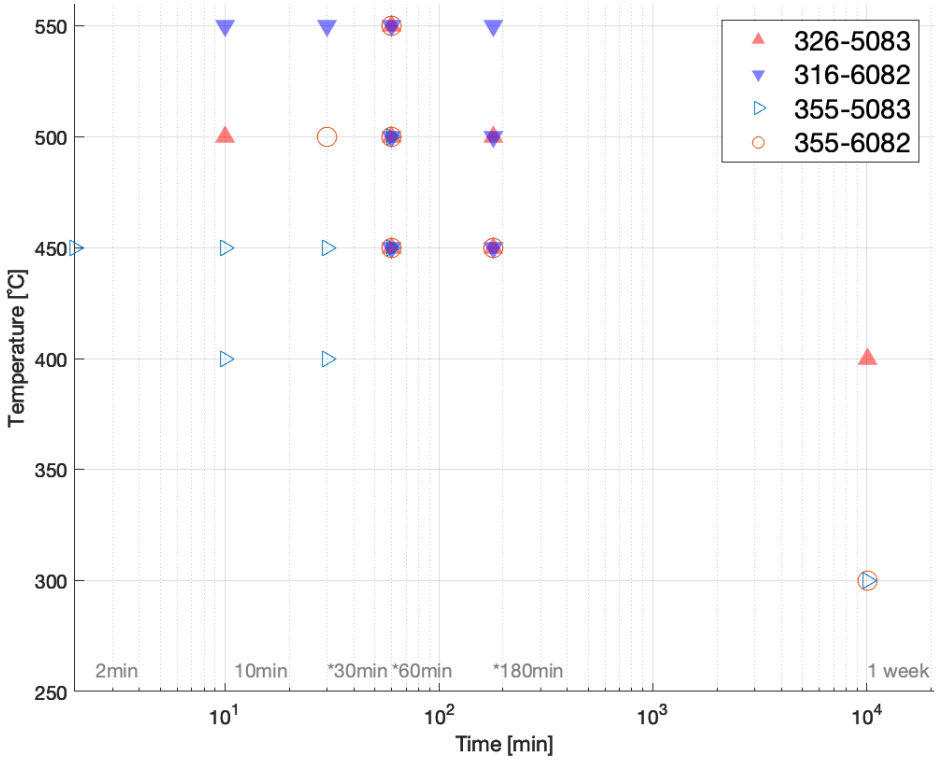

Figure 3.3.: Heat treatment map for all steel and Al combinations. Several time durations are marked with asterisk for clarity.

After heat treatments samples were quenched in room temperature water and the ≈ 1 cm cut samples were then embedded in the epoxy mould for further analysis.

The surfaces of the moulded samples were grinded with [500, 800, 1200, 2400] SiC grit paper and polished with 3 and 1 µm in diamond suspension on Struers Tegramin-30.

Surface preparation for SEM was conducted on Buehler Vibromet 2 with 0.05 µm colloidal silica. To make the samples conductive, the samples were wrapped in aluminium foil to avoid charging inside SEM chamber.

3.3. Characterization techniques

3.3.1. Energy dispersive X-ray spectroscopy (EDS)

Energy Dispersive X-ray Spectroscopy (EDS) is used for chemical microanalysis in combination with SEM. The basic principle behind the technique is that characteristic X-rays emission are stimulated from a specimen by a focused high-energy beam of electrons. When the high-energy electron hits an electron of the inner shell in the specimen, the electron is ejected, and a vacancy is created in the shell – leaving a net positive charge at the location of the vacancy. An electron of an outer shell fills the newly created electron vacancy. This transition of the electron from a high-energy shell to a lower-energy shell emits a high energy photon with sharply defined frequencies, X-ray, to compensate for the energy differences of the shells. Emitted X-rays are characteristic for each element because of energies of the differences between atomic energy levels of the targeted specimen. For an incoming beam to generate an X-ray photon, it needs to exceed the critical excitation energy by $E_0 > 2E_c$ [70].

For quantitative analysis, PB-ZAF algorithm is used to provide compositional data. PB-ZAF method is a standardless microanalysis method. In EDS, the intensity of the photons measured/detected from a sample (characteristic X-rays and continuum X-rays) is proportional to the concentration of that element. Other elements present in the matrix (emission volume) also influences the intensity. This influence is categorized in three ways, which also describe the abbreviation of ZAF [70]:

- electron scattering and retardation ("atomic number" matrix effect, Z)
- X-ray absorption within the specimen ("absorption" matrix effect, A)
- X-ray generation by absorption of X-rays ("secondary fluorescence", matrix effects, F)

The matrix effects are then rendered in an algorithm combined with a theoretical and empirical approach to be a valuable tool in quantitative microanalysis. These corrective algorithms aim is to increase accuracy and reduce the number of required standards as references [70, 71].

The scanning electron microscope used in this word are: FSEM - Zeiss Ultra-55 Limited Edition and LVFESEM-Zeiss Supra-55 VP and their EDS detectors were from BRUKER and EDAX, respectively.

3.3.2. Electron probe microanalyzer (EPMA)

EPMA is similar to EDS analysis but more precise. It gets its precision with several EDS and WDS detectors. WDS (wavelength dispersive X-ray spectroscopy uses Bragg's law and movable monocrystals as monochromators to analyse and differentiate incoming raw spectra [72]. The type EPMA used in this work was JEOL JXA-8500F equiped with five WDS and one EDS detector. The EPMA analysis was conducted by senior engineer Morten Peder Raanes at the Department of Materials Science and Engineering at NTNU.

3.3.3. Nanoindentation

Nanoindentation tests are conducted to estimate elastic modulus and hardness of a specimen. In traditional indentation tests, an indenter of known geometry is pressed on a surface with a known load. The load of the indenter is then divided by the area of the indentation it leaves behind on the surface to give hardness measurement. In nanoindentation, a similar technique is used. However, the load and displacement of the indenter are continuously recorded as pressure is applied on the surface of the specimen [73].

The nanoindentation tests were conducted by Prof. Jianying He at the Department of Structural Engineering at NTNU.

Chapter 4.

Results

This chapter is divided into four sections. Each part describes the results obtained for each composite combination. The sections are further divided by the temperature of the heat treatment. SEM micrographs of the intermetallic layer (and EDS/EPMA analysis for some samples) will be presented for each duration and temperature in the sub-sections.

4.1. Sample: 355-5083

The total reduction percentage of the sample 355-5083 was measured in optical microscope by taking 20 measurements at four different places. The total reduction was measured to be 61%.

The heat treatment program for the 355-5083 combination is plotted in Figure 4.1.

Some abbreviations are used to signify which part of the intermetallic layer (IML) is in the discussion. For example, IML-Al-side means the side of intermetallic adjacent to the aluminium layer and vice versa for the IML-St-side. All the EDS scans, i.e. Line scan, mapping and point scans are PB-ZAF corrected.

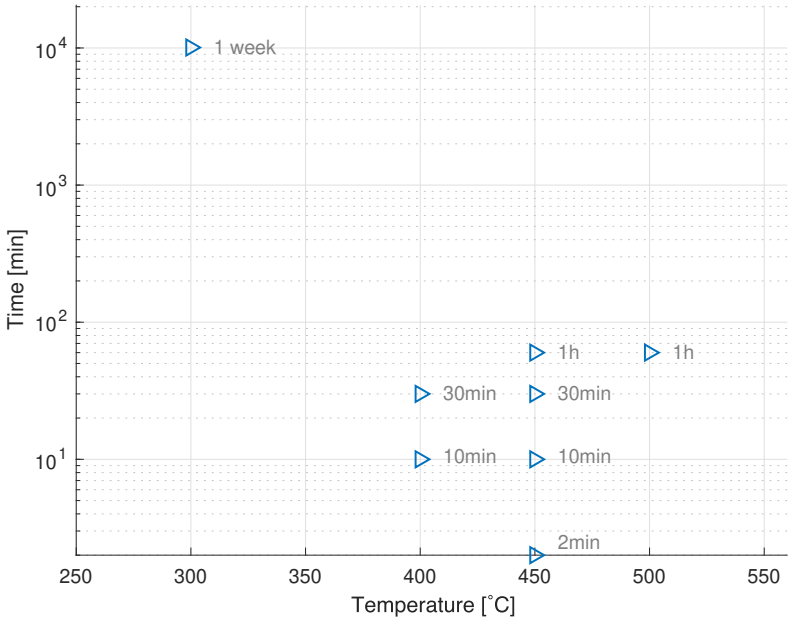

Figure 4.1.: Heat treatment plan for the combination 355-5083

The subsections below describe EDS analysis and images of the interface taken with SEM at different heat-treatments and durations.

4.1.1. 355-5083 at 300 °C for 1 week

Figure 4.2 shows micrographs of the interface taken with SEM and their respective EDS measurements. Delamination was observed mostly throughout the whole intermetallic layer, at the Al-side. The intermetallic layer was measured to be 2.76 µm.

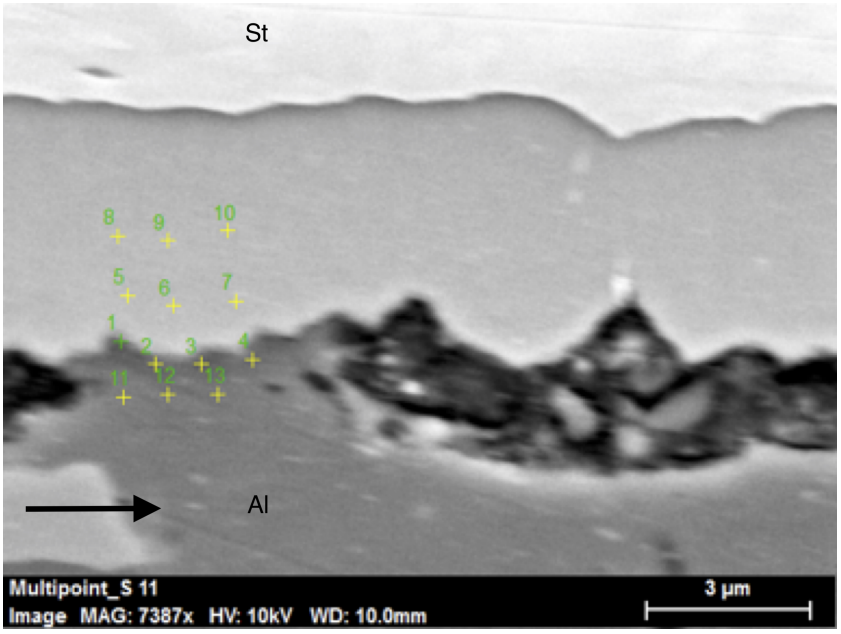

(a)

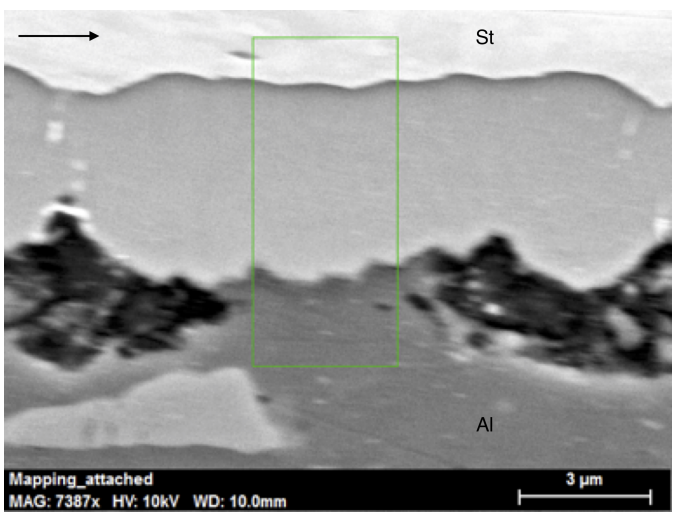

(b)

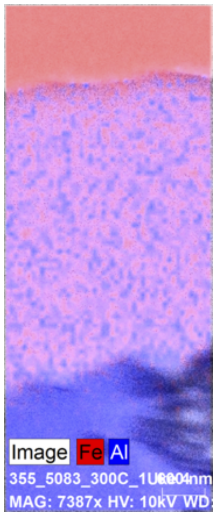

(c)

Figure 4.2.: Sample: 355-5083-300C-1week. **(a)** Point scans to find type aluminides type, see Table 4.1. **(b)** The area for EDS mapping indicated with the green rectangle and **(c)** corresponding EDS with Fe and Al indicated with colour legends at the left corner. Arrows in each figure indicates rolling direction. Avg. IML thickness: 2.76 µm

The Table 4.1 shows results obtained from EDS point scans in Figure 4.2**a**.

Table 4.1.: EDS scans of points marked in Figure 4.2**a** with mass percent and their ratios. Points 8-10 are near Fe-side, and 5-7 near the interface of IMC and Al. Points 1-4 are omitted due to large emission volume and 11-13 for their irrelevance.

Point #	Al[at.%]	Fe [at.%]	Ratio Al/Fe
8.	67.07	30.83	2.18
9.	66.77	31.01	2.15
10.	67.05	30.7	2.18
5.	67.77	30.21	2.24
6.	66.85	30.97	2.16
7.	67.5	30.32	2.23

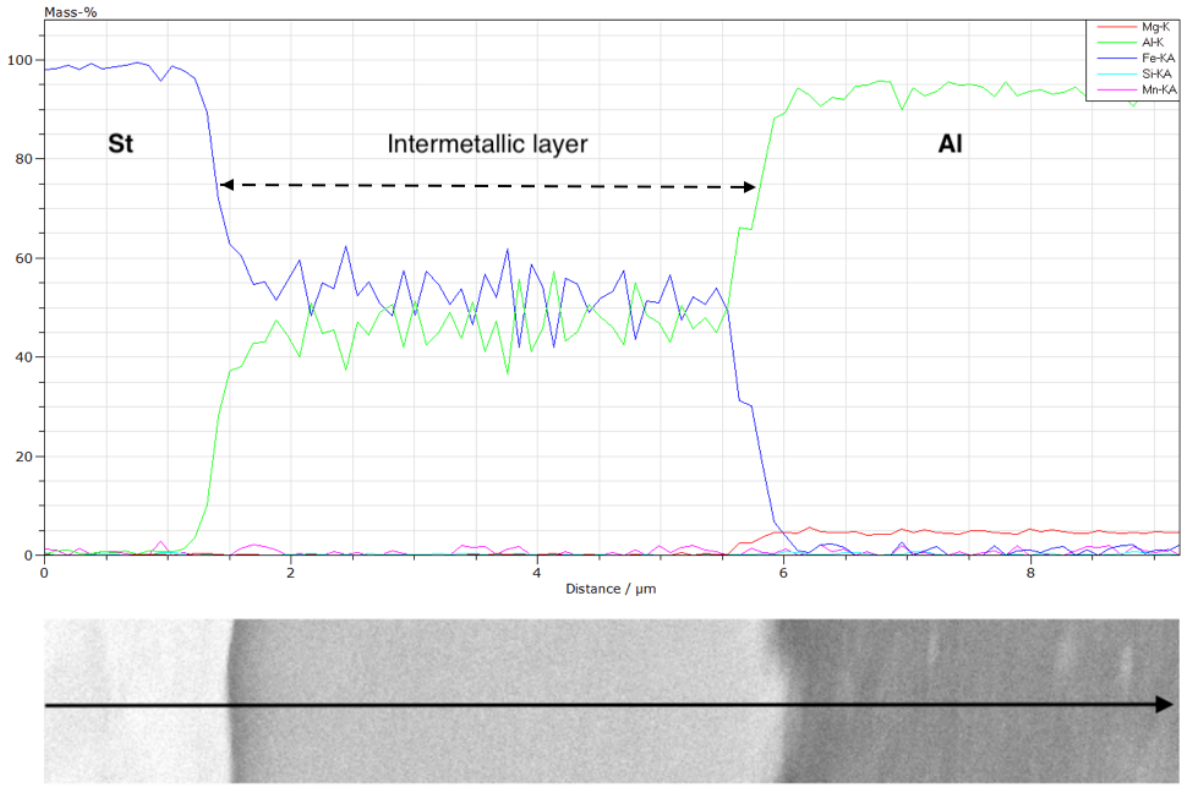

Figure 4.3.: EDS line scan at the interface of 355-5083 heat treated at 300 °C for one week. y-axis displays mass percentage.

4.1.2. 355-5083 at 400 °C for 10 min and 30 min

355-5083-400C-10min

After heat-treatment the micrographs of the sample was taken in SEM and two types of phases were observed at the interface near the aluminium side. These observations are shown

in Figure 4.4.

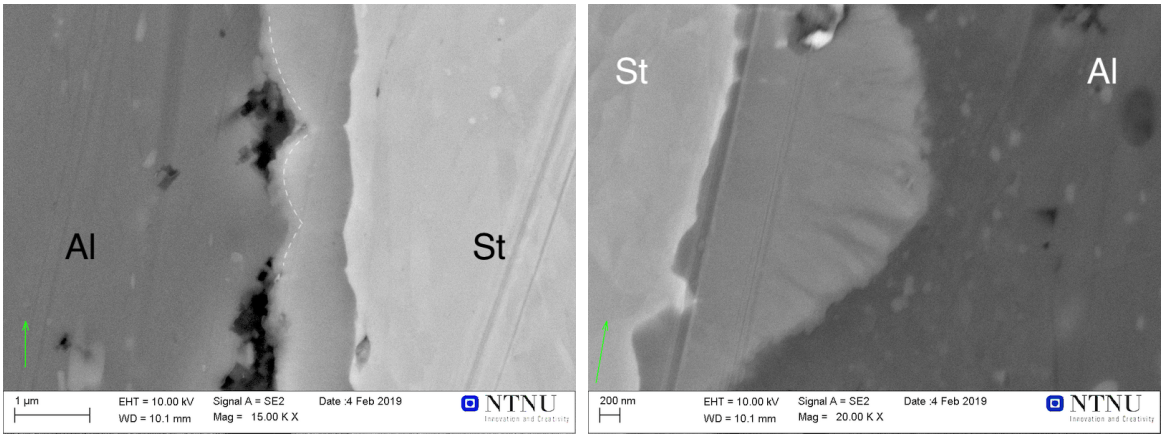

(a) **(b)**

Figure 4.4.: Micrographs of 355-5083-400C-10min. Magnifications:**(a)** 15kx and **(b)** 20kx. Stainless steel and aluminium layers are marked with St and Al, respectively. Dashed white lines exhibit the thin $FeAl_3/Fe_4Al_{13}$ phase at the IML. Arrows indicate rolling direction. Avg. IML thickness: 1.38 µm

In Figure 4.4 a second phase is observed at the Al-interface, marked by a white dashed lines. This phase is predicted to be $FeAl_3/Fe_4Al_{13}$. The intermetallic phase thickness is only at 1.38 µm after 10 minutes of heat treatment at 400°C.

355-5083-400C-30min

Micrographs of 30 min heat-treatment are in Figure 4.5. Here a second phase is observed at the interface near the aluminium side. Cracks and micro-voids are also observed at the aluminium side. The intermetallic layer thickness seems to have increased by 220% only by prolonging the heat treatment by 20 minutes at 400°C. The second phase going into the Al is also visible at the Al-interface in 4.5b, indicated by the red arrow.

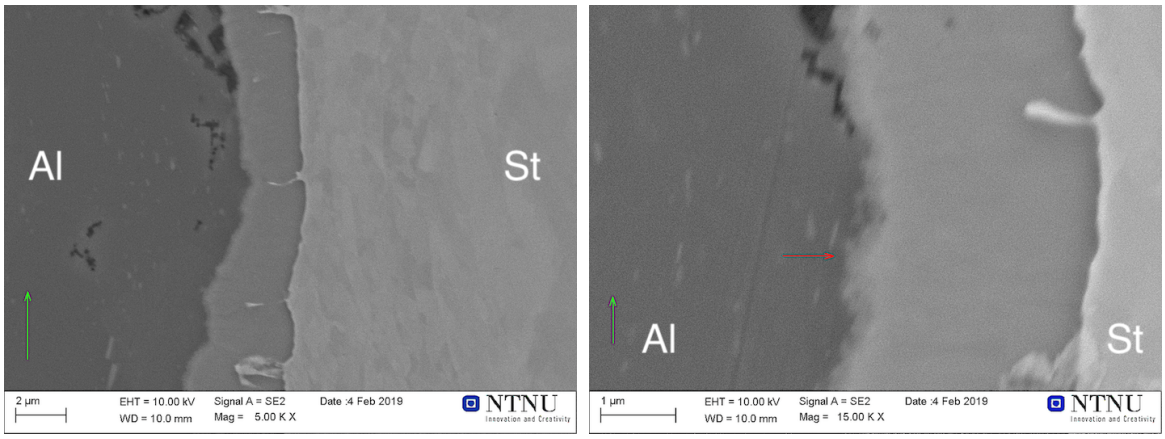

(a) **(b)**

Figure 4.5.: Micrographs of 355-5083-400C-30min. Magnifications:**(a)** 5kx **(b)** 15kx. Red arrow points at the second phase layer at aluminium side. The bright side is steel 355 and darker side Al5083. Arrows indicate rolling direction. Avg. IML thickness: 3.04 µm

4.1.3. 355-5083 at 450 °C for 2, 10, 30, 60 min

355-5083-450C-2min

Micrographs of 2-minute heat-treatment at 450 °C are shown in Figure 4.6. In these micrographs, it can be observed that aluminium alloy has suffered pit corrosion due to the use of Blue Lubricant (ethanediol-based) under sample preparations, therefore the dark, patchy colour.

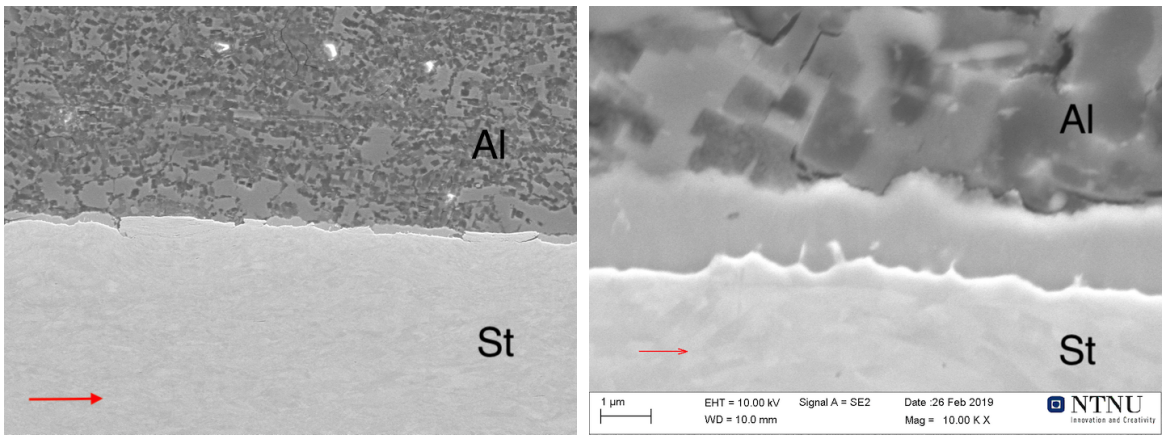

(a) **(b)**

Figure 4.6.: Micrographs of 355-5083-450C-2min. Magnification: **(a)** 1kx **(b)** 10kx. The bright side is steel 355 and darker side Al5083. Arrows indicate rolling direction. Avg. IML thickness thickness: 1.55 µm

The result from EDS mapping is shown in Figure 4.7. An area was chosen for the mapping and EDS was conducted on the area. An insignificant amount of Mg was found at the interface, therefore only Al and Fe are shown below.

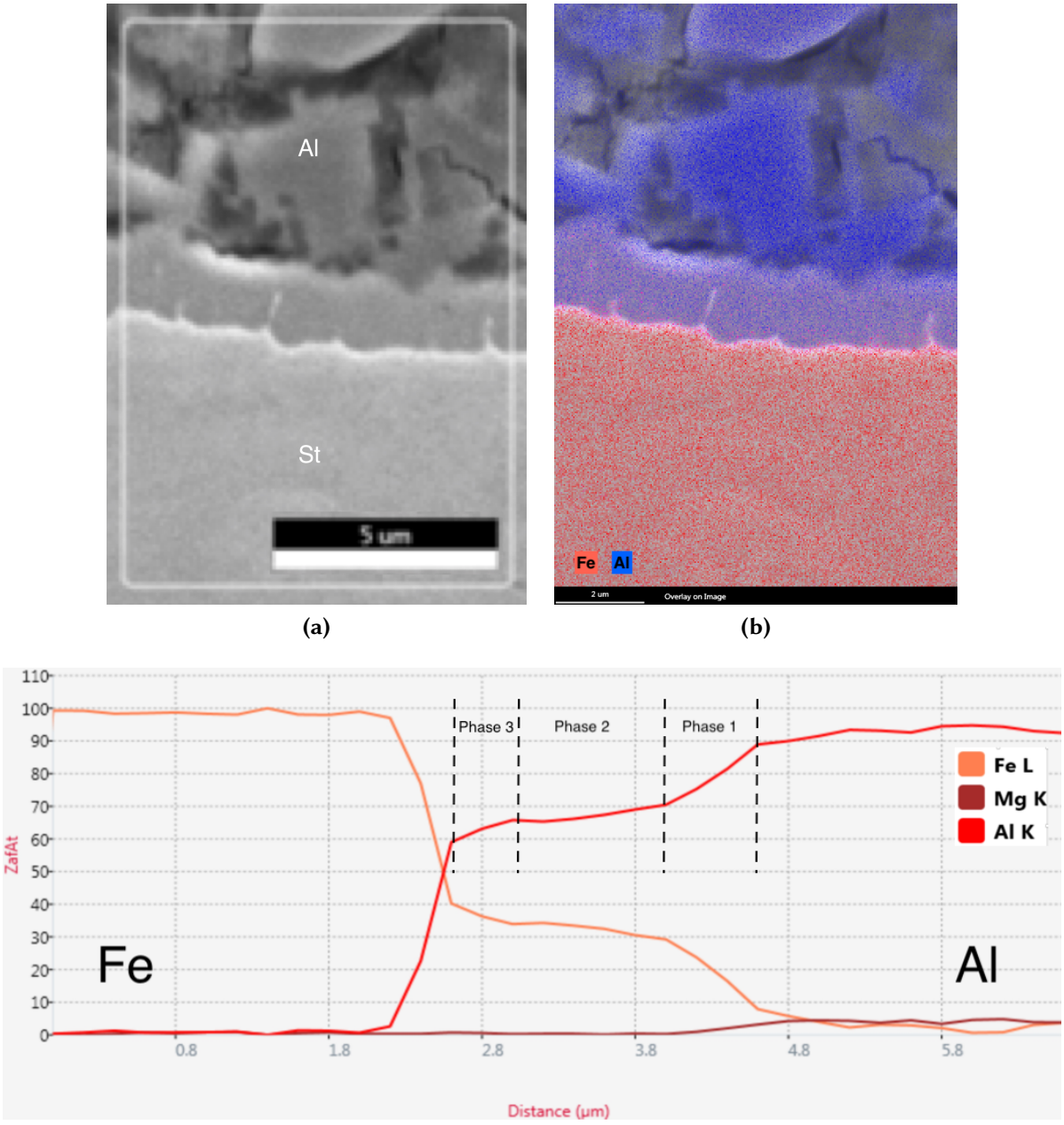

Figure 4.7.: (a, b) EDS mapping of the interface in the sample 355-5083-450C-2min **(c)** A line scan taken through the interface showing intermetallic made of Fe and Al with negligible amount of Mg.

Some points were marked at the interface for EDS Point scan to understand the composition of the IMC areas near the Al and Fe-side, Figure 4.8.

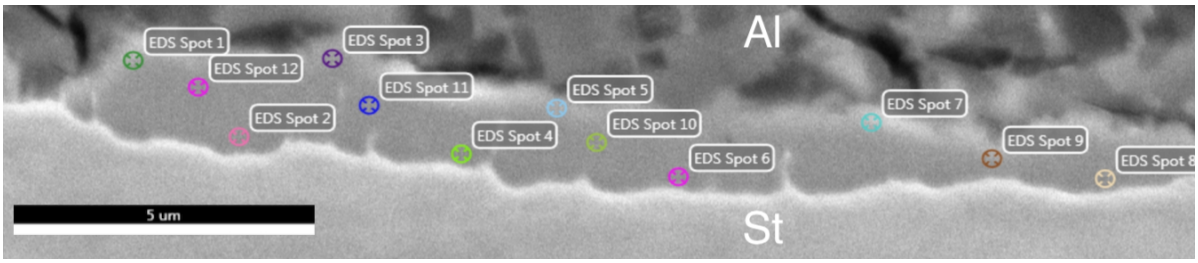

Figure 4.8.: Sample: 355-5083-450C-2min. Locations marked for EDS Point scan.

Corresponding EDS point scans results from Figure 4.8 are given in Table 4.2. Al at.% is observed to decrease as towards steel.

Table 4.2.: Results from point scans in Figure 4.8 with predicted phases. The odd points from 1-7 correspond to IML-Al-side, even numbers from 2-8 correspond to areas at IML-St-side side and points 9 to 12 are located in the middle of IML.

Points	Fe [at. %]	Al [at.%]	Ratio Al/Fe	Pred. phase
1.	16.59	77.07	4.64	$FeAl_3$
3.	17.58	82.42	4.46	$FeAl_3$
5.	17.26	82.74	4.79	$FeAl_3$
7.	17.45	78.00	4.47	$FeAl_3$
9.	21.83	77.51	3.55	Fe_2Al_5
10.	18.48	81.52	4.41	Fe_2Al_5
11.	18.76	81.24	4.33	Fe_2Al_5
12.	17.95	81.14	4.52	Fe_2Al_5
2.	25.34	73.13	2.93	Fe_2Al_5
4.	29.95	70.05	2.34	FeAl?
6.	32.35	67.65	2.09	FeAl?
8.	32.47	67.30	2.07	FeAl?

355-5083-450C-10min

Micrographs of 10 min heat-treatment at 450 °C are given below in Figure 4.10. Three phases are observed at the interface having columnar grain growth.

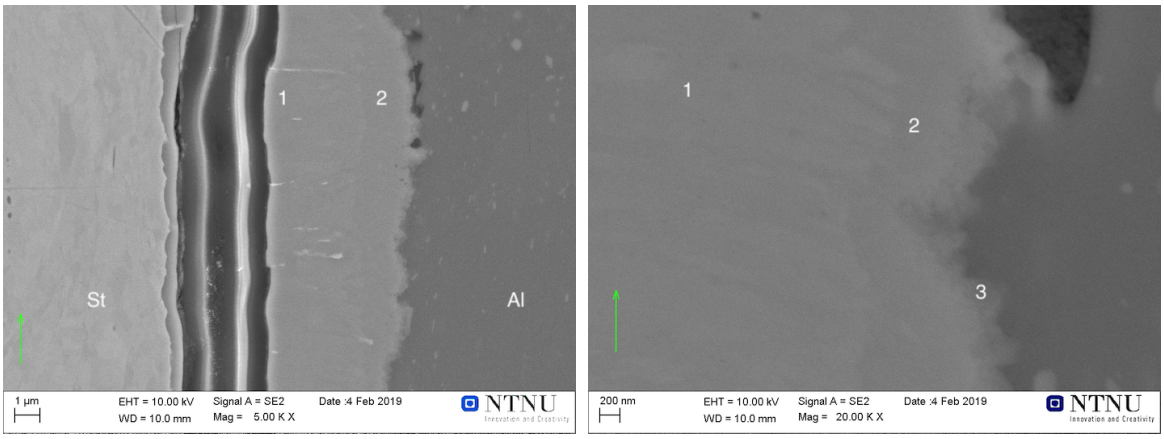

(a) **(b)**

Figure 4.9.: Micrographs of 355-5083-450C-10min. **(a)** the vertical layer at the interface is due to delamination **(b)** at 20kx magnification three phases are observed. Arrows indicate rolling direction. Avg. IML thickness: 5.35 µm

355-5083-450C-30min

The SEM micrographs of the interface between ST and Al are in Figure 4.10. The delamination of the interface is visible in left side of the image in 4.10a. Here also a two phases are visible at IML-Al-side.

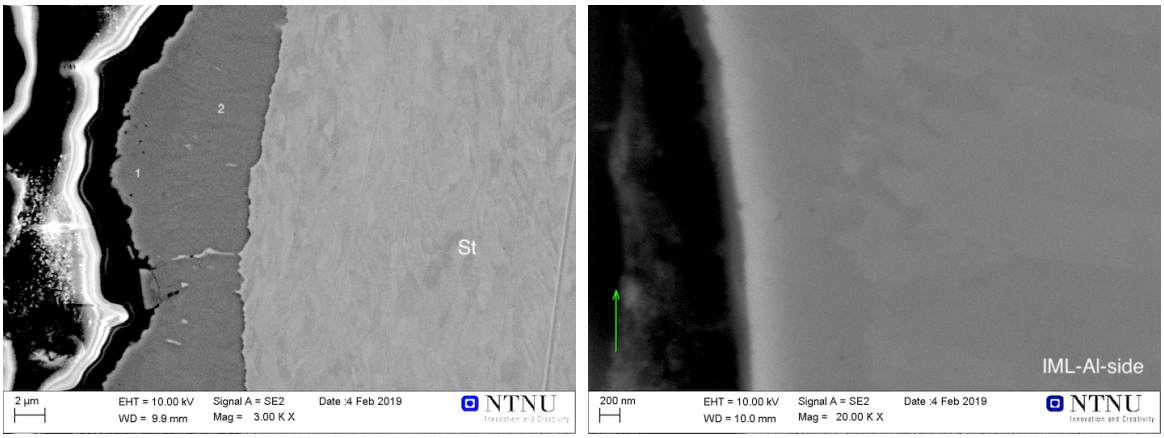

(a) **(b)**

Figure 4.10.: Micrographs of 355-5083-450C-30min. **(a)** the vertical layer at the interface is due to delamination and charging of the epoxy layer which is very bright **(b)** a close up of two phases at 20kx magnification. Arrow indicate rolling direction. Avg. IML thickness: 9.60 µm

Results from nanoindentation are displayed in Figure 4.11.

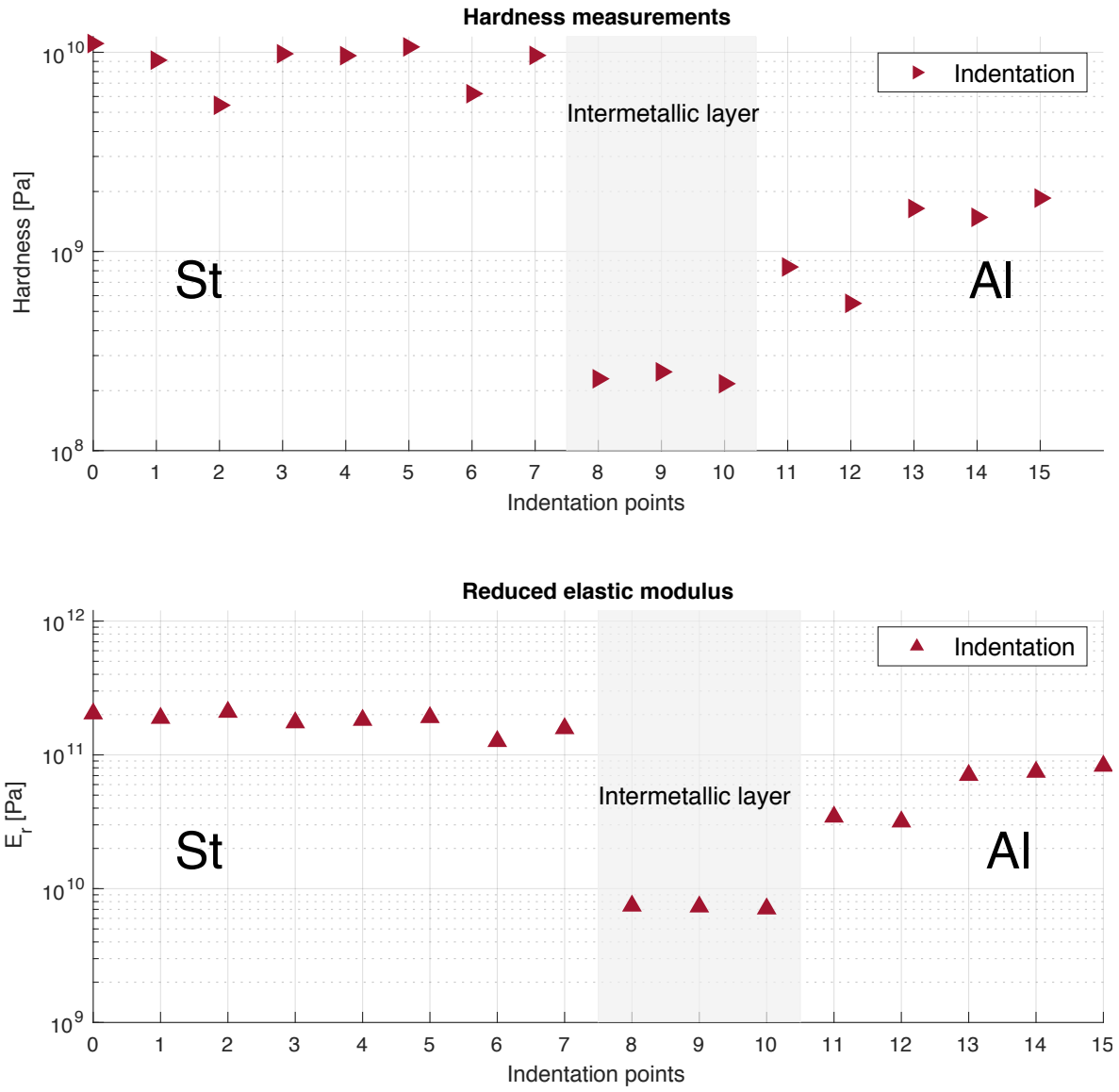

Figure 4.11.: Results from nanoindentation of 355-5083-450C-30min at the interface. The upper part shows hardness measurements and the lower for the reduced elastic modulus[1]. See Appendix 1 for the indentation locations.

355-5083-450C-60min

SEM Micrographs from 1 hour heat treatment are in Figure 4.12. Due to delamination, either during quenching or after rolling, when the samples were mounted in epoxy mould,

[1]Reduced elastic modulus is defined as: $1/E_r = (1 - v_i^2)/E_i + (1 - v_m^2)/E_m$, where E and v are the isotropic Young's modulus and Poisson's ratio, and the subscripts i and m refer to indenter and sample material, respectively [73].

the mould got into empty spaces. The distortion on the image is due to the charging effect of epoxy in SEM.

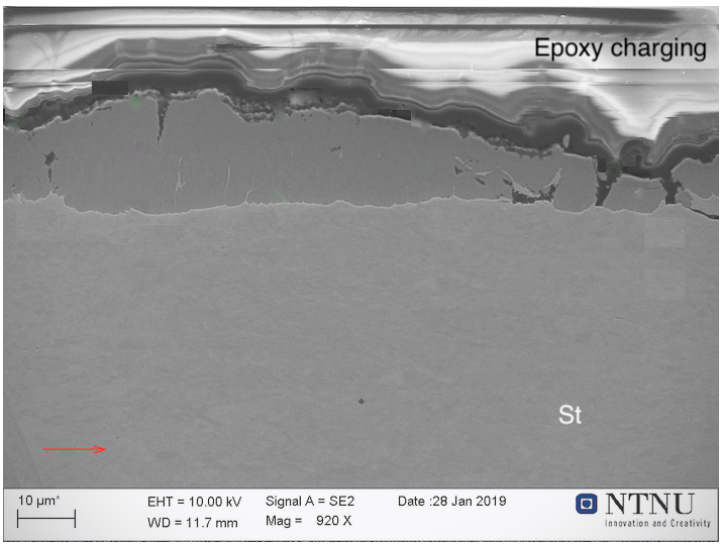

Figure 4.12.: Micrographs of 355-5083-450C-60min. The bright/very dark horizontal layer at the interface is due to delamination and accumulation of epoxy which is being charged, therefore the bright colour. Two phases can be observed. The sample had delaminated at the aluminium side; therefore only the IMC attached to the steel side is visible. Arrow indicate rolling direction. Avg. IML thickness: 13.16 µm

4.1.4. 355-5083-500C-60min

The intermetallic layer thickness 355-5083-500C-60min was measured to be 20.16 µm. At the IML-St-side the finger-like Fe_2Al_5 sub-layer was visible.

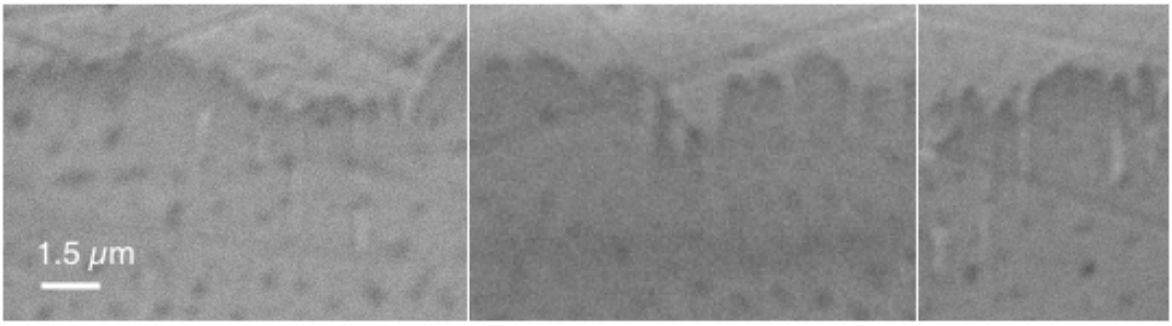

Figure 4.13.: Finger-like Fe_2Al_5 sub-layer at the IML-St-side of 355-5083-500C-60min. Magnification 1.6kx.

4.1.5. Summary

Figure 4.14 shows the overall duration of heat-treatments for each temperature interval and the measured IMC thickness. The values for IMC thicknesses are obtained from taking the average of 20 measurements taken from four locations at the interface. The IML thickness was measured predominantly in ImageJ software.

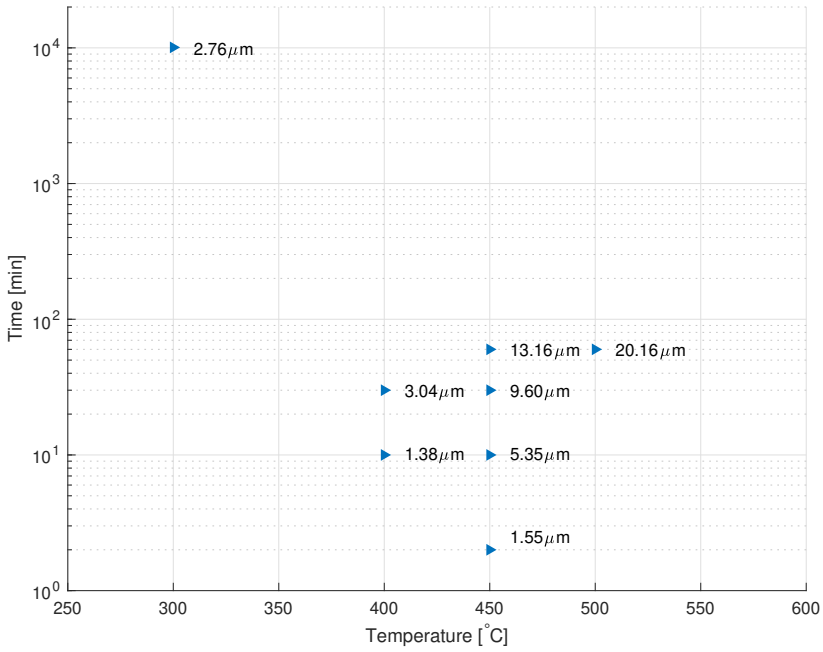

Figure 4.14.: Thickness of intermetallic compound measured in SEM vs. duration and temperature of the heat-treatment for samples made with 355-5083.

Significant observations from SEM images and EDS analysis are as following:

355-5083-300C-1week Uniform layer. More likely to have one phase

355-5083-400C-10min Two phases observed. With diffusion of some lighter elements into the IML

355-5083-400C-30min Three phases observed.

355-5083-450C Three phases observed. Through EDS analysis phases are most likely to be Al-[$FeAl_3$-Fe_2Al_5-FeAl?]-St

355-5083-500C Largest intermetallic layer. Finger like structures are observed at IML-St-side.

4.2. Sample: 355-6082

The total reduction percentage of the sample 355-6082 was measured in OM by taking 20 measurements at four different places. The total reduction was measured to be 57%. Then several pieces were cut for thermal treatments. Figure 4.15 shows the heat treatment plan for samples made with 355-6082.

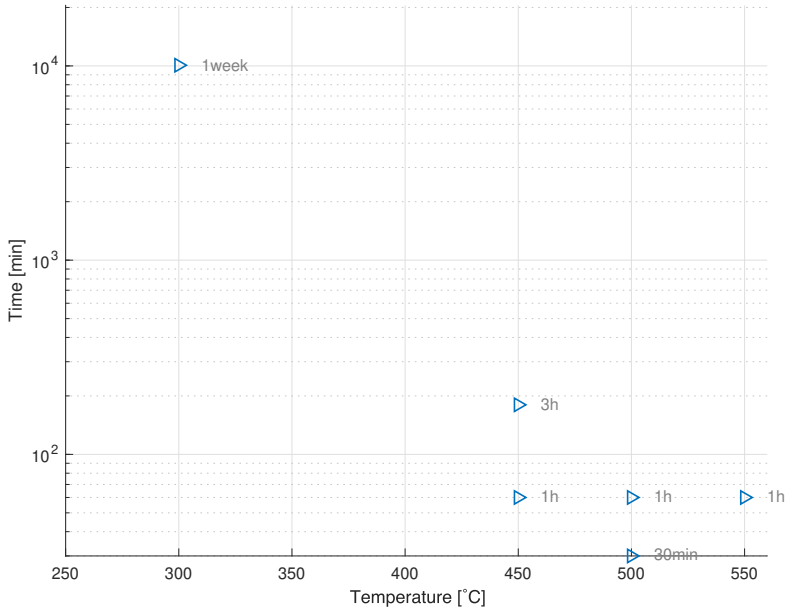

Figure 4.15.: Heat treatment plan for the combination 355-5083

4.2.1. 355-6082 300 °C for 1 week

Figure 4.16 shows micrographs of the interface of St and Al in the sample 355-6082-300C-1week. No intermetallic layer is observed at this temperature. A spike in Si concentration at the Al-interface is observed. Mg concentration gradient is observed to increase a little towards the IML.

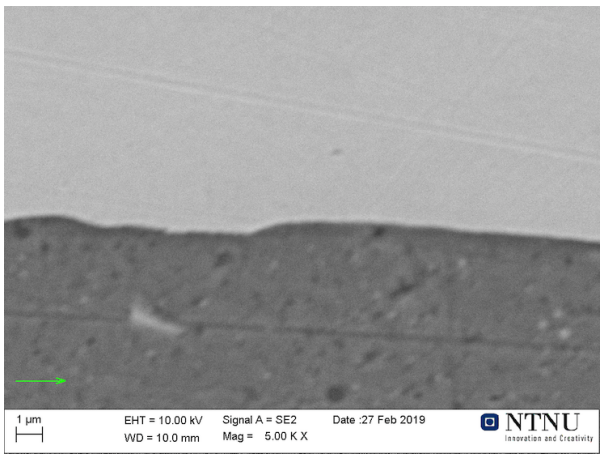

(a)

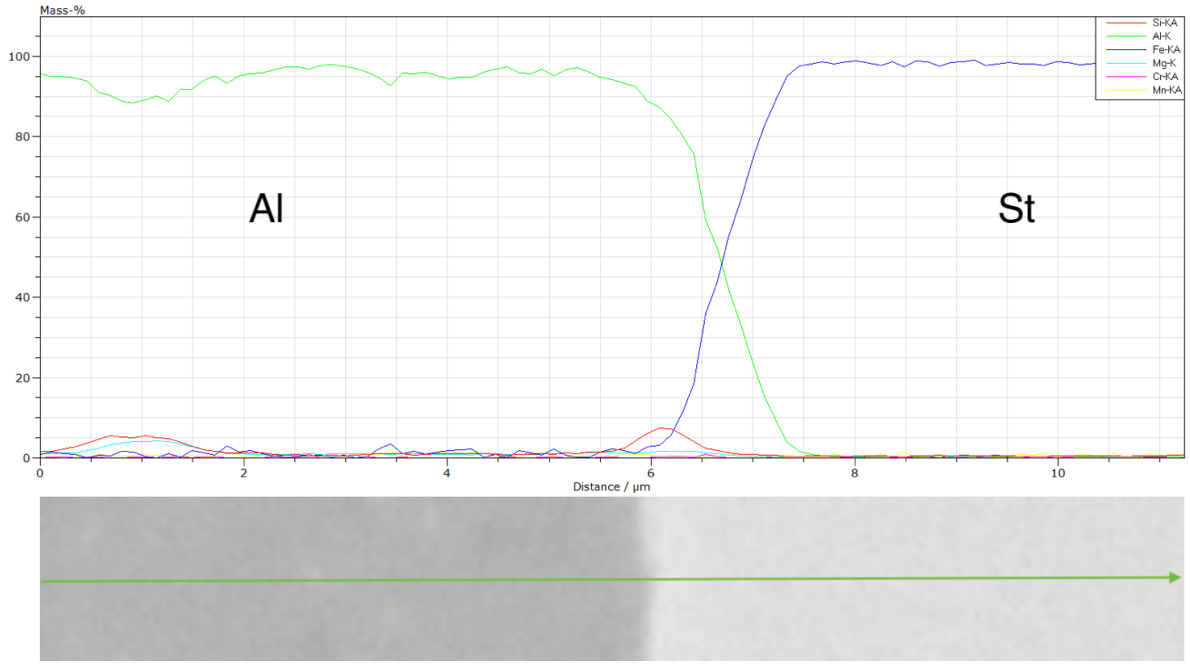

(b)

Figure 4.16.: Micrographs of 355-6082-300C-1week. **(a)**No intermetallic layer visible at 5kx magnification **(b)** line scan at the interface shows no significant intermetallic layer

4.2.2. 355-6082 at 450 °C for 60 and 180 min

355-6082-450C-60min

Close to no IML was observed with 450 °C for 60 min. With the highest magnification possible only 0.08 µm layer was observed. The IML was fragmented and had a non-continuous development across the St-Al interface. The micrographs are shown in Figure 4.17.

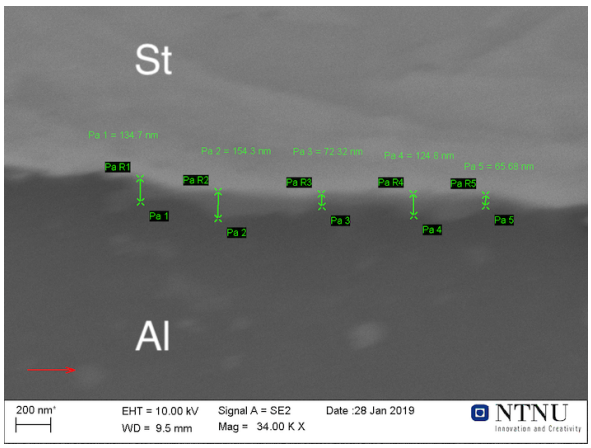

Figure 4.17.: Micrographs of 355-6083-450C-60min. The average of the IMC layer was measured to be 0.08 µm. The magnification is at 34kx.

355-6082-450C-180min

The micrographs of the sample 355-6082-450C-180min is shown in Figure 4.18. At this heat-treatment a very narrow layer of IMC was observed. The formation of IMC is in the Al-interface.

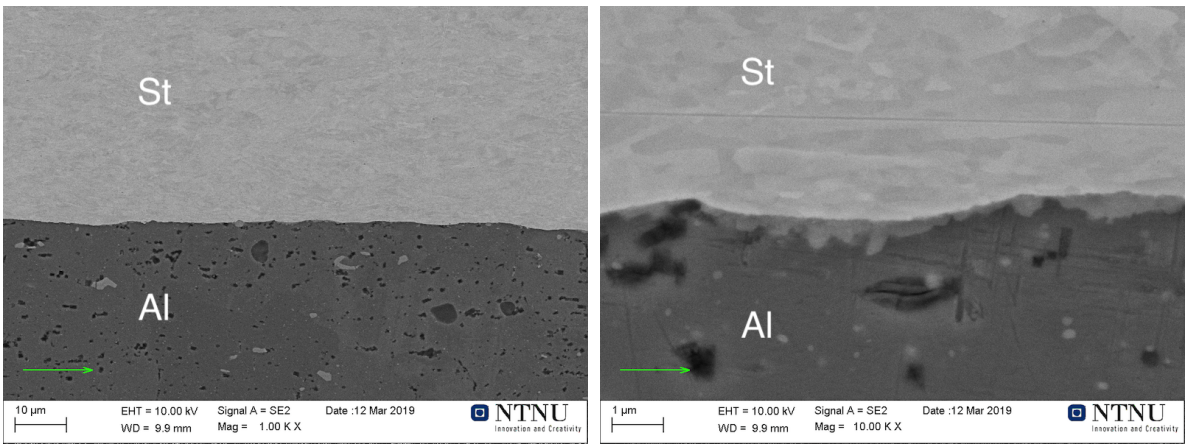

(a) **(b)**

Figure 4.18.: Micrographs of 355-6082-450C-180min. **(a)** No intermetallic layer visible at 1kx magnification **(b)** a close up of the intermetallic layer at 10kx magnification shows IMC layer. Arrows indicate rolling direction. Avg. IML thickness: 0.3 µm

4.2.3. 355-6082 at 500 °C for 30 and 60 min

355-6082-500C-30min

The micrographs of the sample 355-6082-500C-30min are shown in Figure 4.19. The phases are observed at the IML with finger like structures.

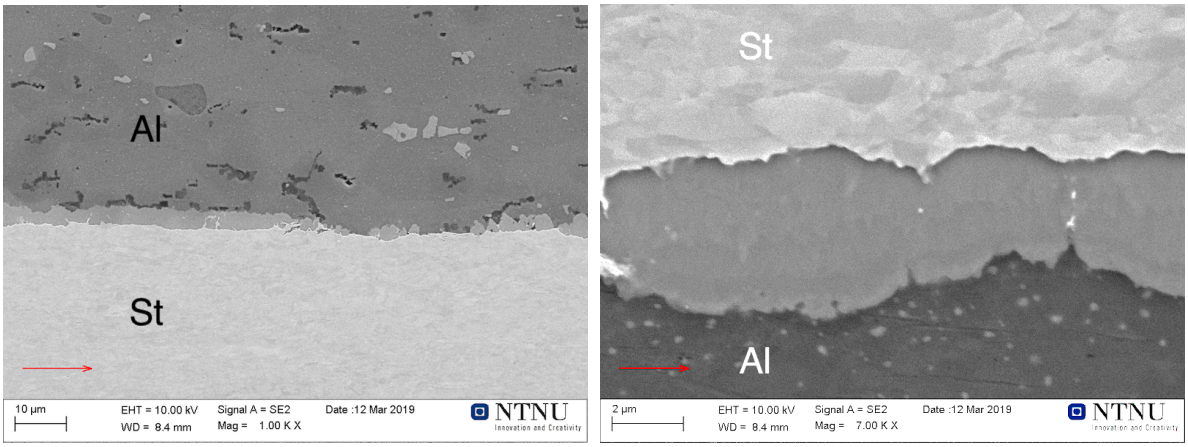

(a) **(b)**

Figure 4.19.: Micrographs of 355-6082-500C-30min. **(a)**No intermetallic layer visible at 1kx magnification **(b)** a close up of the intermetallic layer at 7kx magnification shows IMC layer with 3 phases. Arrows indicate rolling direction. Avg. IML thickness: 3.1 µm

355-6082-500C-60min

The micrographs of 355-6082-500C-60min is shown in Figure 4.20.

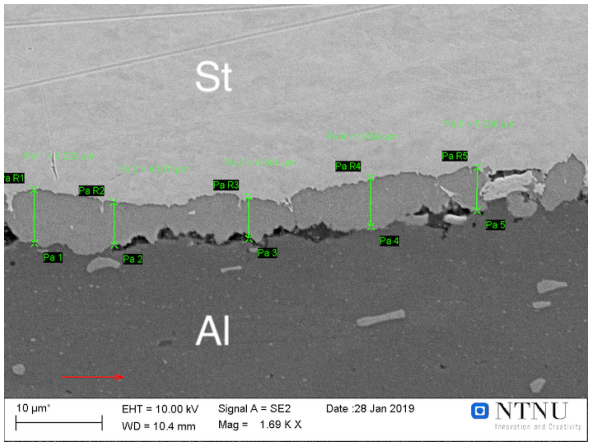

Figure 4.20.: Micrographs of 355-6082-500C-60min. The average of the IMC layer was measured to be 5.0 µm.

4.2.4. 355-6082 at T = 550 °C for 60min

The micrographs of the sample 355-6082-550C-60min are shown in Figure 4.21. From the SEM contrast, some heavier elements are observed in the IML. Columnar grain growth is visible in the IML.

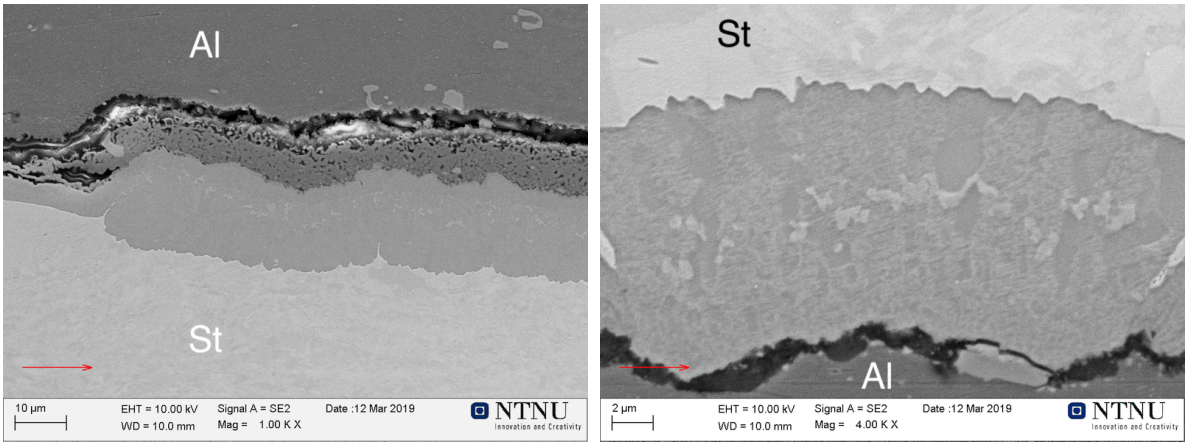

(a) **(b)**

Figure 4.21.: Micrographs of 355-6082-550C-60min. **(a)** The horizontal dark line is due to delamination occurred in the process of quenching/thermal stresses. The IML is finely detached from the Al **(b)** finger like structures are observed at the IML with in dissolved islands of Fe in between the mentioned structures. Arrows indicate rolling direction. Avg. IML thickness: 8.3 µm

4.2.5. Summary

Figure 4.22 shows the duration of heat-treatment for each temperature interval and the measured IML thickness. The values for IML thicknesses are obtained from taking the average of 20 measurements taken from four locations at the interface.

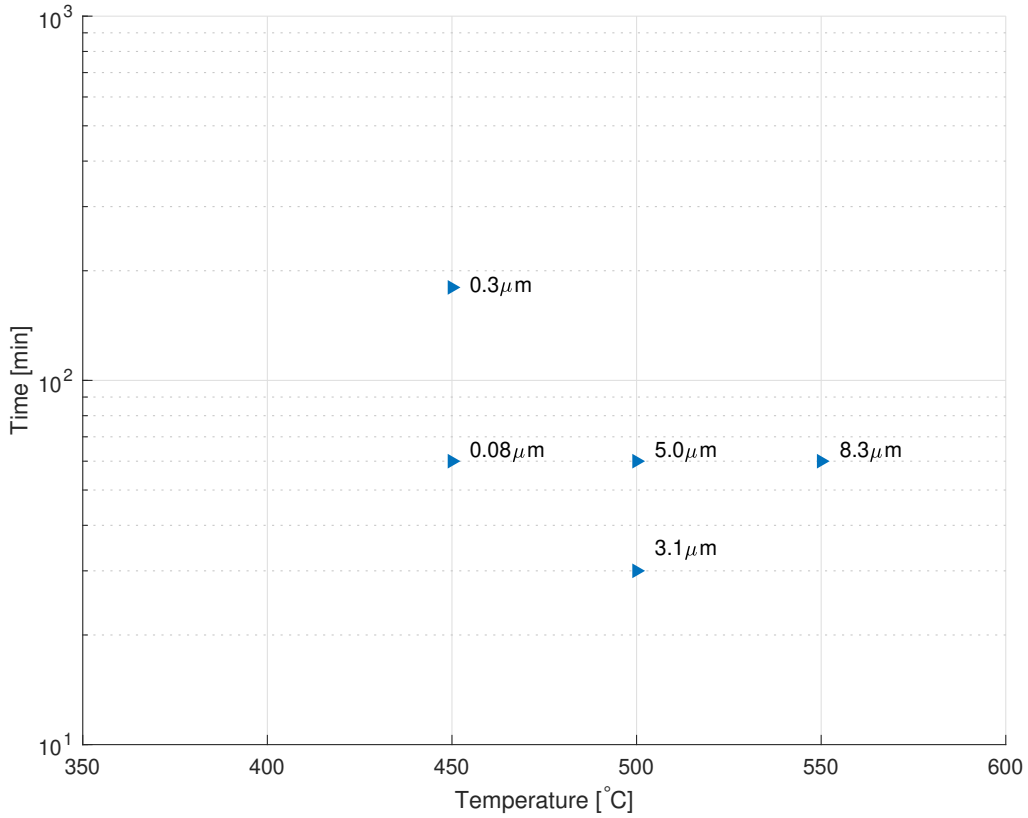

Figure 4.22.: Time-temperature precipitation diagram for 355-6082. The thickness of the IMC layer is shown on each heat-treatment points.

- Very thin IML in temperatures below 450.
- Significant formation of IML in temperature above 500C. Three phases are observed at this temperature.
- From the SEM contrast, some heavier elements are present at the IML.

4.3. Sample: 316-5083

The total reduction percentage of the sample 316-5083 was measured in optical microscopy by taking 20 measurements at four different places. The total reduction was measured to be 61%.

The temperature range and duration of heat treatments are given in the Figure 4.23.

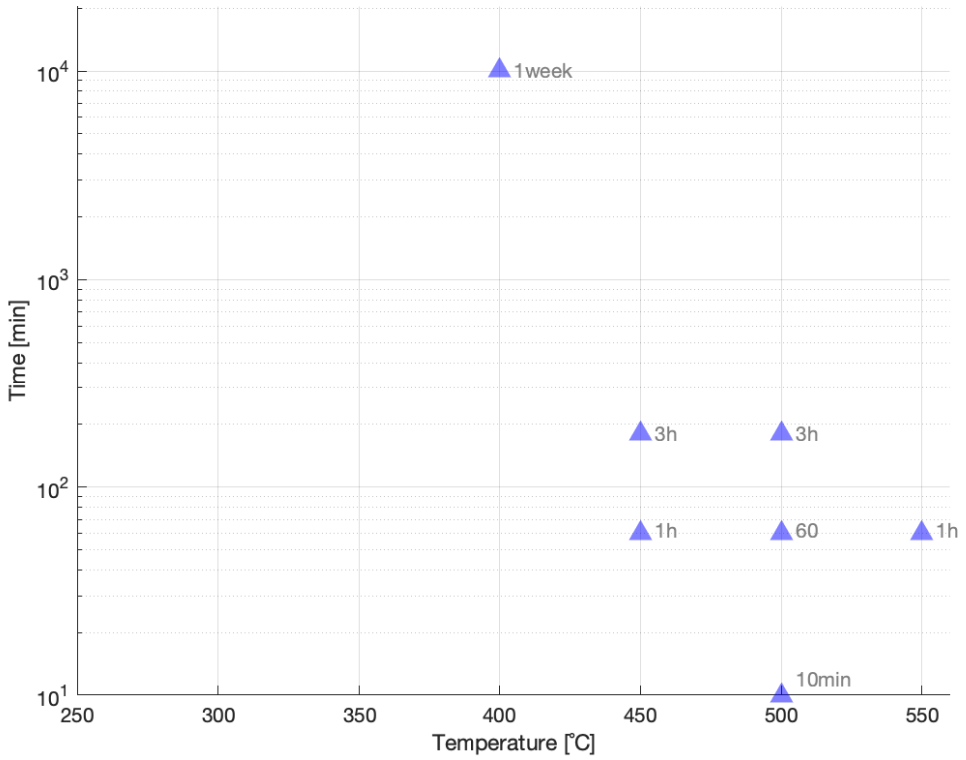

Figure 4.23.: Heat treatment plan for 316-5083 samples.

4.3.1. Sample: 316-5083 at 400 °C for 1 week

Figure 4.24 are the micrographs ofr 316-5083 heat treat in saltbath for 1 week. Pit corrosion on the Al-side is due to use of Blue Lubricant (ethanediol-based) under sample preparations, therefore the dark patchy color. The blue Lubricant was used to avoid scratches on the sample while mounting them in the sample holder for vibrational polishing in colloidal silica.

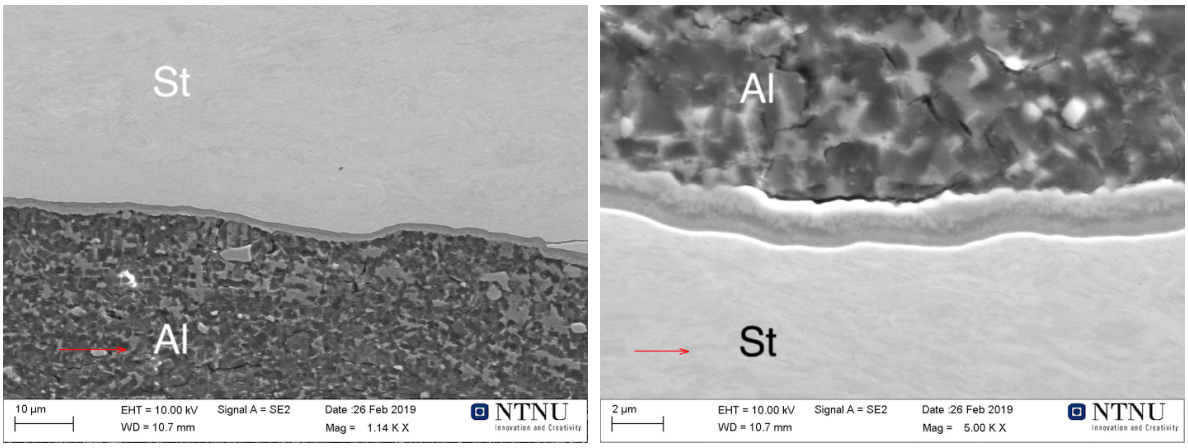

(a) **(b)**

Figure 4.24.: Micrographs of 316-5083-400C-1week at **(a)** 1kx and **(b)** 5kx magnification.. The average of the IML was measured to be 1.54 µm.

The EDS line scan of image in Figure 4.24b is shown in Figure 4.25.

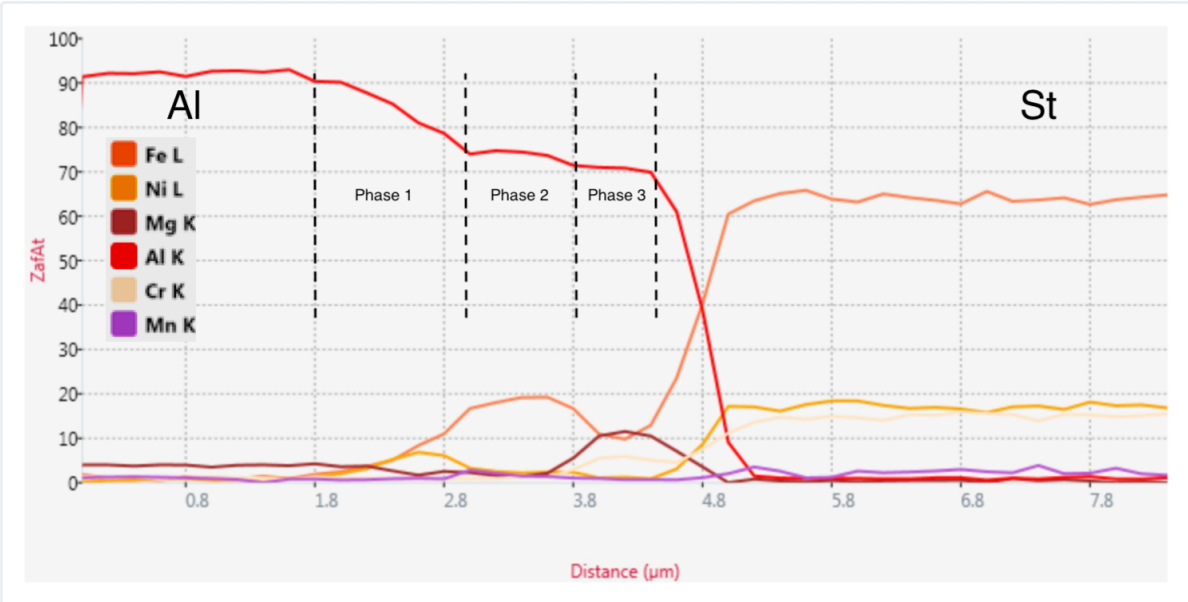

Figure 4.25.: EDS line scans at the interface of 316-5083-400C-1week. Y-axis shows ZAF-corrected atomic percent %.

From the line scan, one can observe the Al EDS line having three separate plateau. This indicated different phases present at the IML. Ni and Mg concentration spikes towards the St-interface is observed. Figure 4.26 displays points marked for point scan. The points are marked near the Al-interface, near the St-interface and in between them.

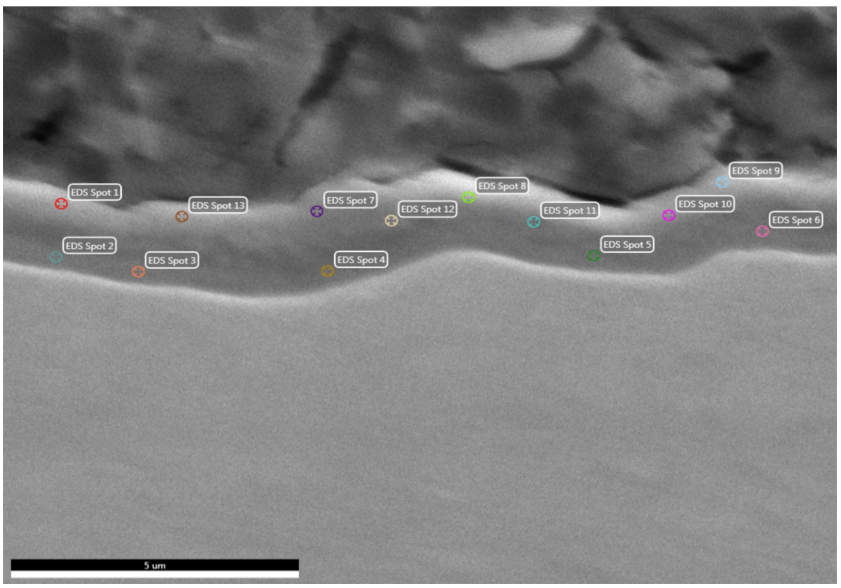

Figure 4.26.: EDS point scan of 316-5083-400C-1week interface. See Table 4.3 for results.

In Table 4.3 results of EDS point scans are shown. Points 1, 13, 7, 8 and 9 are at IML-Al-side and 2 to 6 are at IML-St-side and 10 to 12 are at the middle of intermetallic layer.

Table 4.3.: Point scan results of 316-5083-400C-1week, showing atomic percentages of the main alloying elements in 316 and 5083. Some places and elements have been left [-] due to large compositional errors, caused by pear-shaped emission volume of electrons.

Points	Fe [at. %]	Al [at. %]	Mg [at. %]	Ni [at. %]
1	8.11	85.42	-	-
13	7.21	84.3	-	6.22
7	7.2	87.24	2.86	-
8	9.23	81.62	3.71	3.28
9	5.19	86.4	-	5.07
10	8.89	80.78	2.51	4.8
11	6.56	80.08	7.48	-
12	8.75	84.36	3.79	-
2	10.38	78.77	4.64	-
3	11.42	78.76	3.82	-
4	6.88	76.27	10.56	-
5	8.39	79.05	6.66	-
6	9.49	78.96	5.91	-

4.3.2. Sample: 316-5083 at 450 °C for 60 and 180 minutes

316-5083-450C-60min

In Figure 4.27 two phases are observed at the IML. The intermetallic phase adjacent to St has a darker shade. It can be interpreted that the elements involved in this phase are lighter.

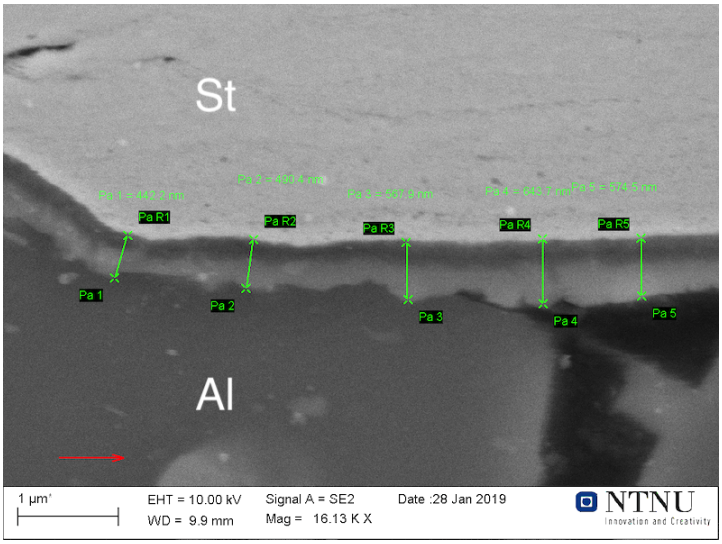

Figure 4.27.: Sample 316-5083-450C-60min at 16kx magnification. The arrow indicated rolling direction. Two phases are visible. The average of the IMC layer was measured to be 0.47 µm.

316-5083-450C-180mins

Figure 4.28 shows the intermetallic layer formed during 3 hours of 450 °C heat treatment. Two phases are observed in the intermetallic layer.

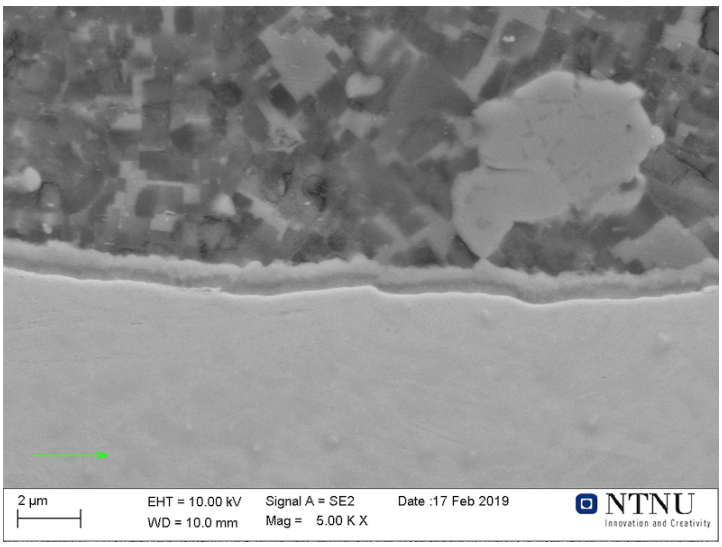

Figure 4.28.: Sample 316-5083-450C-180min at 5kx magnification. The av7rage of the IMC layer was measured to be 0.80 µm.

EDS mapping of the intermetallic layer displays a magnesium segregation in the intermetallic phase adjacent to steel, see Figure 4.29.

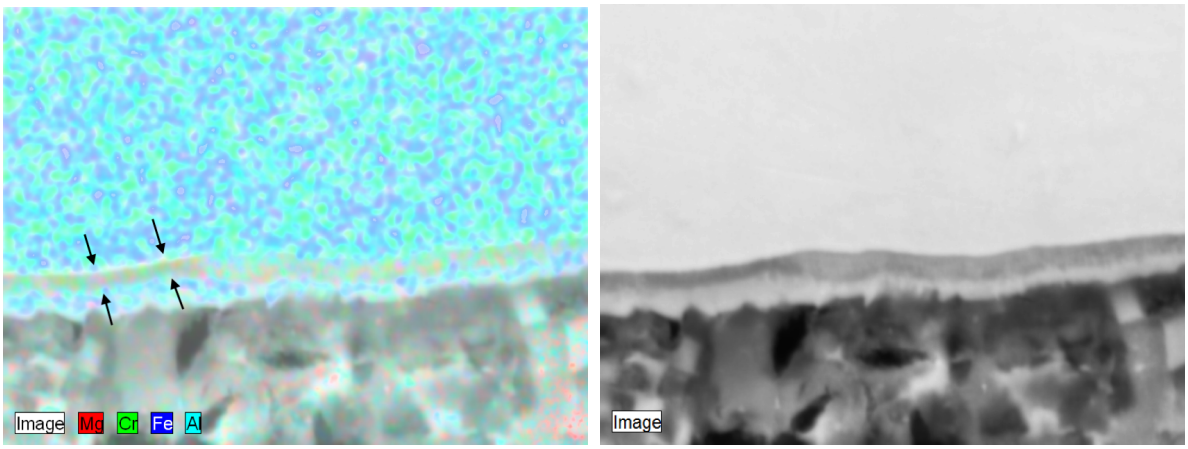

(a) **(b)**

Figure 4.29.: (a) EDS mapping of the interface of 316-5083-450C-180min showing magnesium containing intermetallic phase adjacent to St. **(b)** The area on which mapping was conducted.

4.3.3. Sample: 316-5083 at 500 °C for 10, 60 and 180 minutes

316-5083-500C-10min

The sample heat-treated at 500 °C for 10 minutes, display two phases in the intermetallic layer, see Figure 4.30.

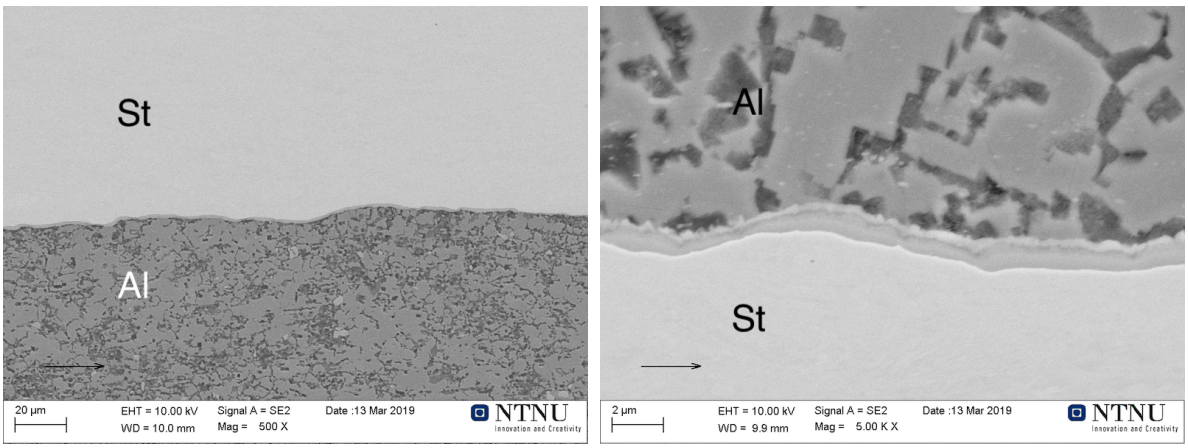

(a) **(b)**

Figure 4.30.: Micrographs of 316-5083-500C-10min at **(a)** 500 and **(b)** 5kx magnification. Two phases are visible at the interface. The average of the IMC layer was measured to be 1.1 µm.

4.3.4. 316-5083-500C-60min

Figure 4.31 displays cropped micrographs of the intermetallic layer with four phases, marked in the figure.

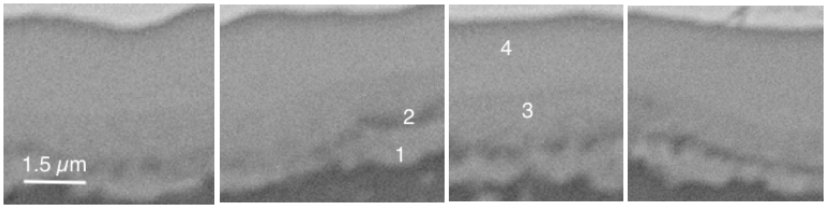

Figure 4.31.: Intermetallic layer of 316-5083-500C-60min at 5kx magnification. Four phases are visible at the IML. The avg. IML thickness was measured to be 2.8 µm.

316-5083-500C-180min

Sample heat-treated at 500 °C for 3 hours, display four phases at the IML. These phases are marked in the Figure 4.32.

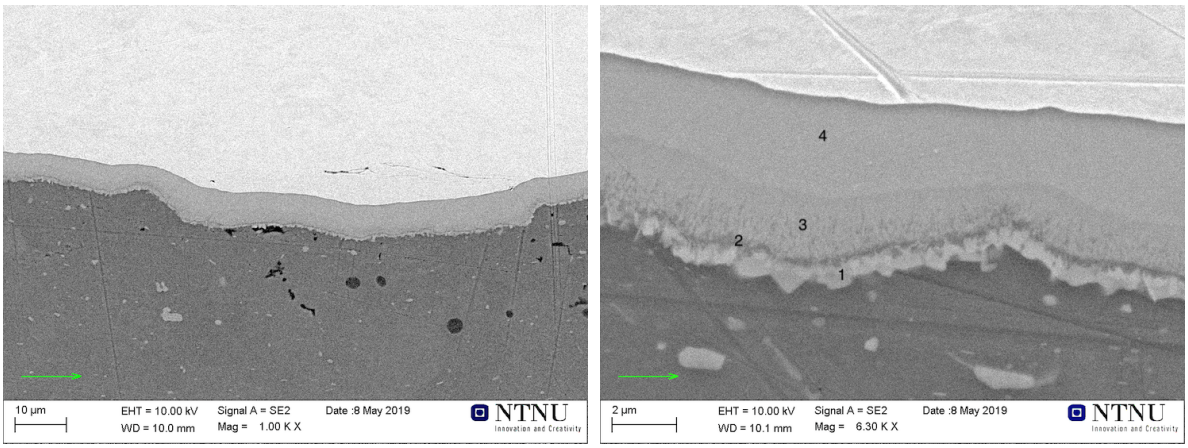

(a) **(b)**

Figure 4.32.: Micrographs of 316-5083-500C-180min at **(a)** 1kx and **(b)** 6.3kx magnification. Three phases are visible at the IML. The average of the IMC layer was measured to be 5.7 µm.

Figure 4.33 displays EDS line scan of the interface of 316-5083-500C-180min. It can be observed from the line scan that at the edge of Al-layer, at approximately 2 µm, there is a sharp rise of Fe and Ni. Right after that, a small peak in Cr and Mg is observed. After the small peak, Cr is observed to have a part throughout the whole intermetallic layer.

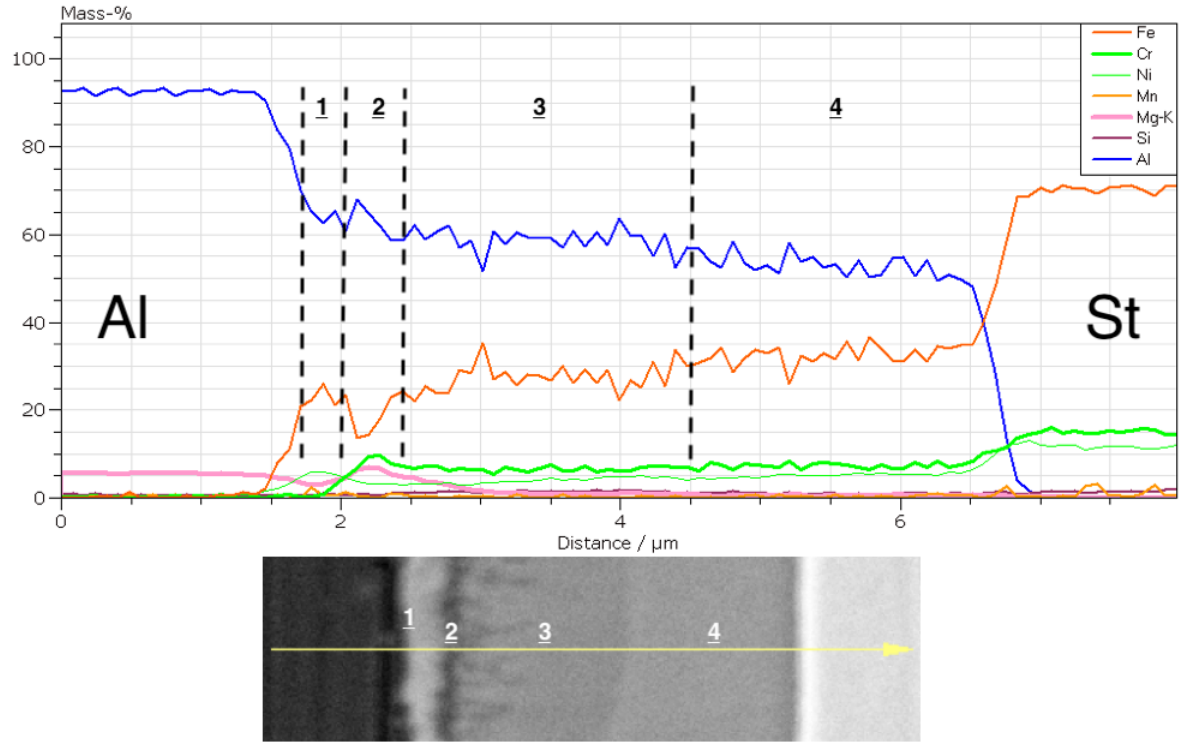

Figure 4.33.: EDS line scan of 316-5083-500C-180min. y-axis displays ZAF corrected mass percent.

To find more about the content of each phase EDS point scan was conducted on the intermetallic layer. Figure 4.34 displays the points marked and Table 4.4 the results.

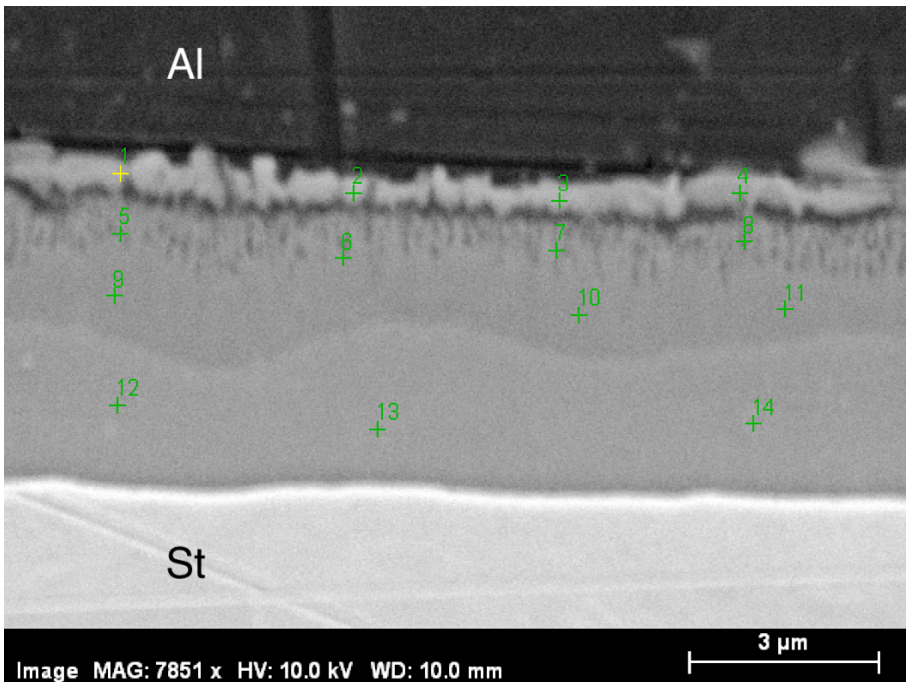

Figure 4.34.: Points marked on the intermetallic layer of 316-5083-500C-180min.

In Table 4.4 results from the point scan are displayed. One can see that the Al concentration decreases towards the St-interface. Point 11 is omitted from the result due to software crash. Mg content is significant at the Al-interface. Cr content seems to be increasing towards the St-interface.

Table 4.4.: Point scan results of 316-5083-500C-180min. See Figure 4.34 for the locations of marked points. Points 1 to 4 are marked on the protruded phase adjacent to Al-layer. 5 to 8 are marked on the porous phase. 9 and 10 are marked before the lighter phase. 12 to 14 on the phase adjacent to the St-layer. Point 11 is omitted from the results due to software crash.

Points	Al [at. %]	Fe [at. %]	Mg [at. %]	Ni [at. %]	Cr [at. %]	Mn [at. %]	Si [at. %]
1	76.89	8.54	6.43	3.07	3.04	1.13	0.91
2	75.54	12.75	5.1	2.73	1.84	1.49	0.55
3	71.76	15.04	5.25	1.81	4.36	1.34	0.44
4	81.2	9.87	3.27	3.46	0.42	0.64	1.14
5	63.75	23.44	2.96	1.61	5.21	1.48	1.54
6	64.4	23.6	2.69	1.72	5.1	1.35	1.13
7	64.97	22.55	2.7	1.7	4.94	1.19	1.95
8	65.49	17.7	5.53	1.43	5.49	1.18	3.19
9	62.57	26.04	0.74	2.36	4.78	1.27	2.25
10	60.99	28.16	0.77	2.54	4.8	1.38	1.35
12	56.68	31.65	0.38	3.03	5.34	1.45	1.48
13	58.27	30.66	0.39	3.14	5.64	1.44	0.46
14	58.64	29.3	0.39	2.98	7.38	1.32	1.97

4.3.5. Sample: 316-5083 550 °C for 60 minutes

Micrographs of 316-5083-550C-60min are displayed in 4.35. Dark patchy IML is observed near the Al-interface.

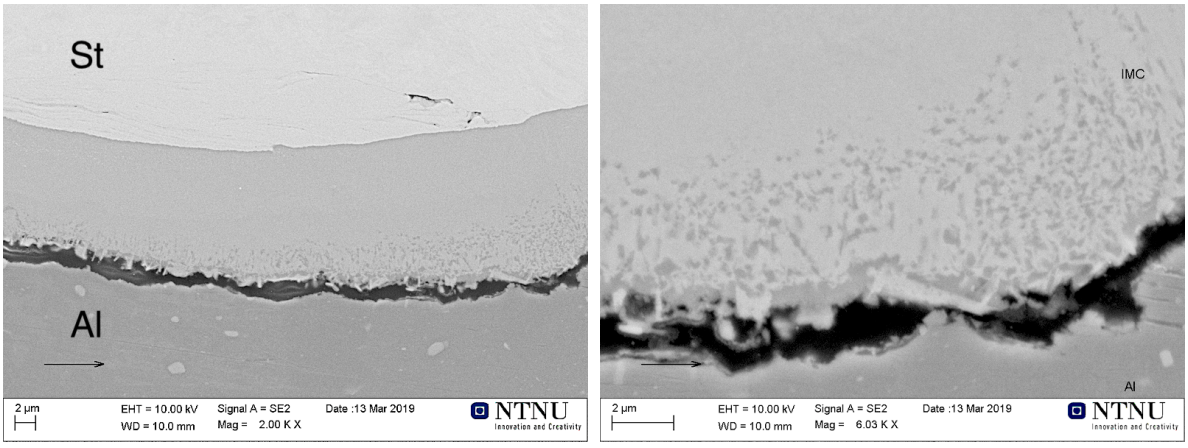

(a) **(b)**

Figure 4.35.: Micrographs of 316-5083-550C-60min at **(a)** 2kx and **(b)** 6kx magnification. Two phases are visible at the interface.The average of the IMC layer was measured to be 12.0 µm.

A line scan across the interface of 316-5083-500C-60min is shown in Figure 4.36. Huge variations in the line scan are observed. This might be due to large electron beam depth.

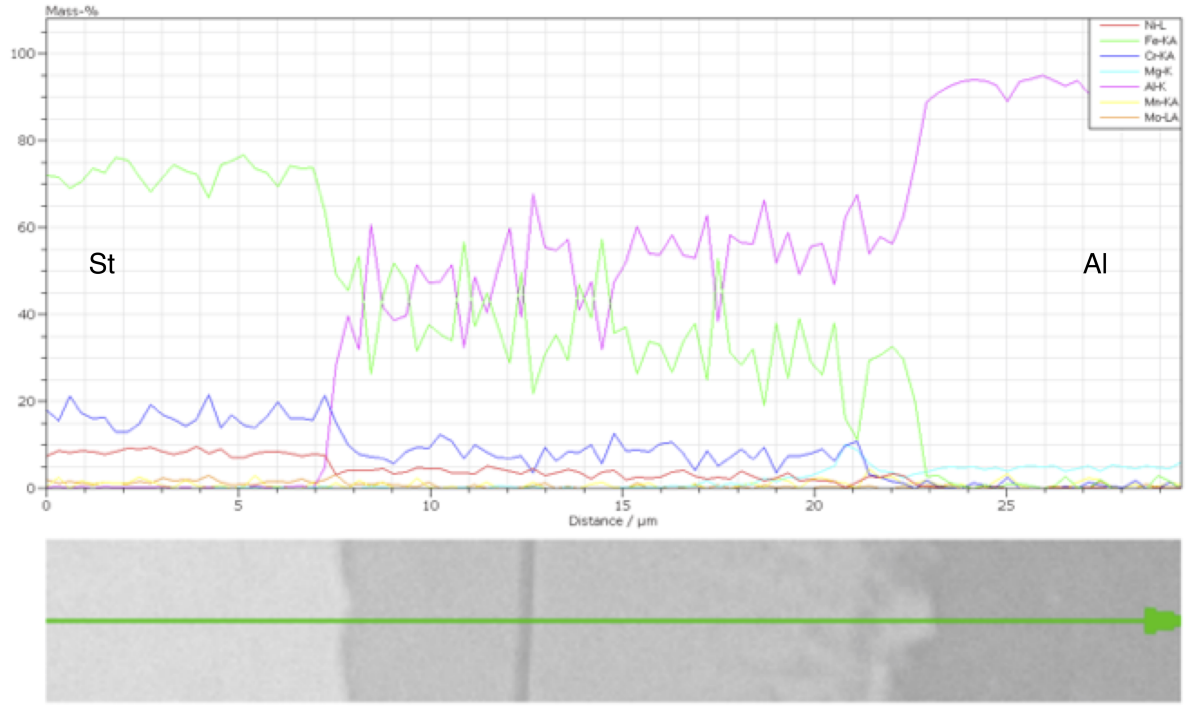

Figure 4.36.: line scan of the interface of the sample 316-5083-550C-60min. y-axis displays ZAF-correct mass percent.

Several points were marked for EDS pointscan at the intermetallic layer of 316-5083-550C-60min to find out about the composition of the phases. Figure 4.37 displays the marked points. In Table 4.5 the Al concentration seems to not differ much throughout the points. High Mg concentrations at the interface of Al is observed. Cr seems to be increasing in concentration towards St-interface.

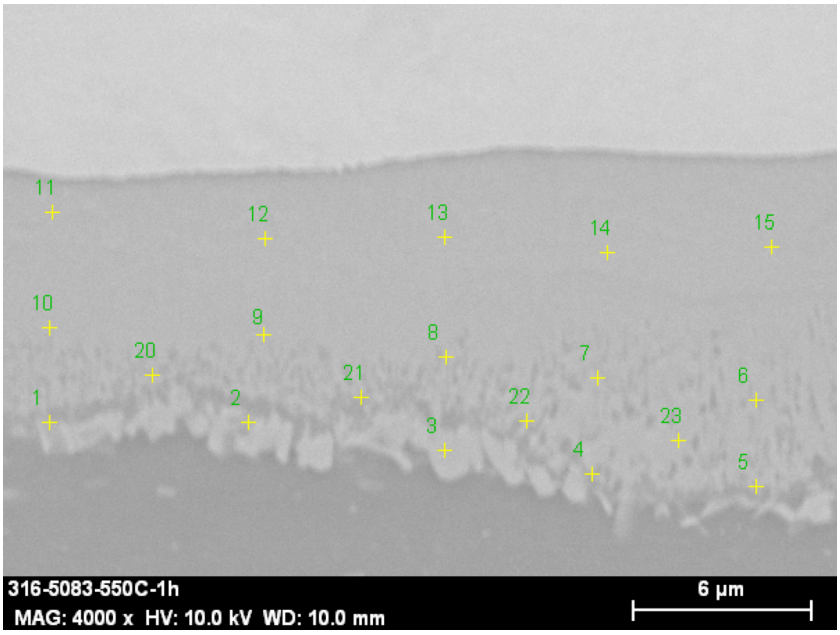

Figure 4.37.: Points marked at the intermetallic layer of 316-5083-550C-60min for EDS point scan. See results in Table 4.5.

Table 4.5.: Results from EDS scan on atomic compositions of points marked on the intermetallic layer of 316-5083-550C-60min. Points 1 to 5 are marked in the phase adjacent to Al. Points 11 to 15 are marked in the phase adjacent to St. The rest are in the area between the mentioned regions. Each layer is separated by horizontal lines.

Points	Al [at. %]	Fe [at. %]	Mg [at. %]	Cr [at. %]	Ni [at. %]	Mn [at. %]
1	73.94	12.56	7.5	2.92	1.87	1.21
2	75.14	8.34	8.99	5.12	1.54	0.86
3	73.03	19.66	1.76	0.55	3.29	1.71
4	74.21	12.59	7	3.26	1.71	1.23
5	73.61	9.89	9.59	5.02	1.2	0.69
20	76.02	11.58	5.89	4.15	1.59	0.77
21	76.27	7.92	8.37	6.31	0.8	-
22	76.17	11.65	6.18	3.47	1.64	0.89
23	72.47	19.16	2.08	2.41	2.59	1.29
6	75.19	14.45	3.69	4.01	1.99	0.66
7	73.91	1645	3.67	3.28	1.97	0.72
8	75.43	15.92	3.06	3.3	1.94	-
9	75.55	16.83	1.89	3.65	1.91	-
10	75.41	16.82	1.43	3.83	1.91	0.6
11	72.51	18.99	0.88	4.87	2.52	-
12	72.05	19.25	0.86	5.23	2.41	-
13	71.87	19.87	0.96	4.57	2.46	-
14	71.45	20.45	0.92	4.84	2.11	-
15	70.57	21.37	0.87	4.62	2.37	-

4.3.6. Summary

The thickness of IML from all the samples in 316-5083 are displayed in Figure 4.38.

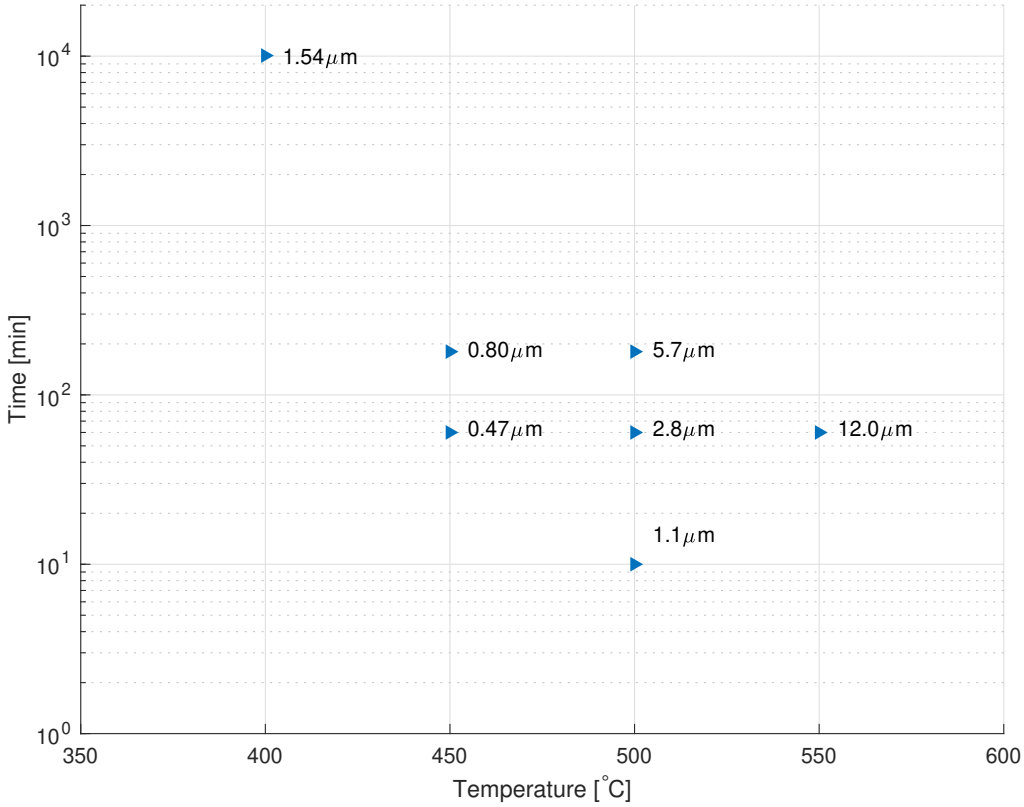

Figure 4.38.: IMC layer in all heat-treatments for 316-5083

Key findings:

316-5083-400C-1week Three phases found at the IML. Mg rich phase adjacent to St-side and Ni rich phase adjacent to Al-side.

316-5083-450C-180min Mg rich phase (or segregation of Mg) adjacent to St-side. Two phases observed.

316-5083-500C-60min Four phases observed at the IML.

316-5083-500C-180min Four phases observed. EDS line scan show intermetallic phases rich with Cr and Ni. Ni phase observed at the start of IML adjacent to the Al-side, simultaneously a dip in Mg content observed. Right after, Mg and Cr rich phase observed. The intermetallic phases also included Si.

316-5083-550C-60min Four phases observed. Intermetallic layer rich with Cr and Ni. High content og Mg observed in the phase adjacent to Al-side.

4.4. Sample: 316-6082

The 316-6082 samples used for heat treatments were taken from a batch of other samples. The average total reduction in thickness was measured to be 63 ± 2.5%. The total reduction percentage of the sample 316-6082 was measured in OM by taking 20 measurements at four different places.

Heat treatment plan for the samples 316-6082 is given in Figure 4.39.

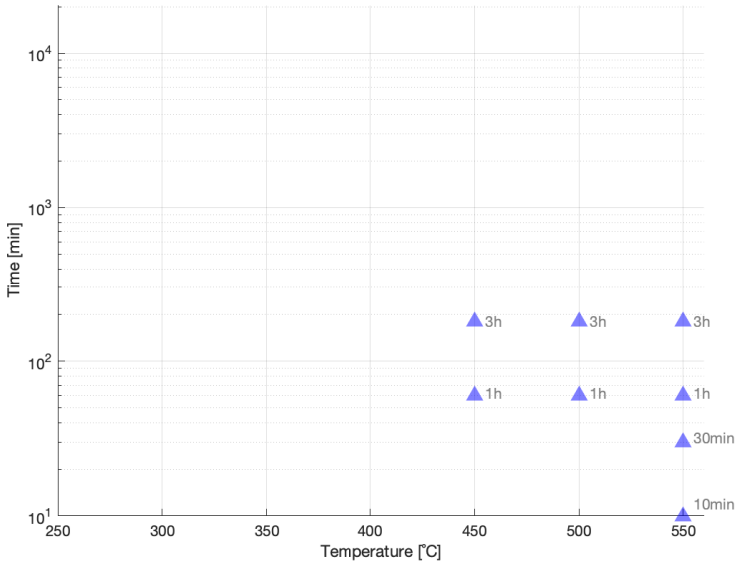

Figure 4.39.: Heat treatment plan for 316-6082

4.4.1. Sample: 316-6082 at 450 °C for 60 and 180 minutes

316-6082-450C-60min

No intermetallic layer was observed at 450 °C for 60 minutes of heat treatment, see Figure 4.40

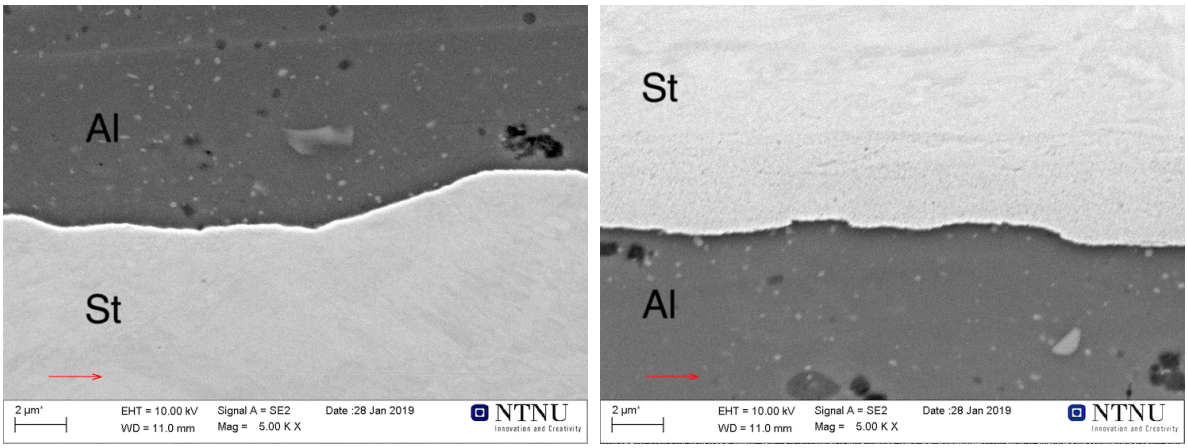

(a) **(b)**

Figure 4.40.: Micrographs of 316-6082-450C-60min at **(a)** 5kx and **(b)** 5kx magnification. No intermetallic layer observable.

316-6082-450C-180min

For heat treatment at 450 °C for 180 minutes, the intermetallic observed was formed fragmented. No continuous layer was observed.

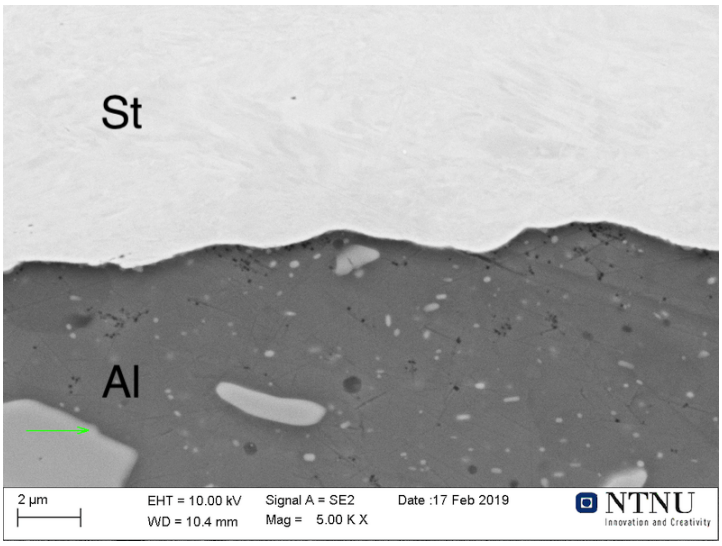

Figure 4.41.: Sample 316-6082-450C-180min. The average of the IML layer was measured to be 0.07 µm.

4.4.2. Sample: 316-6082 at 500 °C for 60 and 180 minutes

316-6082-500C-60min

At 500 °C for 60 minutes of heat treatment, a very thin fragmented intermetallic layer was observed, see Figure 4.42. The IML is observed to be forming into the Al-interface.

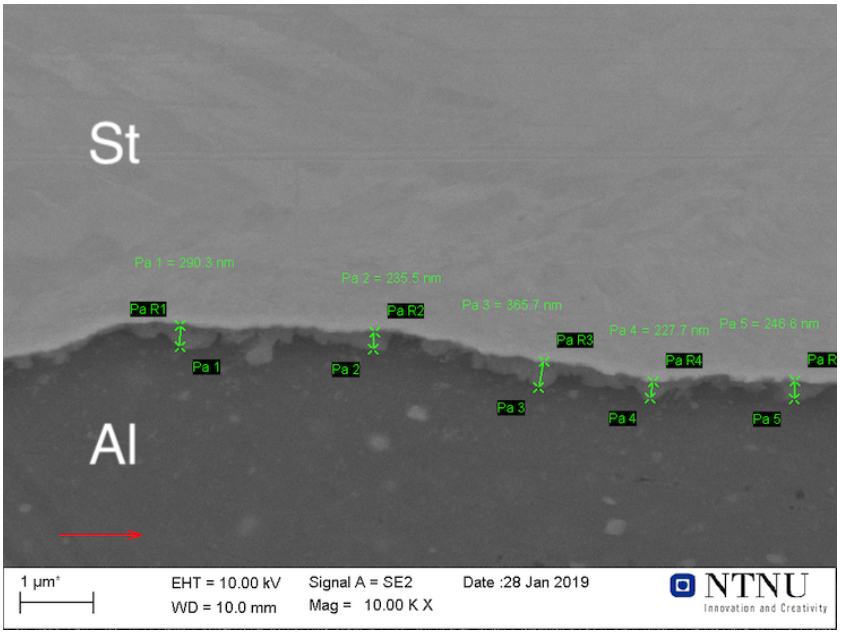

Figure 4.42.: Intermetallic layer in 316-6082-500C-60min. The average of the IML was measured to be 0.25 µm.

316-6082-500C-180min

A continuous intermetallic layer was observed at 500 °C for 3 hours of heat treatment, see Figure 4.43.

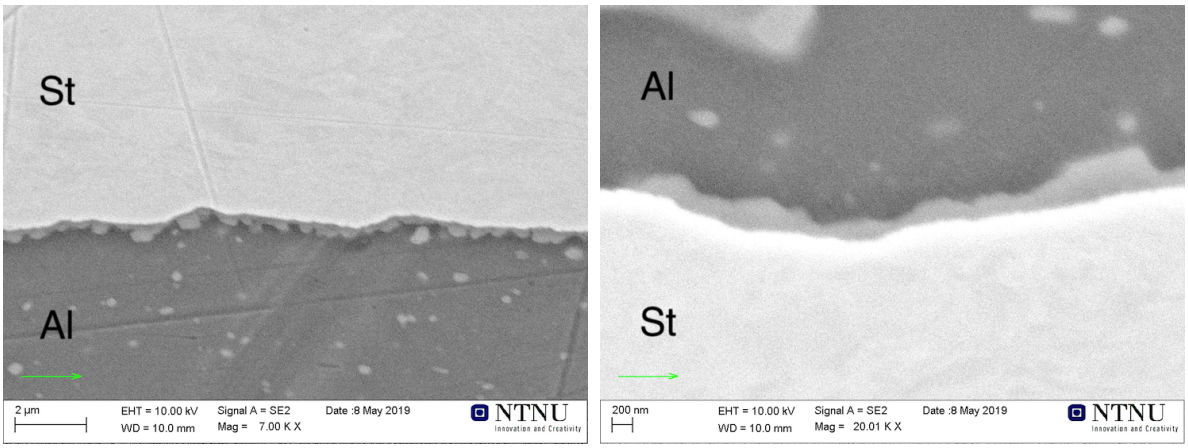

(a) **(b)**

Figure 4.43.: Micrographs of 316-6082-500C-180min at **(a)** 7kx and **(b)** 20kx magnification. The average of the IML layer was measured to be 0.236 µm.

4.4.3. Sample: 316-6082 at 550 °C for 10, 30, 60 and 180 minutes

A uniform intermetallic layer was observed at 550 °C for 10 minutes heat treatment.

316-6082-550C-10min

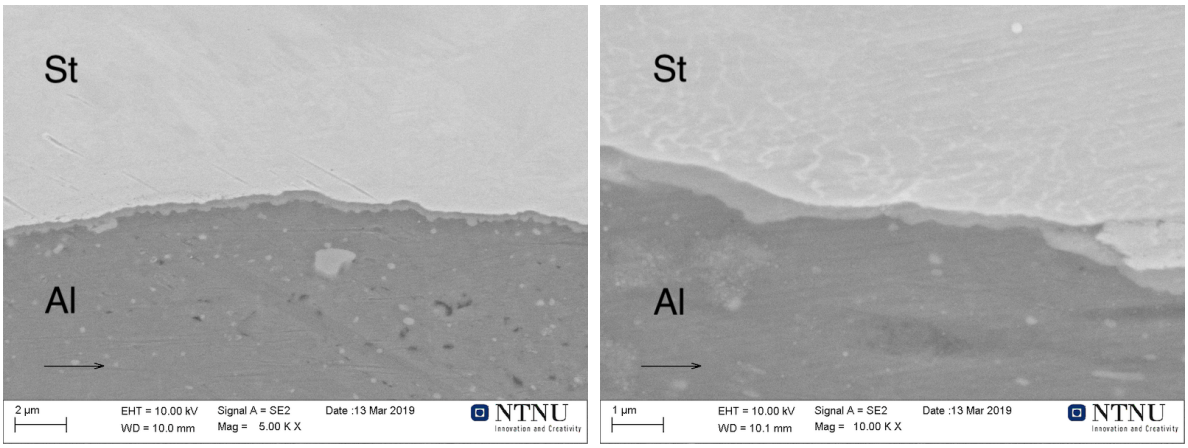

(a) **(b)**

Figure 4.44.: Micrographs of 316-6082-550C-10min at **(a)** 5kx and **(b)** 10kx magnification.The average of the IML layer was measured to be 0.5 µm.

316-6082-550C-30min

At 550 °C for 30 minutes of heat treatment, two phases were observed at the intermetallic layer.

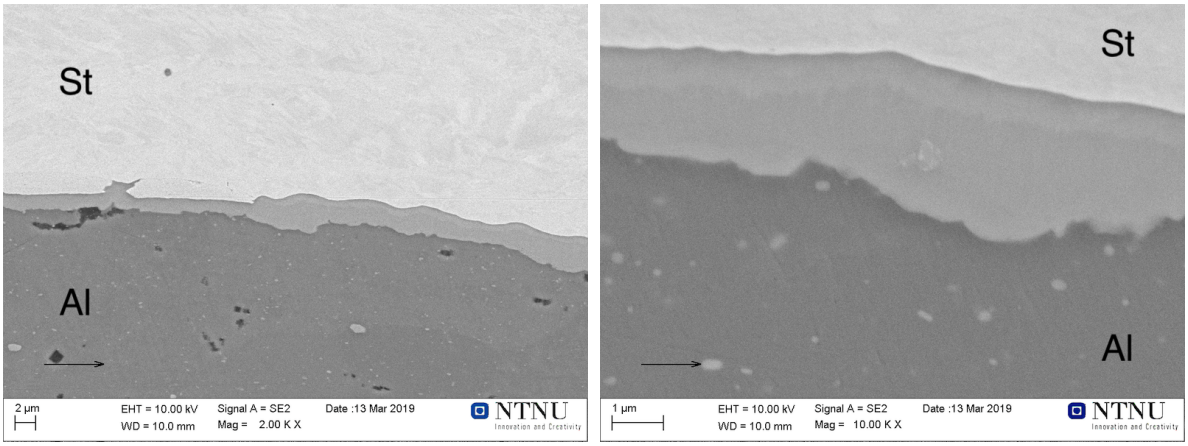

(a) **(b)**

Figure 4.45.: Micrographs of 316-6082-550C-30min at **(a)** 2kx and **(b)** 10kx magnification. Two phases in the intermetallic layer is visible. The average of the IML layer was measured to be 2.3 µm.

316-6082-550C-60min

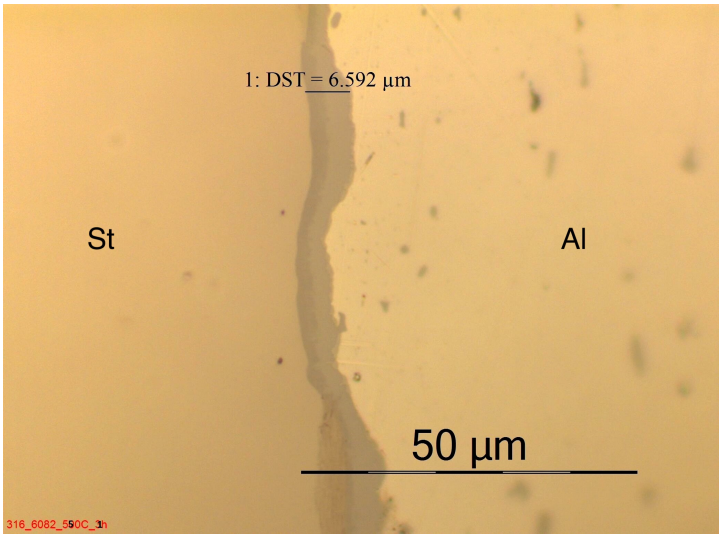

Figure 4.46.: Sample 316-6082-550C-60min at 100x magnification. Two phases at the intermetallic layer are visible.The average of the IML layer was measured to be 5.71 µm.

Nanoindentaion tests were conducted on this sample to measure hardness and reduced elastic modulus of the intermetallic layer, see Figure 4.47.

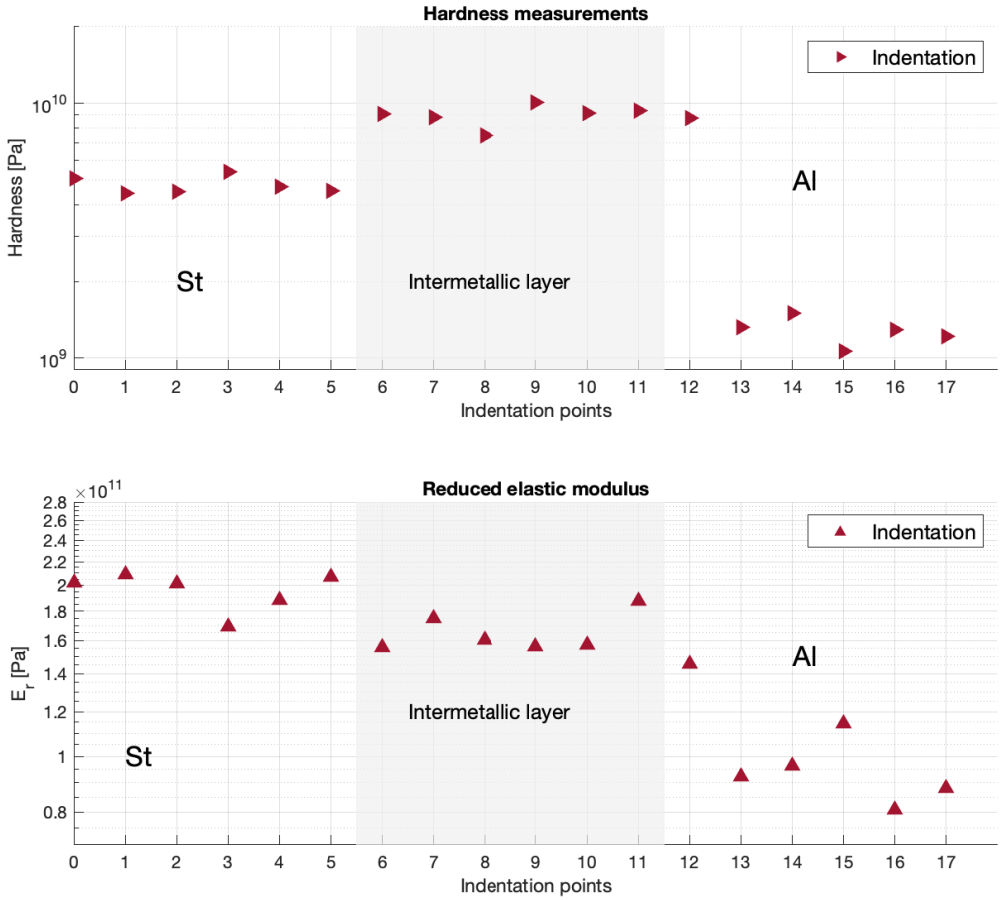

Figure 4.47.: Nanoindentation tests conducted on 316-6082-550C-60min.

316-6082-550C-180min

Three phases were observed at the intermetallic layer of 316-6082-550C-180min.

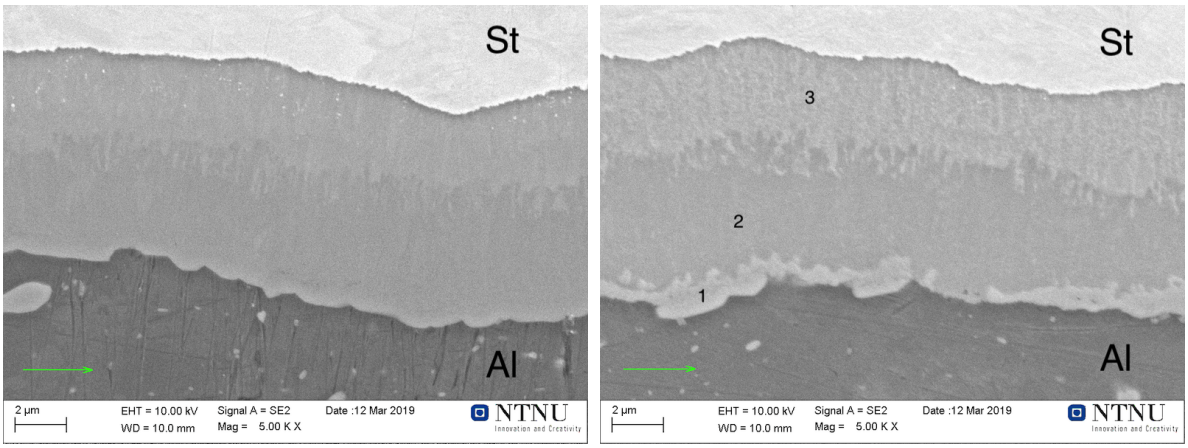

(a) **(b)**

Figure 4.48.: Micrographs of 316-6082-550C-180min at **(a)** 5kx and **(b)** 5kx magnification. Three phases in the intermetallic layer is visible, marked phases. The average of the IML layer was measured to be 8.0 µm.

Figure 4.49 displays line scan of the interface. Ni and Cr are observed in the intermetallic layer adjacent to St-side. Cr concentration decreases towards Al-rich phases adjacent to Al-side. Si concentration increases in towards IML-Al-side.

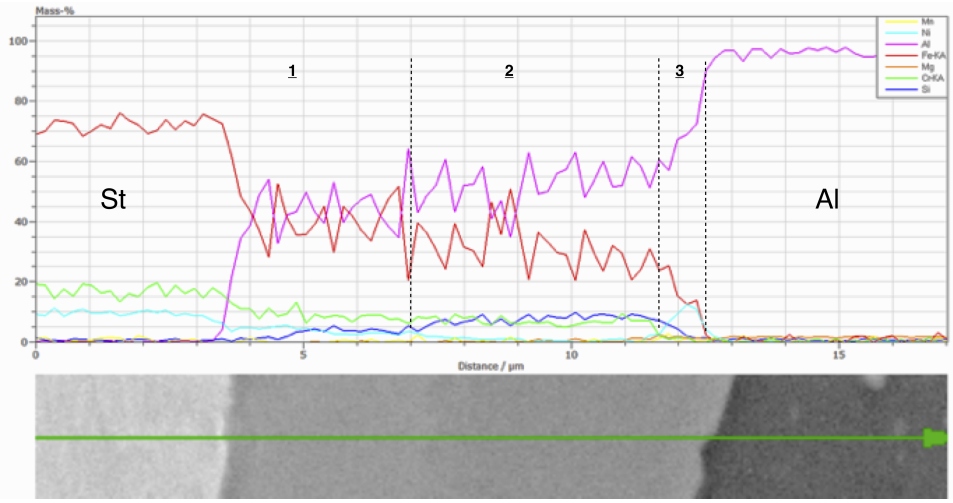

Figure 4.49.: Line scan of 316-6082-550C-180min across the interface. y-axis displays ZAF-corrected mass percent.

The evidence of Ni-rich phase is supported by the EDS mapping scan displayed in Figure 4.50. A clear Si-rich phase is formed after the Ni-rich layer at the Al-interface. Si concentration seems to decrease towards St-interface.

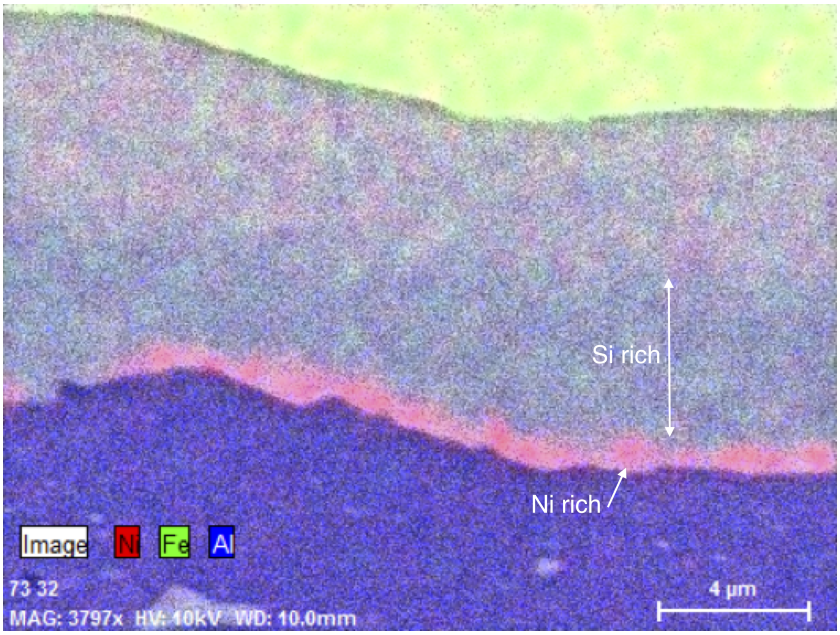

Figure 4.50.: EDS mapping of 316-6082-550C-180min showing the three phases and Ni compounds near the Al side.

4.4.4. Summary

Intermetallic thickness of each sample is displayed in Figure 4.51.

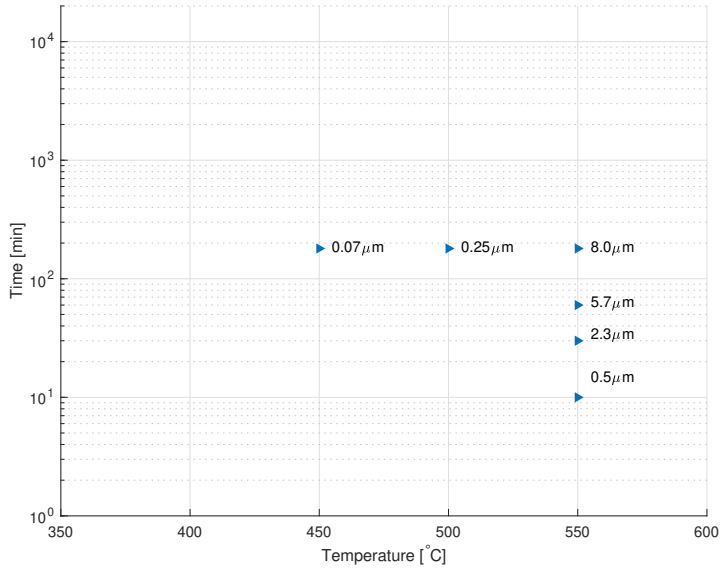

Figure 4.51.: IML layer in all heat-treatments for 316-6082

Key findings:

IML No intermetallic layer was formed with heat treatments below 500 °C. Fragmented intermetallic formation observed in heat treatments layer of 500 °C for 60 minutes. Uniform IML formed at 550 °C.

IML phases Three phases observed at heat treatments of 550 °C for 30 minutes. The phases more distinct at heat treatments of 550 °C for 180 minutes.

Nanoindentation Brittle intermetallic IMC were observed. Have data to compare my results with.

Ni Ni-rich IMC adjacent to the Al-side were observed. Most likely IMC: Al_3Ni_2 and Al_3Ni.

Si Significant Si concentrations were observed in the intermetallic phase of 316-6082-550C-180min, most probable AlFeSi-rich phase.

Cr Significant Cr concentration was observed in intermetallic layer. Cr mass concentration observed to be increasing in the IML towards Al-side.

Chapter 5.

Discussion

In this chapter, we will discuss the results obtained for each sample combination and temperature regime.

5.1. 355-5083

5.1.1. 355-5083-300C

From the observations in Figures 4.2 and 4.3 and Table 4.1, we can conclude based on the atomic weight ratios of Fe/Al that there are two phases present at the intermetallic layer. The dark line visible in SEM micrographs at the interface is expected to be from rapid quenching, where higher degree of contraction due to thermal stresses in aluminium breaks the weak bonds at the interface.

It is observed from Table 4.1, that the dark-patchy intermetallic phase at the vicinity of Al-interface is predominantly $FeAl_3$ [46]. However, in literature [49, 74–76] use different nomenclature [77] for the θ-phase, i.e. Fe_4Al_{13} - which is the actual stoichiometry [78]. The average atomic percent ratio was calculated to be 2.190 ± 0.034 for $FeAl_3$. The Walser-Bene model predicts formation of $FeAl_3$, the is in accordance to prediction. The rapid growth of $FeAl_5$ is due to 30% vacancies along the [001] direction of the orthorhombic cell structure [74]. This allows greater diffusion along the c-axis [30]. At 300 °C annealing temperature, there is no apparent distinction between minor and major phases of Fe-Al IMCs in the intermetallic layer, due to low contrast between them in SEM.

In Figure 4.3, the disparity between St and Al mass percentages are observed to be climbing from the lower ends of 40% to 50%. This is an indication of another phase present at the St-interface, namely Fe_2Al_5, with an average weight ratio Al/Fe of roughly 0.76 ± 0.11.

EDS line scan in Figure 4.3 supports the evidence from point scans in Table 4.1 that the expected intermetallic phases present are Fe_2Al_5 and $FeAl_3$.

5.1.2. 355-5083-400C

High temperature heat treatment show faster growth rates in the formation of the intermetallic layer. At 400 °C the columnar shape of Fe_2Al_5 is already visible at 30 minutes heat treatment. A 220% increase in IML growth is observed after increasing the duration of heat treatment by 20 minutes. The micro-voids observed at the Al-interface in Figures 4.4a and 4.5 are due to faster diffusion of Al-atoms towards St/IML compared to Fe-atoms towards Al/IML [79].

5.1.3. 355-5083-450C

At 450 °C heat treatment, three phases are observed already at 2 minutes duration. However, the phases were not visible, Figure 4.6. From the EDS mapping in Figure 4.7c, one can see the three plateau in the ZAF-corrected atomic percentages making a reasonable argument for the existence of three phases in the intermetallic layer. From Table 4.2, we can predict that the phase present in the IML are Al-/ $FeAl_3$ / Fe_2Al_5 / $FeAl_2$ /-St. In Figure 4.7c, it can be observed that the major phase is Fe_2Al_5 and the minor phases are $FeAl_3$ and $FeAl_2$. Notice the concentration gradient of Mg increasing towards Al-interface. The results from point scans did not show significant amounts of Mg ($\approx <$ 0.7at.%) at the Al-interface. However, the concentration does seem to increase. The "segregation" of Mg is more evident in higher temperature treatments, which will be dealt with in later sections.

The thickness of the intermetallic layer increases with the duration of the heat treatments. This gives weight to the observations in literature that the growth mechanism of the intermetallic layer is diffusion controlled [35, 42, 51, 80–82].

Growth kinetics

By inserting the IML thickness values for all the samples heat treated at 450 °C in equations (2.3) and (2.2), we get $n = 0.632$ and $k = 0.24\,\mu m\,s^{-1/2}$. The value of $n = 0.63$ means that the controlling process of intermetallic growth is a mixed mechanism of volume diffusion and grain boundary diffusion. It should be noted that this conclusion is based on few heat treatment duration points at 450 °C. In literature the consensus is mainly on volume diffusion growth kinetics [83].

Furthermore, the growth rate constant is closer to the value reported by Springer et al. [37], $k = 0.176\,\mu m\,s^{-1/2}$ for low carbon steel and pure aluminium at 450 °C heat treatment and the value reported by Bobzin et al.[84], $k = 0.25\,\mu m\,s^{-1/2}$ for low carbon and AA7075 alloy (Si 0.4 wt.%) at 500 °C heat treatment. It should be noted that not all researchers use the same unit for the growth constant, depending on how they have used they write equation (2.2). Some places it is $m^2\,s^{-1}$ [38] and others use $\mu m\,s^{-1/2}$ [37].

It would be possible to calculate activation energies of IMC formation by Arrhenius relationship, $k = k_0 \exp(-Q/RT)$, if we had the same amount of points for other temperatures as well.

Nanoindentation

For nanoindentation, a sample was chosen with thick enough IML so that all the phases are visible. The results obtained in Figure 4.11 are not in agreement with the literature [49, 85–87]. The hardness values at the IML are lower than the matrix, a contradiction to their brittle nature. In Table 5.1 average hardness values of IMCs from several papers are presented. It should be noticed that the sample on which the nanoindentations were made had delaminated, making it difficult to find areas where the IML was attached to either side Al/St. Also the load function for hardness measurements was 500 µN, see Appendix B.1**(a)**.

Table 5.1.: Average hardness measurements of IMCs found in literature and hardness of IMCs in 355-5083-450C.

	$FeAl_3$ [GPa]	Fe_2Al_5 [GPa]	Ref.
	7.8	10	[49]
	7.8	8.5	[85]
	-	12.1	[86]
	6	8.5	[87]
Avg.	**7.2**	**9.78**	
	0.24	0.22	current work

EPMA results

EPMA results in Figure A.1**(b)** confirm our observations of the existence of three phases at the IML. Mg segregation is observed at the Al-interface. Mg segregation to grain boundaries have been observed before in past studies [88, 89]. Mg segregation makes the Al-Mg alloys susceptible to stress-corrosion, therefore has been extensively studied, [90]. When Al-Mg alloys are under severe plastic deformation (SPD), they produce non-equilibrium grain boundaries which contain an excessive density of extrinsic dislocations. These non-equilibrium grain boundaries exhibit features like long-range elastic stresses and enhanced free volume which accommodates solute atoms [91]. This excess density of dislocations turns into the pinning sites for Mg and thus causing Mg segregation which in turn forms precipitates of Al_3Mg_2 [90]. In another study by Kenji et al.[92] observed formation of $MgAl_2O_4$ layer in friction stir welding of 5083/S10C steel.

5.1.4. 355-5083-500C

At 500 °C the finger-like morphology of the Fe_2Al_5-phase is more visible. The mechanism behind the formation of columnar/finger-like structure is explained by the work of Takata et al. [93]. A schematic showing the microstructure and columnar growth of Fe_2Al_5 phase is presented in Figure 5.1.

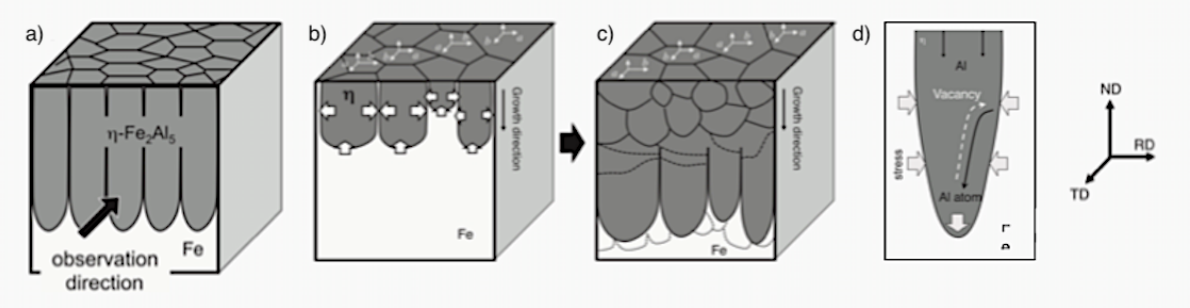

Figure 5.1.: A schematic of columnar grain growth of Fe_2Al_5 [93]. **(a)** overview of the observation direction **(b)** stress field generated by the formation of Fe_2Al_5 in Fe **(c)** columnar growth of Fe_2Al_5 creating high density dislocations in Fe **(c)** vacancy flow in the Fe_2Al_5 phase and the stress induced by Fe

Takata et al.[93] describes that the columnar shape of Fe_2Al_5 is due to volume expansion of its lattice in Fe. Iron has bcc structure and Fe_2Al_5 having the orthorhombic oC24 structure, is bigger. As the transformation from Fe $\longrightarrow$ Fe_2Al_5 occurs, it is accompanied by a volume expansion. It has been observed that the Fe_2Al_5 has accelerated diffusion along its [001] direction [39]. The Fe_2Al_5 phase lattice expansion along a-, and b-axis is met by strain from Fe. Growth of Fe_2Al_5 under strain creates a tensile stress and compression stress along and perpendicular to the growth direction. This causes vacancies to flow into the compression stress field by Nabarro-Herring creep diffusional creep mechanism [93].

5.2. 355-6082

5.2.1. 355-6082-300C

In Figure 4.16, no intermetallic layer is visible. The alloy 6082 is an Al-Mg-Si alloy and with a higher amount of Si in this alloy, it impedes the growth of the intermetallic layer. In comparison to 355-5083-300-1week, the intermetallic growth was non-existent. In the EDS scan in the same figure, a spike in Si and Mg is observed. In a similar study by Arbo et al. [94], they observed that the IMC adjacent to the Al-interface was AlFeSi, see Figure 2.3. There is also a little spike in Mg at the interface, this might indicate existence of Mg_2Si precipitates, as reported by Narsimhachary et al. [95] and Reeb and Weidenmann [96]. The EDS line can indicates that the IML thickness is $<<$ 1 µm.

5.2.2. 355-6082-450C

Heat-treated samples at 450 °C in Figures 4.17 and 4.18 show a thin IML. However, the IML is observed to have fragmented formation. It shows that the time and temperature required to facilitate interdiffusion of Fe-Al at the interface for the growth of IML was not sufficient.

In Figures 4.17 and 4.18 it is observed that the growth of the IML is at the Al-side. The Walser-Bene model [97], predicts $FeAl_3$ to be the first stable phase to form in a solid-solid reaction. This model predicts that the first phase nucleated in solid-solid reaction is the phase immediately adjacent to the low-temperature eutectic in the binary phase diagram [97]. In comparison to 355-5083 composites, the IML thickness in 355-6082 is much thinner at the same heat treatment temperature. This suppressed growth kinetics of IML thickness in 355-6082 can be argued to be mainly because of higher Si additions in the 6082 alloy [45, 47, 51, 98]. However, because of very thin IML, EDS measurements were not best suited for the characterization of IMCs due to pear-shape penetration depth of electrons which would give rise to compositional error [78]. At 450 °C heat treatment, we can assume that the IMC formed at the interface observed are $FeAl_3$ with local Si enrichment as reported by Reza-e-Rabby et al. [99], $FeAl_3$ with Si enrichment at the grain boundaries of the IMC [39], or AlFeSi as reported by Arbo et al. [19]. The mechanism behind the suppression of intermetallic layer growth by addition of Si is not well understood [100]. There are several hypotheses concerning the role of Si. The hypothesis put forward by Nicholls [101] proposed an interaction of Si atoms with the crystallographic arrangement of Fe_2Al_5, Yin et al. [48] proposed that Si reduces the activation energy for the Fe_2Al_5 formation, and Kurakin [45] and Zhang et al. [102] proposed that formation of ternary compounds act as a diffusion barrier.

5.2.3. 355-6082–(500C & 550C)

In stark comparison to 500 °C heat treatment of 355-5083, at 500 °C and 550 °C. The samples showed extensive growth of the IML layer. The growth increased approximately $>1000\%$ but still lower than 355-5083 samples. The retardation of IML growth can be due to the high amount of Si (0.7–1.30 wt.%) in 6082. In Figures 4.20 and 4.21 delamination of samples is observed attributed to the thermal stresses. The expansion coefficients of St and Al (11–12.5 µm/(m K) for Al and 21–24 µm/(m K)) [74]. In Figure 4.19b voids are observed at the Al-interface. These voids are attributed to faster diffusion of Al atoms compared to that of Fe [79]. Similar results were obtained by Kim and Hong [79], where the roll bonded composites of STS304 and Al1050 were annealed at 550 °C for 12 & 24 hours with IML thicknesses of 25 µm and 32 µm, respectively. This shows that even after prolong heat treatments the Si content retards IML growth considerably. The IMCs Kim and Hong observed at the interface, through XRD, were in the sequence Al-/ Fe_4Al_{13} / Fe_2Al_5 / $FeAl_2$ / Fe_3Al /-St.

However, the characterization of IMCs through transmission electron microscopy (TEM) in St/Al interface has identified many other phases. The phase diagram of Al-Fe-Si shows several phases which form at 500 °C and 550 °C, see Figure 5.2. Shin et al. [82] through hot dipping of Al-Si/St identified $\tau_5(Al_8Fe_2Si)$ at the Al-interface and $\tau_1(Al_2Fe_3Si_3)$ phase in the Fe_2Al_5 phase. It should be noted that at 550 °C Fe_4Al_{13} can dissolve 4 at.% Si, Fe_2Al_5 dissolves 2 at.% Si, and $FeAl_2$ dissolves about 1 at.% Si [103]. Thus, observations from EPMA, see Figure A.2, together with literature, we hypothesis that the phases in the IML are in sequence of Al-/ AlFeSi / Fe_4Al_{13} / Fe_2Al_5 enriched with Si precipitates or τ_1 /-St.

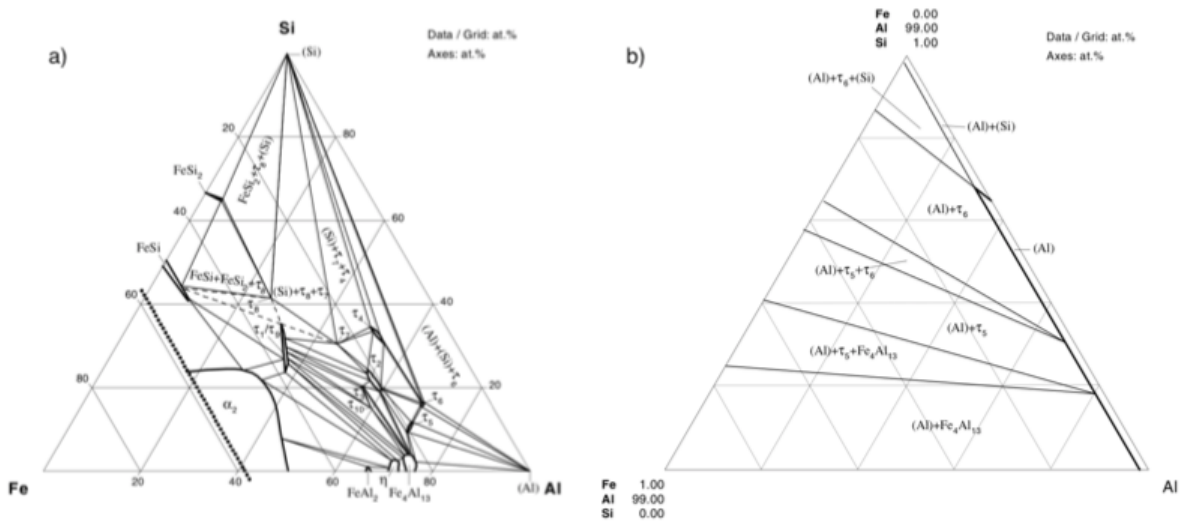

Figure 5.2.: Ternary phase diagram of Al-Fe-Si. **(a)** Partial isothermal section at 550 °C **(b)** Isothermal section of Al-corner at 500 °C [103].

5.3. 316-5083

In sample preparation of 316-5083, few of them suffered pit corrosion due to usage of DP-Blue Lubricant. The corrosion is transgranular and the anodic pits are formed at the second phase β strengthening particles [104].

5.3.1. 316-5083-400C

At 400 °C the growth of the IML is moderately slow, compared to 355-5083. It should be noted that despite the low concentration of Si in 5083-alloy, the steel grade 316L has 0.336 wt.% Si and other major alloying elements like Ni and Cr. The alloying elements have certainly retarded the intermetallic layer growth after prolong heat treatment time. In Figure 4.24(b), a dark phase is observed at the middle of the IML, meaning that the IMC has lighter elements. From the EDS line scan in Figure 4.25, one can see that there are three phases observed at the IML. The phase at the Al-interface side seems to have Ni a spike in concentration gradient just before reaching the first plateau of Al concentration, marked "Phase 1". Ni concentration gradient dies off in the region marked "Phase 2" with a small climb in Mn concentration is observed. In the region "Phase 3" a dip in the Fe concentration is observed with a concurrent spike in Mg and Cr concentrations.

It should be noted that due to a very thin layer of IML in Figure 4.26, and large pear-shaped electron penetration depth, the matrix below will be contributing to the signals as well. This will induce errors in the compositional data detected in Table 4.3. Based on thermodynamic data [105], there are three stable ternary phases at the Al-rich region of the Al-Fe-Ni phase

diagram, i.e. τ_1 $(Ni, Fe)_2Al_9$ with compostion 82 at.% Al 4.4 to 11.1 at.% Fe, and τ_2 & τ_3 which are found at higher temperature.

The τ_1 ternary phase resembles the IMC Fe_2Al_9. Szczepaniak [106] identified via EBSD, TEM and via *in-situ* TEM heating characterization that Fe_2Al_9 is the first IMC which forms towards Al, due to Fe-enriched particles in the aluminium adjacent to the steel. She argued that growth mechanism favours particles by their size. Thereafter, due to diffusion flux of Al phase like Fe_4Al_{13} is formed at the expense of Fe_2Al_9. Hence, our postulation on the possible IMC found at the points 1,7,8,9, and 13 in Table 4.3 and "Phase 1" in Figure 4.25, is $\tau_1(Ni, Fe)_2Al_9$. In the same figure at.% ratios of "Phase 2" is approximately equal to that of Fe_2Al_5, see Figure 2.2. In the "Phase 3"-zone the concentration gradient of Fe has the lowest point while Mg and Cr have their peaks. This can signify either quaternary phase IMCs. The literature on IMCs with Cr and Mg was scarce. However, in the Al-rich corner of the Al-Mg-Cr phase diagram, at 400 °C, 450 °C, and 500 °C, there exists only one ternary phase, i.e. $Al_{18}Cr_2Mg_3$ [107]. This, however, does not explain the 10 at.% Fe observed in Figure 4.25 at the "Phase 3"-zone.

Furthermore, in hot dipping experiments of 316L in molten aluminium Barbier et al. [108] and Dybkov [40] found the phases to be: Al-/ $(Fe, Cr, Ni)Al_3$ / $(Fe, Cr, Ni)_2Al_5$ /-St. Their work, however, does not explain the growth mechanism behind it. As one can see that both identified phases are in the form of the major and minor phases at the IML and have same molar volumes [109] as $FeAl_3$ and Fe_2Al_5.

Hence, we postulate that the points 10 to 12, in Figure 4.3 are likely to be $(Fe, Cr, Ni)_2Al_5$ and points 2 to 6 were not identifiable by only EDS measurements.

5.3.2. 316-5083-450C

Heat-treated samples at 450 °C did not show extensive growth of IML. At 60 minutes of heat treatment, the IML is observed to be at the Al-interface. This suggests the formation of IMCs of $Fe_4Al_{13}/FeAl_3$-type. At 180 minutes, the Fe_4Al_{13}-type phase is not visible, and the IML is observed be grown in the St, suggesting Fe_2Al_5-type phase is present. EDS mapping in Figure 4.29 shows high concentrations of Mg and Cr.

5.3.3. 316-5083-500C

At 500 °C heat treatment already after 10 minutes the IML thickness is observed to be increased 137%. The IMCs are distinguishable by the porous layer of $FeAl_3$ phase preceding Fe_2Al_5. At 60 minutes heat treatment four phases are observed at the IML. The high temperature and longer duration time increased the diffusion flux of Al into the St-layer. In Figure 4.33 EDS line scan and Table 4.4 presents the distinct layers formed. The first phase to form might be presumably expressed as $(Fe-Ni)Al_3$ [110] and the second phase $(Fe, Cr)Al_3$ or $Al_{18}Cr_2Mg_3$. The third phase is observed to have a constant concentration gradient of Cr, and for Ni increasing concentration gradient towards St-interface. This could point at

phases like (Fe, Cr, Ni)Al_3, which resembles structure of $FeAl_3$. The fourth phase marked in Figure 4.33 is presumably expressed as (Fe, Cr, Ni)$_2Al_5$, which has the resemblance to the structure of Fe_2Al_5.

5.3.4. 316-5083-550C

At 550 °C substantial growth of intermetallic layer was observed at 1 hour duration. The same characteristic porous $FeAl_5$ phase is observed near the Al-interface. The EDS line scan in Figure 4.36 is discarded due to large uncertainties in the atomic percentages, as it can be seen as large oscillations in the scan lines. This uncertainty is caused by the high electron beam depth. Furthermore, in the Fe-Al phase diagram, an important transformation occurs, i.e. FeAl $\rightleftharpoons$ Fe_3Al at 545 °C. However, from the point scans this phase is not identified. At higher temperatures the Al diffusion into Fe seems to be considerably increased. From the composition of elements obtained from Table 4.5, we conclude that the phase composition is similar to that of 316-5083-500C but with wider phases. Furthermore, EPMA results in Figure A.3(b) does not show distinct phases. Mg segregation is observed by its increasing concentration gradient towards Al-interface. High concentration of Ni is also observed at the Al-interface giving weight to (Fe – Ni)Al_3-type phase.

5.3.5. 316-6082-(450C&500C)

Thin IML thickness was observed at heat treatments at 450 °C and 500 °C. The IML growth kinetics in 316-6082 is severely suppressed by Si content. Here, Cr and Ni alloying elements also could play a role in the retardation of IML growth. The IMC formed show similar characteristic of Fe_4Al_{13}.

5.3.6. 316-6082-550C

Increase in IML thickness was observed at 550 °C 30 minutes heat treatment. As the duration of heat treatment is increase a Si rich Fe_2Al_5 is observed with characteristic columnar grains. EDS line scan in Figure 4.49 display the three phases. The phase "3" near the Al-interface shows negative concentration gradient of Fe and spike in Ni concentration, which leads us to conclude that this phase presumably be expressed as $NiAl_3$. The phase "2" has high concentrations of Si and Cr. Further investigation revealed that the main intermetallic phase found in 6082-alloy are β-Al_5FeSi_2 or α-$Al_{12}Fe_3Si$. Due to atomic radius similarities between Mn, Cr and Fe. Manganese and chromium can substitute places with Fe in the lattice. Therefore, stabilized phases like α-$Al_{12}(FeMn)_3Si$ or α-$Al_{12}(FeCr)_3Si$ - together called Al_{12}(Fe, Mn, Cr)$_3$Si, are formed [111–113]. EDS map of individual elements demonstrate existence of Mn in the Si-rich phase, see Figure 5.3. EPMA measurements in Figure A.3 confirms our hypothesis.

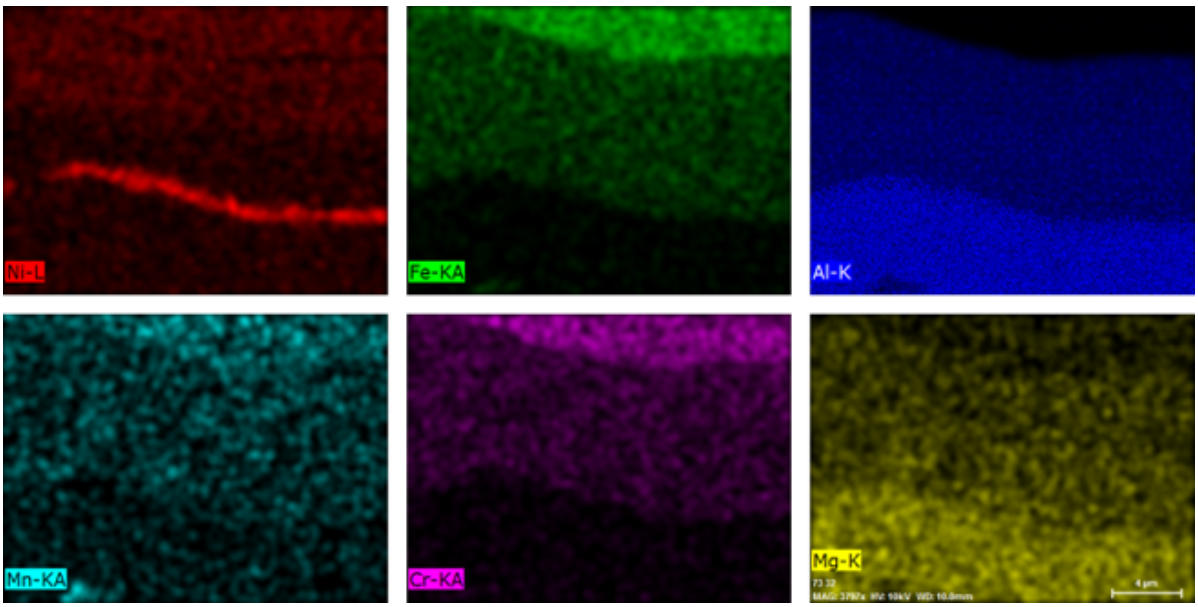

Figure 5.3.: EDS map of the interface in 316-6082-550C-180min. From upper left to right: Ni, Fe, and Al. Bottom left to right: Mn, Cr and Mg

Nanoindentation measurements in Figure 4.47 gives us average hardness value of the $FeAl_3$-like phase at 8.4 GPa and for Fe_2Al_5 phase: 9.5 GPa. We have considered points 6 to 8 in Figure B.1b for the probable locations for the Fe_2Al_5 phase and points 9 to 11 for the $FeAl_3$ phase, since it lies adjacent to Al-interface. Our result is somewhat closer to the values found in literature, see Table 5.1. Technically, on a closer look points 9 to 11 also lie at the Fe_2Al_5 phase.

Figure 5.4 shows the plot of IML thickness vs. $\sqrt{(t)}$ to demonstrate the growth kinetics of the four sample combinations. The growth constant for each combination are as follows:

355-5083 $k = 0.24\,\mu m/s^{1/2}$ at 450 °C

355-6083 $k = 0.11\,\mu m/s^{1/2}$ at 500 °C. Only two points

316-5083 $k = 0.06\,\mu m/s^{1/2}$ at 500 °C

316-5083 $k = 0.09\,\mu m/s^{1/2}$ at 550 °C

The values obtained for the growth constant correlates with our observations. Al-alloy with high Si concentration impeded IML thickness growth. Alloying elements in Steel grades helped in suppressing IML thickness growth. Furthermore, since the growth constant is dependent on temperature, it seems to increase at higher temperatures, slightly.

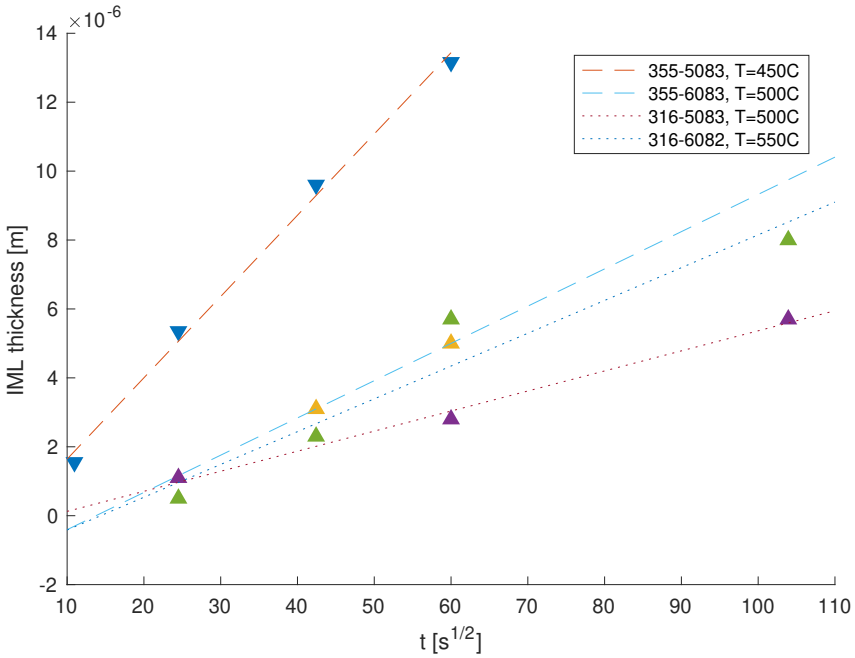

Figure 5.4.: Plot of IML thickness vs. $\sqrt{t}$ of four material combinations. The x-axis has units of $/s^{1/2}$

Chapter 6.

Conclusion

In this study, composites of steel and aluminium alloys were heat treated with different durations to investigate intermetallic compound formation at the interface. Four types of combinations were investigated: 355-5083, 355-6082, 316-5083, and 316-6082. The results from heat treatment experiments are as following:

- The intermetallic phases detected were in the sequence of Al-/ $FeAl_3$ / Fe_2Al_5 /-St, as predicted by the phase diagram and the Walser-Bene model. $FeAl_3$ was first formed at the interface towards Al, as a minor phase. Fe_2Al_5 was found to be the major phase in all the samples.
- The intermetallic layer formed at the lowest temperature was observed in the sample 355-5083. The low Si content in 5083 made combinations with this alloy susceptible for intermetallic compound formation in all temperatures and durations. The influence of Si on retardation of intermetallic layer growth was observed.
- Growth constant calculated for the sample 355-5083 at 450 °C was compared with the values found in the literature.
- Segregation of Mg was observed towards the Al-interface at temperatures over 450 °C in 355-5083 combinations. The literature on Mg segregation mechanism was found to be scarce.
- Nanoindentation measurement for the hardness of the sample 355-5083 was found to be well below the values observed in the literature. For 316-6082, the hardness measurements were found well within the margin.
- In samples 316-5083 heat-treated at 500C, four phases were observed. A Mg phase (or segregation of Mg) adjacent to the steel layer, Cr and Ni enrichment at the Al-interface and Si, Cr and Mn rich phase were observed.
- No apparent effect of the total reduction of the samples under rolling was found to be influencing formation of IML
- For the characterization of IMCs, EDS measurements were not found to be very exact. Significant compositional errors were found for some samples, due to thin IML

thickness. On the other hand, EPMA analysis was satisfactory. Characterization of IMCs through EBSD, TEM and Atom Probe Tomography would be advantageous.

- Some new postulates were made on the type of IMC found in 316-5083 and 316-6082 samples, based on values provided by EDS measurement. They were based on thermodynamic data and some limited literature.

Appendix A.

EPMA

A.1. 355-5083-450C-60min

The EPMA results for 355-5083-450C-60min mapping and line scan.

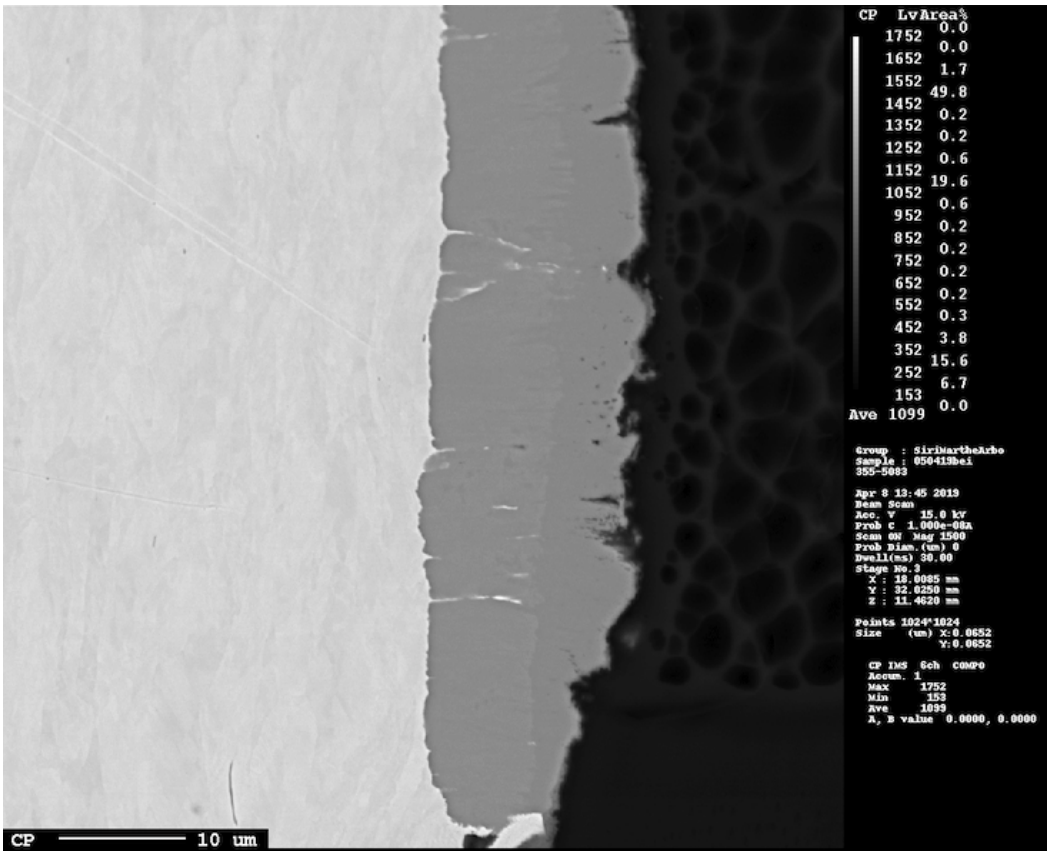

(a)

Figure A.1.: Results obtained from EPMA analysis of sample 355-5083-450C-60min. **(a)** the area for line scan

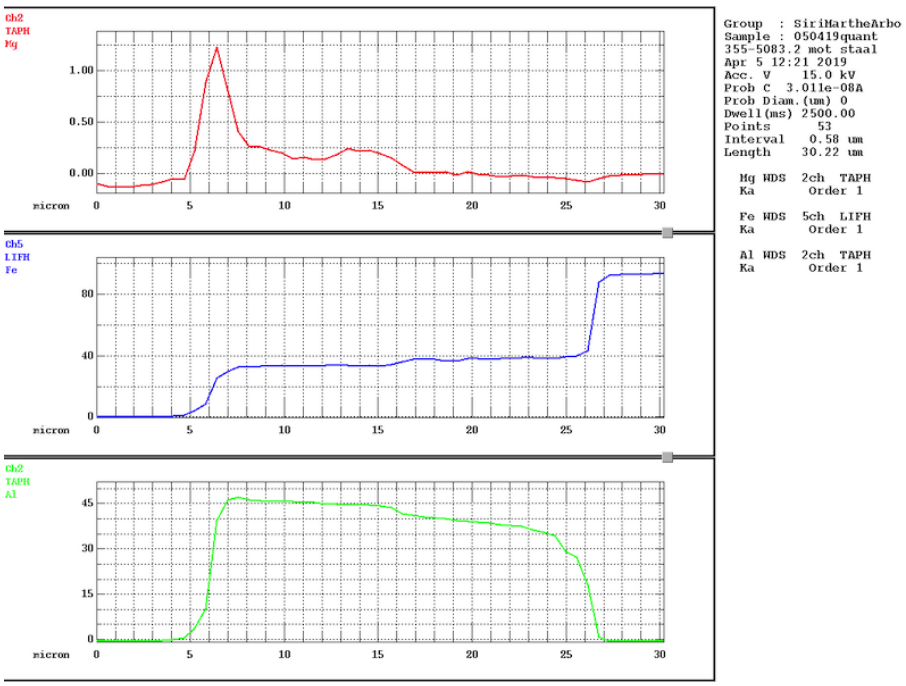

(b)

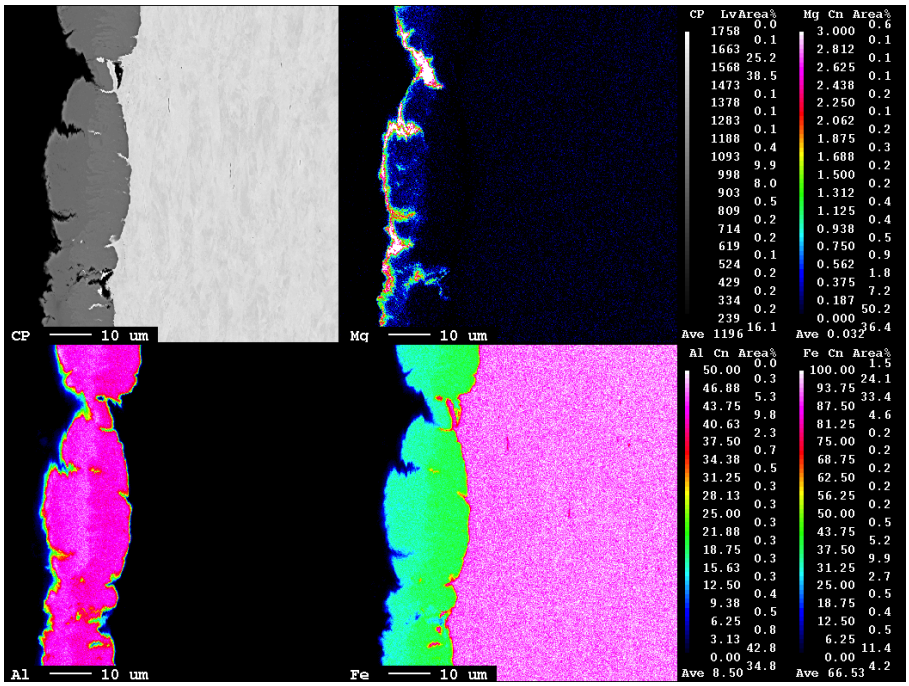

(c)

Figure A.1.: (b) line scan at the middle of the sample from right to left. y-axis is in weight percent **(c)** Mapping of interface showing Mg segregation towards Al-interface.

A.2. 355-6082-550C-60min

The EPMA results for 355-6082-550C-60min line scan.

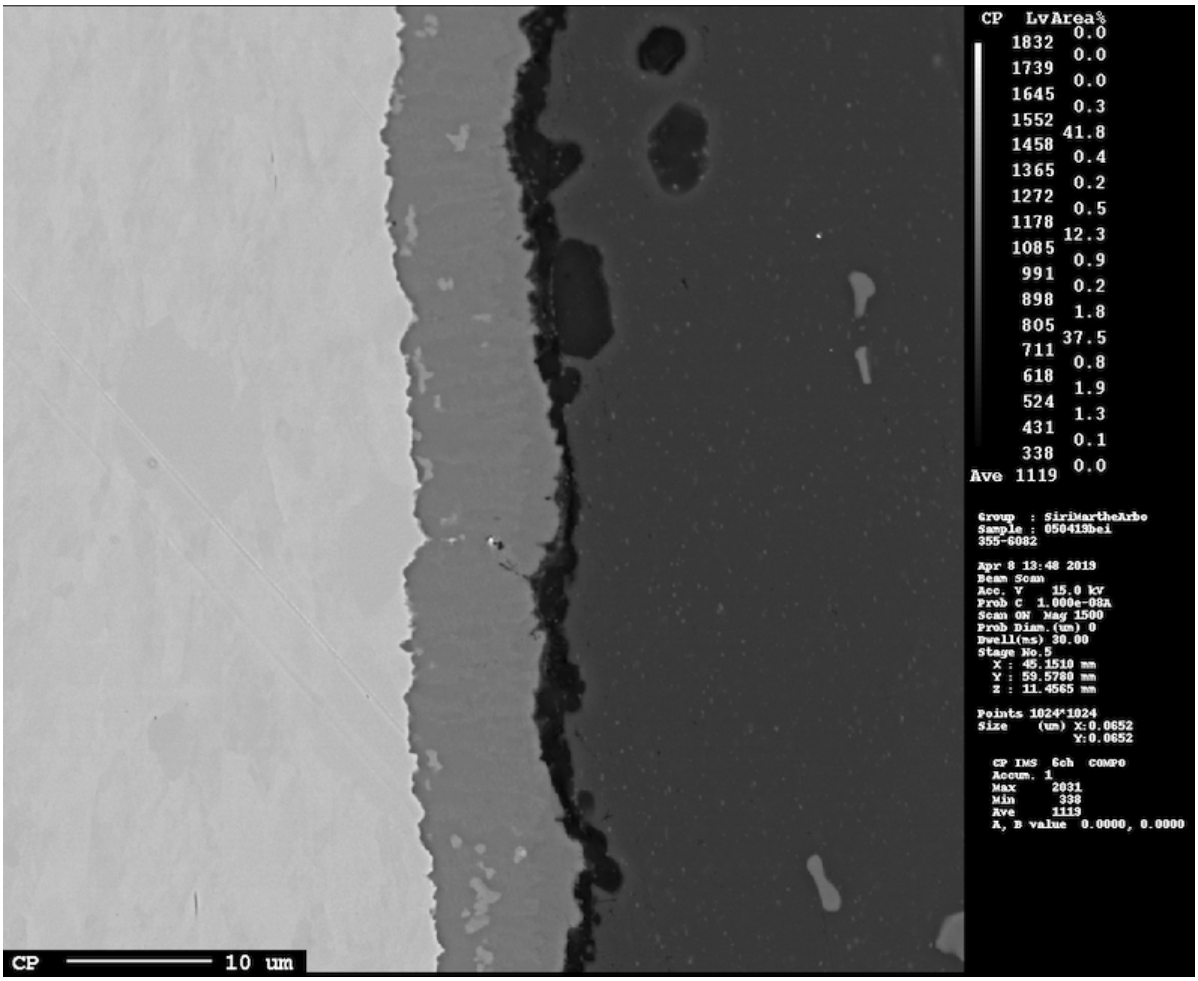

(a)

Figure A.2.: a Micrograph of the 355-6082-550C-60min interface

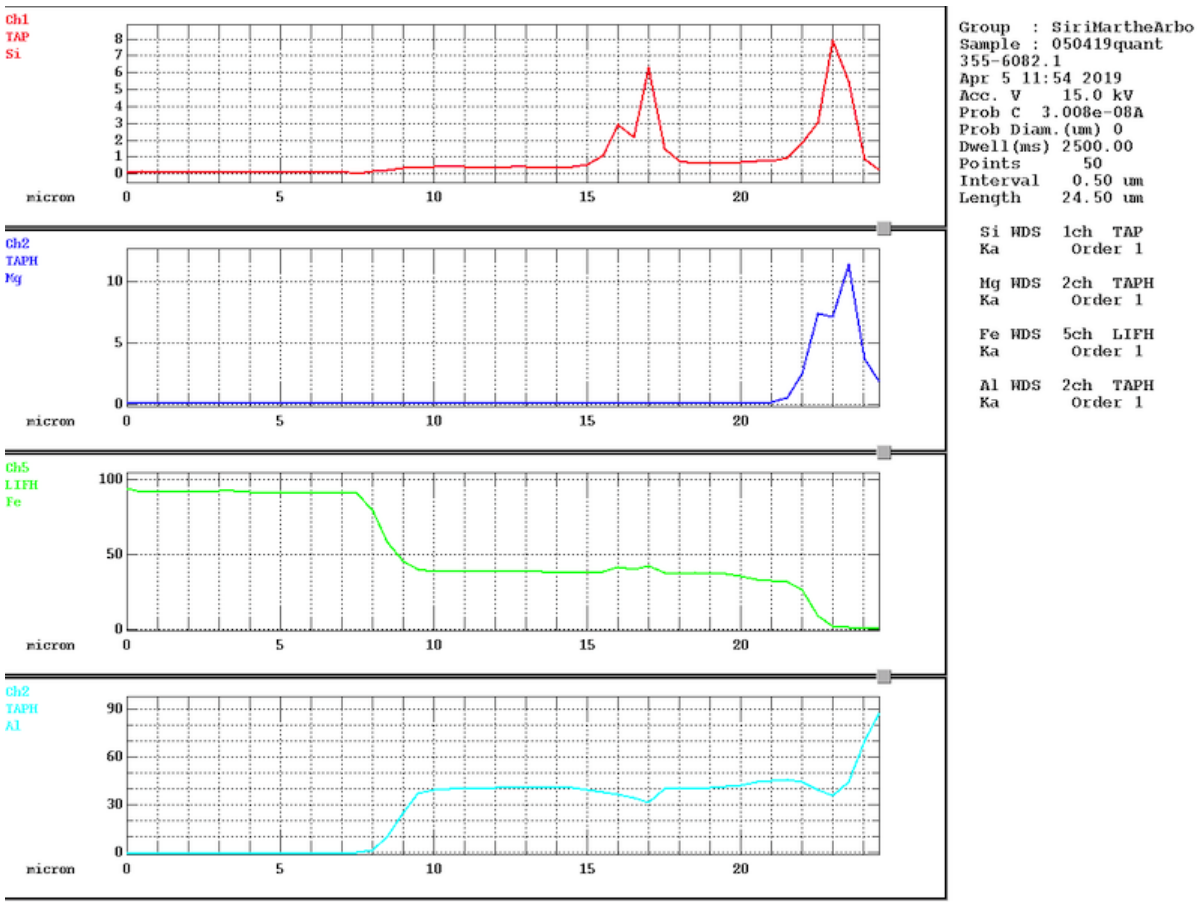

(b)

Figure A.2.: (b) line scan taken at the middle of the sample from left to right. y-axis is in weight percent

A.3. 316-5083-550C-60min

The EPMA results for 316-5083-550C-60min line scan.

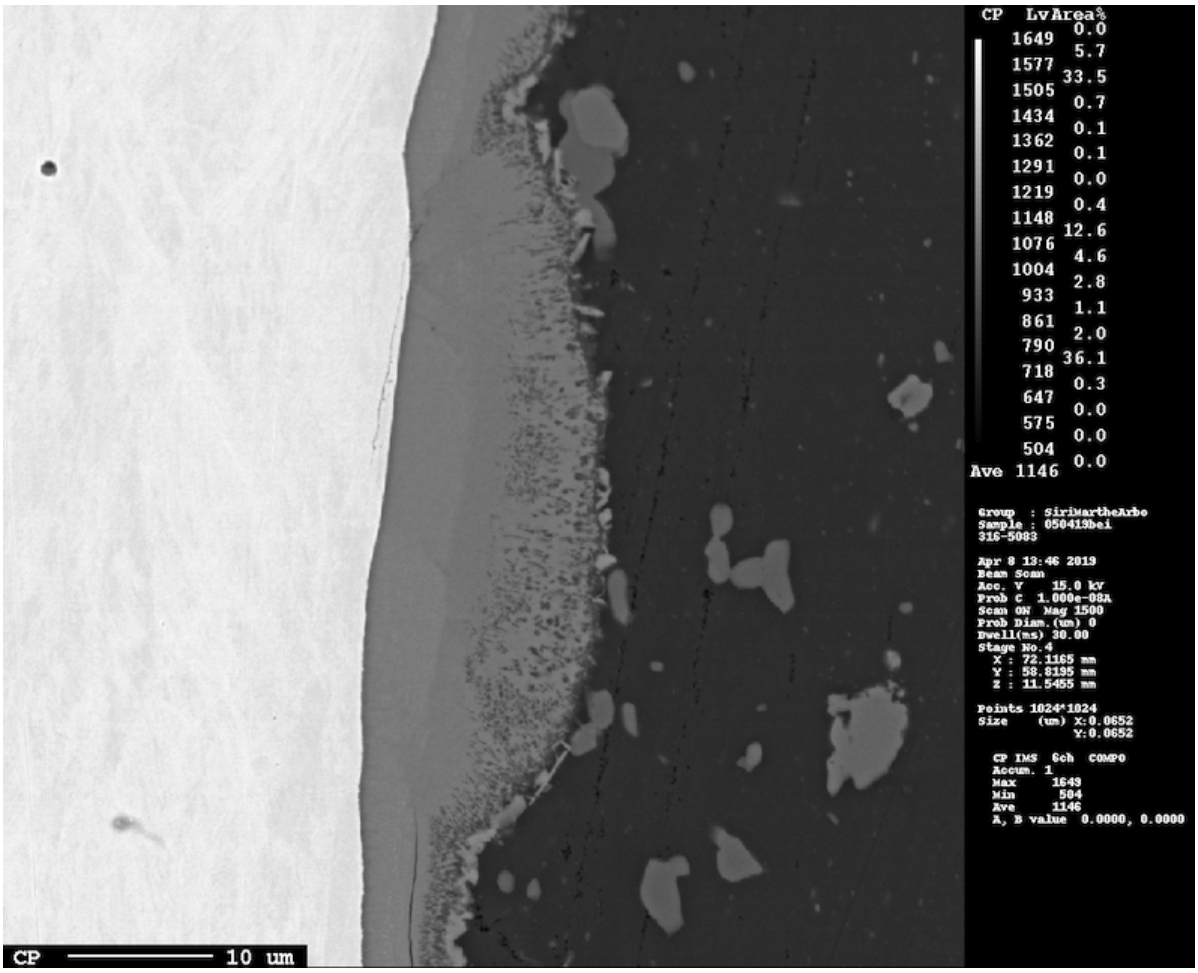

(a)

Figure A.3.: a Micrograph of the 316-5083-550C-60min interface

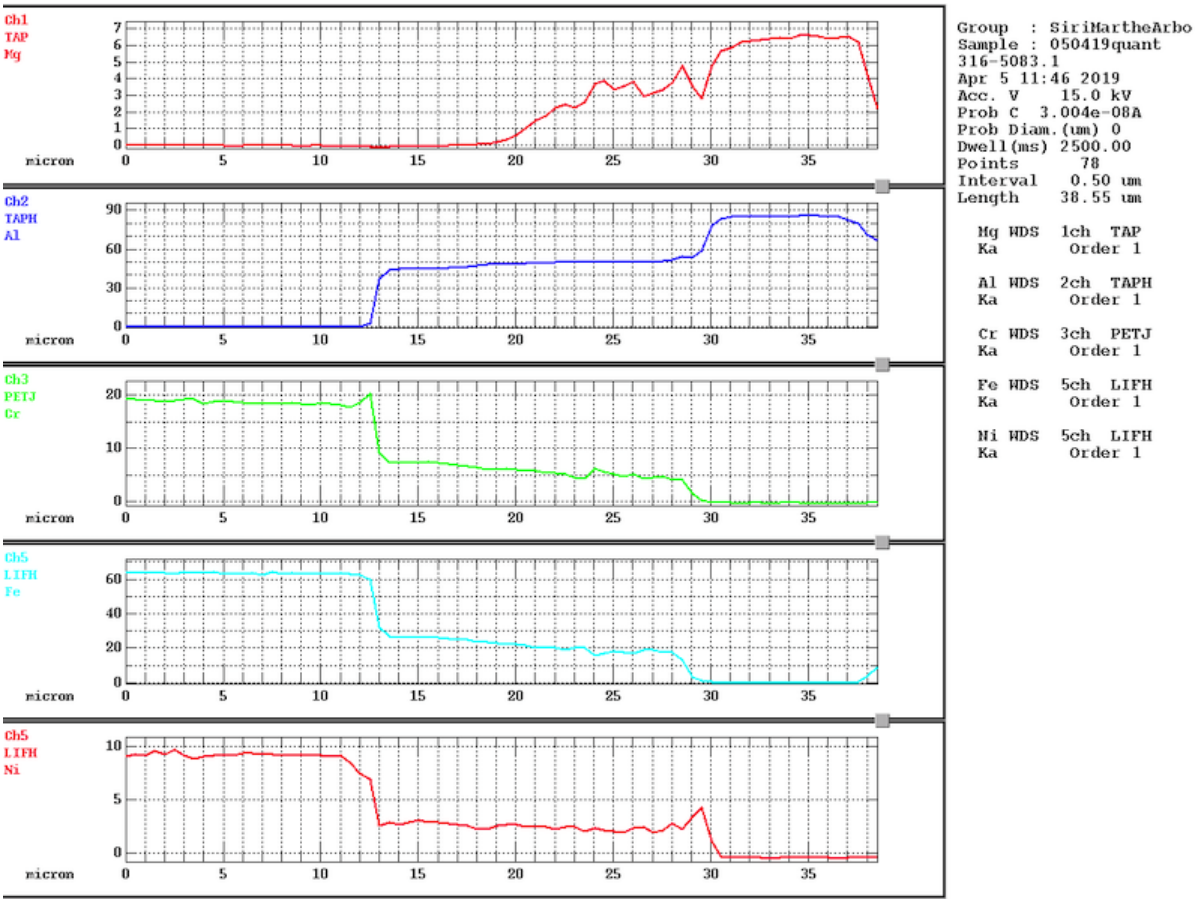

(b)

Figure A.3.: (b) line scan taken at the middle of the sample from left to right. y-axis is in weight percent

A.4. 316-6082-550C-180min

The EPMA results for 316-6082-550C-180min line scan.

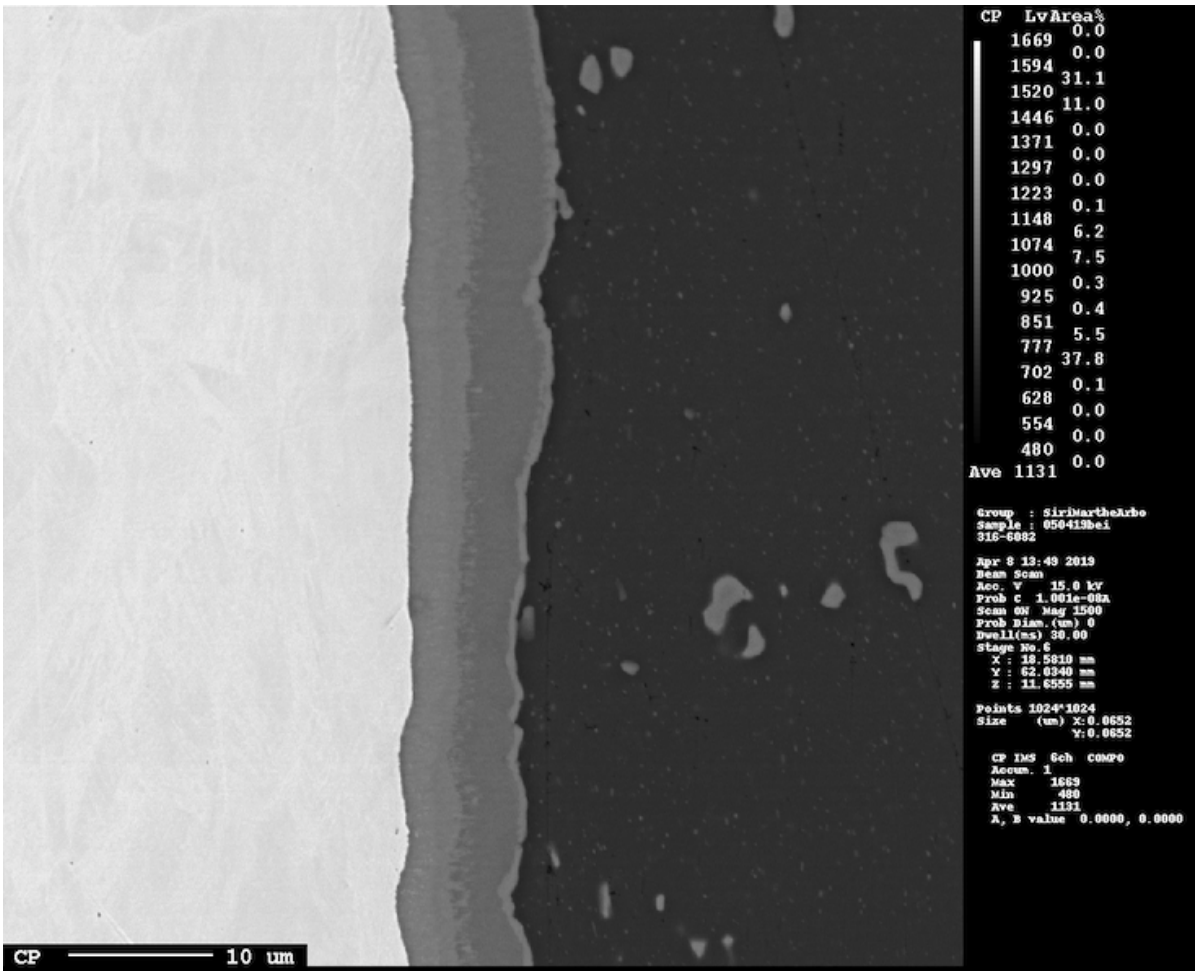

(a)

Figure A.4.: a Micrograph of the 316-6082-550C-180min interface

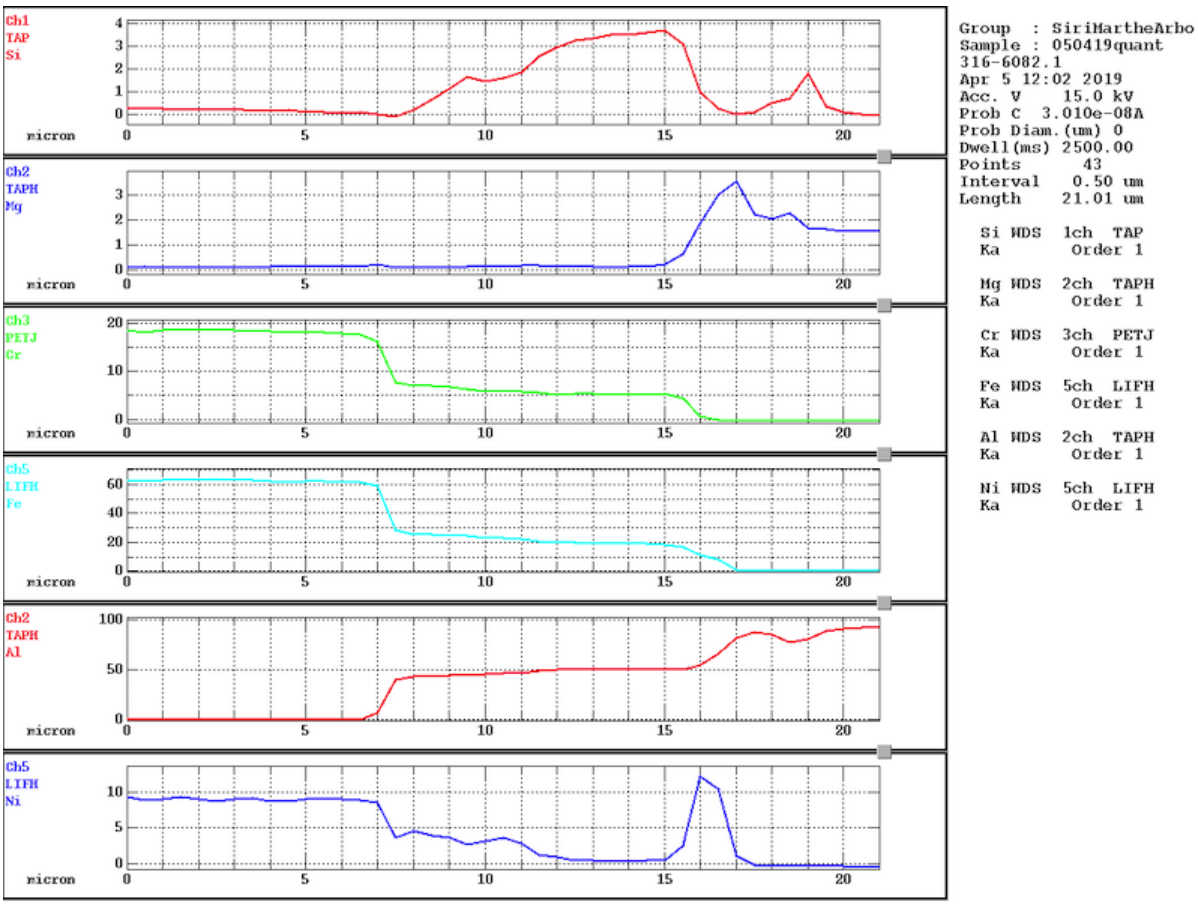

(b)

Figure A.4.: (b) line scan taken at the middle of the sample from left to right. y-axis is in weight percent

Appendix B.

Nanoindentation

Nanoindentation points marked at the interface of 355-5083-450C-30min and 316-6082-550C-60min together with the load function of the indenter is presented in Figure B.1.

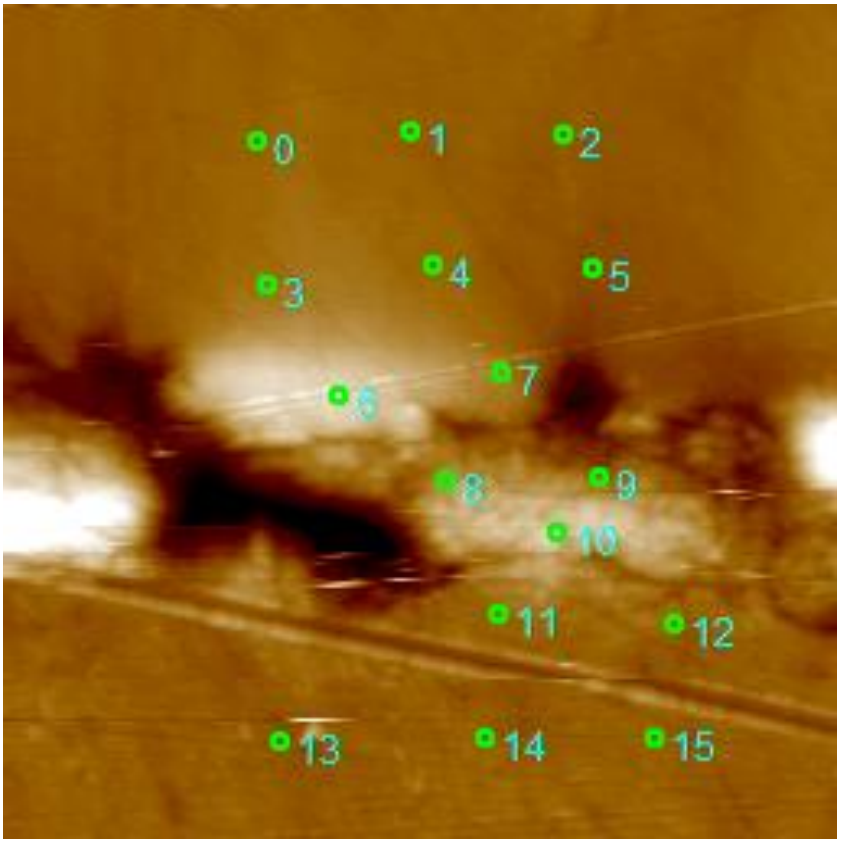

(a)

Figure B.1.: (a) Nanoindentation points at the interface of 355-5083-450C-30min

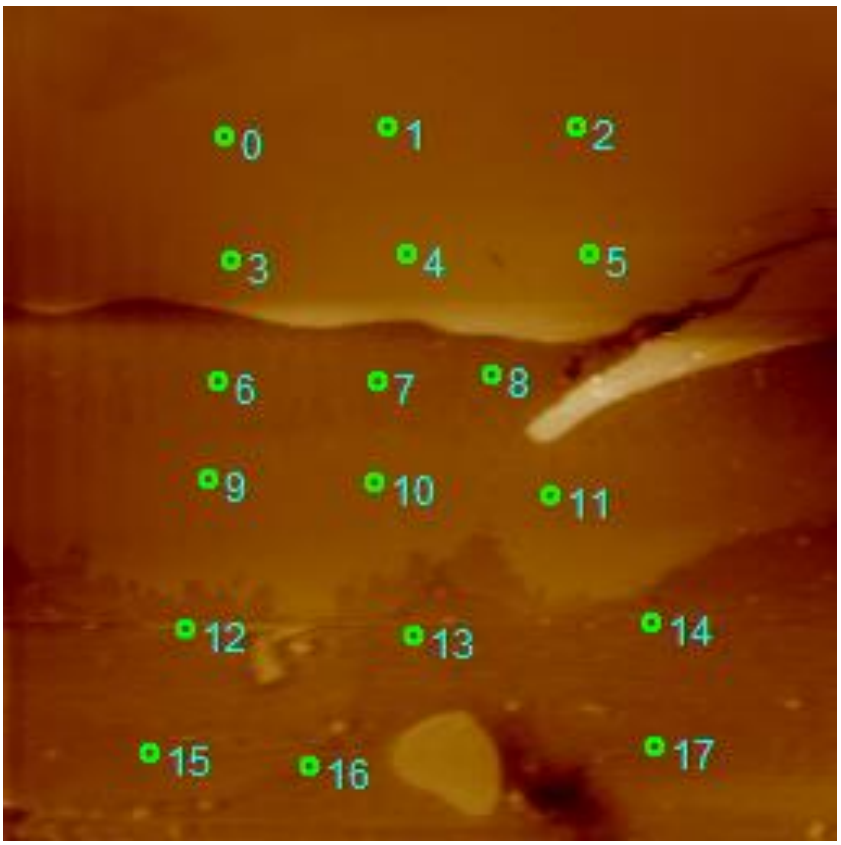

(b)

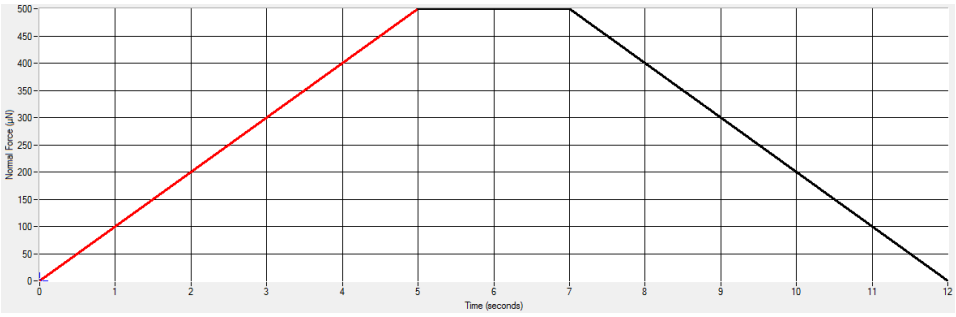

(c)

Figure B.1.: (b) nanoidentation points at the interface of 316-6082-550C-60min **(c)** load function of the indenter.

Bibliography

[1]F. Kümmel et al., "High lightweight potential of ultrafine-grained aluminum/steel laminated metal composites produced by accumulative roll bonding", Advanced Engineering Materials **21** (2019) (cit. on p. 1).

[2]S. A. David and M. Santella, *Physical Metallurgy and processing of Intermetallic Compounds*, edited by N. Stoloff and V. Sikka (Chapman and Hall, 1996) (cit. on p. 1).

[3]Wickeder-Group, *Clad Metal sheets*, Webpage, Mar. 2019 (cit. on p. 1).

[4]R. Messler, *Principles of Welding: Processes, Physics, Chemistry, and Metallurgy* (Wiley India Pvt. Limited, 2004) (cit. on pp. 1, 3).

[5]L. Li, K. Nagai and F. Yin, "Progress in cold roll bonding of metals", Science and Technology of Advanced Materials **9**, 023001 (2008) (cit. on pp. 1, 3).

[6]A. A. Shirzadi, "Diffusion bonding aluminium alloys and composites: new approaches and modelling", PhD thesis (King's College, Cambrige, 1997) (cit. on p. 1).

[7]J. G. Lenard, *Primer on Flat Rolling*, 2nd ed. (Elsevier, Oxford, 2014) (cit. on pp. 1, 3 sq.).

[8]W. Zhang and N. Bay, "A numerical model for cold welding of metals", CIRP Annals **45**, 215 –220 (1996) (cit. on p. 1).

[9]F. C. Campbell, *Joining : Understanding the Basics.* (ASM International, 2011) (cit. on pp. 3 sqq.).

[10]H. Mohamed and J. Washburn, "Mechanism of solid state pressure welding", Welding Journal **54** (1975) (cit. on pp. 3 sqq.).

[11]V. Borovikov et al., "Effect of Stacking Fault Energy on Mechanism of Plastic Deformation in Nanotwinned FCC Metals", Modelling Simul. Mater. Sci. Eng. **23** (2015) (cit. on p. 5).

[12]N. Najafzadeh, "Microstructural Analysis of Accumulative Roll-Bonded Aluminium ", PhD thesis (The University of New South Wales, 2016) (cit. on p. 5).

[13]R. Jamaati and M. R. Toroghinejad, "Influence of stacking fault energy on the grain size of fcc metals fabricated by accumulative roll bonding process", Advanced Materials Research **1064**, 131–137 (2014) (cit. on p. 5).

[14]L. da Silva et al., "A review of the cold roll bonding of AlSn alloy/steel bimetal strips", METAL 2014 - 23rd International Conference on Metallurgy and Materials, Conference Proceedings, 274–284 (2014) (cit. on p. 5).

[15]R Jamaati and M. R. Toroghinejad, "Cold roll bonding bond strengths: review", Materials Science and Technology **27**, 1101–1108 (2011) (cit. on p. 5).

[16]A. Bagheri, M. R. Toroghinejad and A. Taherizadeh, "Effect of Roughness and Surface Hardening on the Mechanical Properties of Three-Layered Brass/IF Steel/Brass Composite", Transactions of the Indian Institute of Metals **71**, 2199–2210 (2018) (cit. on p. 5).

[17]H. Solhaug, "Thermomechanical processing of an AA6082 - IF steel cold roll bonded composite material", MA thesis (Norwegian University of Science and Technology, 2017) (cit. on pp. 5 sq., 18).
[18]M. S. A. Nezhad and A. H. Ardakani, "A study of joint quality of aluminum and low carbon steel strips by warm rolling", Materials & Design **30**, 1103 –1109 (2009) (cit. on p. 5).
[19]S. M. Arbo et al., "Influence of thermomechanical processing sequence on properties of AA6082-IF steel cold roll bonded composite sheet", Procedia Manufacturing **15**, 152 –160 (2018) (cit. on pp. 6, 9 sq., 67).
[20]R. Jamaati and M. R. Toroghinejad, "Investigation of the parameters of the cold roll bonding (CRB) process", Materials Science and Engineering: A **527**, 2320 –2326 (2010) (cit. on p. 6).
[21]H. D. Manesh and A. K. Taheri, "The effect of annealing treatment on mechanical properties of aluminum clad steel sheet", Materials & Design **24**, 617 –622 (2003) (cit. on p. 6).
[22]U. Mizutani, *Hume-rothery rules for structurally complex alloy phases*, 1st (CRC Press, 2010) (cit. on p. 6).
[23]J.-S. Wang, "Why l12 intermetallics are brittle and how to make them ductile", Journal of Computer-Aided Materials Design **4**, 157–163 (1998) (cit. on p. 6).
[24]ASM International Handbook Committee, "Properties and Selection: Nonferrous Alloys and Special-Purpose Materials", in , Vol. 2 (ASM International, 1990) Chap. 45.8 Intermetallic-Matrix Composites (cit. on p. 6).
[25]Y. Harada et al., "New crystal structure maps for intermetallic compounds", J. Phys.: Condens. Matter **9**, 8011–8030 (1997) (cit. on p. 7).
[26]M. Yildirim, "Design and development of iron aluminium intermetallic compounds for structural applications at high temperatures", MA thesis (Middle East Technical University, 2014) (cit. on p. 7).
[27]L. H. Shah and M. Ishak, "Review of Research Progress on Aluminum–Steel Dissimilar Welding", Materials and Manufacturing Processes **29**, 928–933 (2014) (cit. on p. 7).
[28]L. Agudo et al., "Intermetallic fexaly-phases in a steel/al-alloy fusion weld", Journal of Materials Science **42**, 4205–4214 (2007) (cit. on p. 7).
[29]R. Mitra, *Intermetallic matrix composites: properties and applications*, Woodhead Publishing Series in Composites Science and Engineering (Elsevier Science, 2017) (cit. on p. 7).
[30]H. Shahverdi et al., "Microstructural analysis of interfacial reaction between molten aluminium and solid iron", Journal of Materials Processing Technology **124**, 345 –352 (2002) (cit. on pp. 7, 63).
[31]H. Baker and H. Okamoto, "ASM Handbook - Alloy Phase Diagrams", in , Vol. 3 (ASM International, 1992) Chap. 2.6.60 Al-Fe (cit. on p. 7).
[32]J. Davis, "Metals Handbook", in , 2nd (ASM International, 1998) Chap. 85.3 Titanium Aluminides, p. 686 (cit. on p. 8).
[33]J. Davis, "Alloying - Understanding the Basics", in (ASM International, 2001) Chap. 15.3 Iron Aluminides, p. 343 (cit. on p. 8).
[34]C. Schön, "Thermodynamics and physical properties of ternary iron aluminides", in (Nov. 2015) (cit. on p. 8).

[35]H. Springer et al., "On the formation and growth of intermetallic phases during interdiffusion between low-carbon steel and aluminum alloys", Acta Materialia **59**, 1586–1600 (2011) (cit. on pp. 8 sq., 64).
[36]Y. Liu et al., "Mechanical properties and electronic structures of fe-al intermetallic", Physica B: Condensed Matter **506**, 1–11 (2017) (cit. on p. 8).
[37]H. Springer et al., "Influence of intermetallic phases and kirkendall-porosity on the mechanical properties of joints between steel and aluminium alloys", Materials Science and Engineering: A **528**, 4630 –4642 (2011) (cit. on pp. 8, 64).
[38]Z. Silvayeh et al., "Calculation of the Intermetallic Layer Thickness in Cold Metal Transfer Welding of Aluminum to Steel", Materials **12**, 35 (2018) (cit. on pp. 8, 64).
[39]B. Lemmens et al., "Atom probe tomography of intermetallic phases and interfaces formed in dissimilar joining between Al alloys and steel", Materials Characterization **120**, 268–272 (2016) (cit. on pp. 8 sq., 66 sq.).
[40]V. I. Dybkov, "Interaction of 18cr-10ni stainless steel with liquid aluminium", Journal of Materials Science **25**, 3615–3633 (1990) (cit. on pp. 8, 69).
[41]A Bouayad et al., "Kinetic interactions between solid iron and molten aluminium", Materials Science and Engineering: A **363**, 53 –61 (2003) (cit. on p. 8).
[42]K. Bouché, F. Barbier and A. Coulet, "Intermetallic compound layer growth between solid iron and molten aluminium", Materials Science and Engineering **A249**, 167–175 (1998) (cit. on pp. 8, 64).
[43]A. Furuto and M. Kajihara, "Numerical analysis for kinetics of reactive diffusion controlled by boundary and volume diffusion in a hypothetical binary system", MATERIALS TRANSACTIONS **49**, 294–303 (2008) (cit. on p. 9).
[44]I. Kwiecien et al., "Growth kinetics of the selected intermetallic phases in ni/al/ni system with various nickel substrate microstructure", Nanomaterials **9** (2019) (cit. on p. 9).
[45]A. K. Kurakin, "Mechanism of the influence of silicon on the processes of the reaction diffusion of iron in aluminium", Physics of Metals and Metallography (Fiz. Metal. Metalloved.) **30**, 105–110 (1970) (cit. on pp. 9, 67).
[46]N. Takata et al., "Morphology and formation of Fe–Al intermetallic layers on iron hot-dipped in Al–Mg–Si alloy melt", Intermetallics **54**, 136–142 (2014) (cit. on pp. 9, 63).
[47]K. Li et al., "Effect of Si on the growth of Fe-Al intermetallic layer in Zn-11%Al-3%Mg coating", Surface and Coatings Technology **306**, Developments in Galvanic and Related Coatings, 390 –396 (2016) (cit. on pp. 9, 67).
[48]F.-C. YIN et al., "Effect of si on growth kinetics of intermetallic compounds during reaction between solid iron and molten aluminum", Transactions of Nonferrous Metals Society of China **23**, 556–561 (2013) (cit. on pp. 9, 67).
[49]B. Liu, Q. Yang and Y. Wang, "Intereaction and intermetallic phase formation between aluminum and stainless steel", Results in Physics **12**, 514–524 (2019) (cit. on pp. 9, 63, 65).
[50]M. Akdeniz and A. Mekhrabov, "The effect of substitutional impurities on the evolution of Fe-Al diffusion layer", Acta Materialia **46**, 1185 –1192 (1998) (cit. on p. 10).
[51]B. Dangi, T. W. Brown and K. N. Kulkarni, "Effect of silicon, manganese and nickel present in iron on the intermetallic growth at iron - aluminum alloy interface", Journal of Alloys and Compounds **769**, 777–787 (2018) (cit. on pp. 10 sq., 64, 67).

[52]R. Fleischer, "Substitutional solution hardening", Acta Metallurgica **11**, 203 –209 (1963) (cit. on p. 11).
[53]U. F. Kocks, "Kinetics of solution hardening", Metallurgical Transactions A **16**, 2109–2129 (1985) (cit. on p. 11).
[54]A. Poznak, D. Freiberg and P. Sanders, "Automotive wrought aluminium alloys", in *Fundamentals of aluminium metallurgy*, edited by R. N. Lumley (Woodhead Publishing, 2018), p. 345 (cit. on pp. 11, 13).
[55]R. Ambriz and D. Jaramillo, "Mechanical behavior of precipitation hardened aluminum alloys welds", in *Light metal alloys applications*, edited by W. A. Monteiro (IntechOpen, Rijeka, 2014) Chap. 2 (cit. on p. 12).
[56]J. Davis, *Corrosion of aluminum and aluminum alloys* (ASM International, 1999) (cit. on pp. 12 sq.).
[57]F. Cardarelli, *Materials handbook: a concise desktop reference*, 2nd (Springer London, 2000) (cit. on p. 12).
[58]MatWeb - Material Property Data, *Aluminum alloy heat treatment temper designations*, Webpage (cit. on p. 12).
[59]V. S. Zolotorevsky, N. A. Belov and M. V. Glazoff, *Casting aluminum alloys* (Elsevier, 2007) (cit. on p. 13).
[60]J. Yan et al., "Improve sensitization and corrosion resistance of an Al-Mg alloy by optimization of grain boundaries", Scientific reports **6** (2016) (cit. on p. 13).
[61]D. S. D'Antuono, "β Phase Growth and Precipitation in the 5xxx Series Aluminum Alloy System", PhD thesis (Drexel University, 2017) (cit. on p. 13).
[62]T. Materia, "Precipitation hardening of aluminum alloys", Total Materia (2018) (cit. on pp. 13 sq.).
[63]A. P. Ratvik, *Light metals*, The Minerals, Metals and Materials Series (Springer, Cham, Germany, 2017) (cit. on p. 13).
[64]G. Sha, R. Marceau and S. Ringer, "12 - Precipitation and solute clustering in aluminium: advanced characterisation techniques", in *Fundamentals of aluminium metallurgy*, edited by R. Lumley (Woodhead Publishing, 2011), pp. 345 –366 (cit. on pp. 13 sq.).
[65]H. M. Cobb, ed., *Dictionary of metals* (ASM International, 2012) (cit. on p. 14).
[66]M. van Huis et al., "Phase stability and structural features of matrix-embedded hardening precipitates in Al–Mg–Si alloys in the early stages of evolution", Acta Materialia **55**, 2183 –2199 (2007) (cit. on p. 14).
[67]E. Sverdrup, "Intermetallic growth and metallurgical bonding in cold roll-bonded steel-aluminium laminates", MA thesis (Norwegian University of Science and Technology, 2018) (cit. on pp. 15, 18).
[68]Aalco, "Aluminium alloy composition", Aalco Metals Ltd (2018) (cit. on p. 16).
[69]Ø. Ryen, "Work hardening and mechanical anisotropy of aluminium sheets and profiles", PhD thesis (Norwegian University of Science and Technology, 2003) (cit. on p. 18).
[70]J. I. Goldstein et al., *Scanning Electron Microscopy and X-Ray Microanalysis*, 4th (Springer New York, 2018) (cit. on p. 20).
[71]M. Rohde, *Introduction to EDS analysis*, Bruker Nano GmbH (2011) (cit. on p. 20).
[72]CAMECA, "Introduction to EPMA", (2019) (cit. on p. 21).

[73]S. P. Baker et al., "Nanoindentation techniques", in *Encyclopedia of materials: science and technology* (Elsevier, Oxford, 2001), pp. 5908–5915 (cit. on pp. 21, 31).
[74]J. Rong et al., "Growth kinetics and thickness prediction of interfacial intermetallic compounds between solid steel and molten aluminum based on thermophysical simulation in a few seconds", Materials Characterization **132**, 413–421 (2017) (cit. on pp. 63, 67).
[75]P. G. Gonzales-Ormeño, H. M. Petrilli and C. G. Schön, "Ab-initio calculations of the formation energies of BCC-based superlattices in the Fe-Al system", Calphad **26**, 573 – 582 (2002) (cit. on p. 63).
[76]L. Li et al., "Crystallographic features of the primary Al_3Fe phase in as-cast Al–3.31wt% Fe alloy", Journal of Applied Crystallography **43**, 1108–1112 (2010) (cit. on p. 63).
[77]Springer-Materials Database, *FeAl3 (Fe4Al13) Crystal Structure*, edited by P. Villars and K. Cenzual, Online (cit. on p. 63).
[78]A. Van Alboom et al., "Multi-method identification and characterization of the intermetallic surface layers of hot-dip al-coated steel: feal 3 or fe 4 al 13 and fe 2 al 5 or fe 2 al 5+x", Surface and Coatings Technology **324**, 419–428 (2017) (cit. on pp. 63, 67).
[79]Y. K. Kim and S. I. Hong, "Influence of interface structure and stress distribution on fracture and mechanical performance of STS439-Al1050-STS304 clad composite", Materials Science and Engineering A, 35–47 (2019) (cit. on pp. 64, 67).
[80]B. Zhang et al., "Microstructure and mechanical properties of sus304/q235 multilayer steels fabricated by roll bonding and annealing", Materials Science and Engineering: A **740-741**, 92 –107 (2019) (cit. on p. 64).
[81]S. Meco et al., "Design of laser welding applied to T joints between steel and aluminium", Journal of Materials Processing Technology **268**, 132 –139 (2019) (cit. on p. 64).
[82]D. Shin et al., "Formation procedure of reaction phases in al hot dipping process of steel", Metals **8** (2018) (cit. on pp. 64, 67).
[83]M. Kajihara, "Quantitative Evaluation of Interdiffusion in Fe2Al5 during Reactive Diffusion in the Binary Fe-Al System", MATERIALS TRANSACTIONS **47**, 1480–1484 (2006) (cit. on p. 64).
[84]K. Bobzin et al., "Effect of Alloying Elements on Growth Behavior of Intermetallic Compounds at the Cold-Sprayed Coating/Steel Interface During Immersion in Aluminum Melt", International Journal of Metalcasting **12**, 712–721 (2018) (cit. on p. 64).
[85]T. Tsukahara et al., "Mechanical Properties of Fe2Al5 and FeAl3 Intermetallic Phases at Ambient Temperature", Tetsu-to-Hagane **102**, 29–35 (2016) (cit. on p. 65).
[86]N. Chen et al., "Microstructural and mechanical evolution of al/steel interface with fe2al5 growth in resistance spot welding of aluminum to steel", Journal of Manufacturing Processes **34**, 424 –434 (2018) (cit. on p. 65).
[87]M. I. R. Basariya and N. K. Mukhopadhyay, "Structural and mechanical behaviour of al-fe intermetallics", in *Intermetallic compounds - formation and applications* (IntechOpen, 2018) Chap. 5 (cit. on p. 65).
[88]T. Malis and M. C. Chaturvedi, "Grain-boundary segregation in an al-8 wt % mg alloy", Journal of Materials Science **17**, 1479–1486 (1982) (cit. on p. 65).
[89]V. I. Razumovskiy et al., "The effect of alloying elements on grain boundary and bulk cohesion in aluminum alloys: an ab initio study", Scripta Materialia **65**, 926 –929 (2011) (cit. on p. 65).

[90]A. Devaraj et al., "Grain boundary segregation and intermetallic precipitation in coarsening resistant nanocrystalline aluminum alloys", Acta Materialia **165**, 698 –708 (2019) (cit. on p. 65).
[91]X. Sauvage et al., "Grain boundary segregation in ufg alloys processed by severe plastic deformation", Advanced Engineering Materials **14**, 968–974 (2012) (cit. on p. 65).
[92]I. Kenji et al., "Effect of interfacial reaction layer on bond strength of friction-bonded joint of al alloys to steel", JWRI **34** (2005) (cit. on p. 65).
[93]N. Takata et al., "Crystallography of fe2al5 phase at the interface between solid fe and liquid al", Intermetallics **67** (2015) (cit. on pp. 65 sq.).
[94]S. M. Arbo, I. Westermann and B. Holmedal, "Influence of Stacking Sequence and Intermediate Layer Thickness in AA6082-IF Steel Tri-Layered Cold Roll Bonded Composite Sheets", Key Engineering Materials **767**, 316–322 (2018) (cit. on p. 66).
[95]D. Narsimhachary et al., "Mechanical and microstructural characterization of laser weld-brazed AA6082-galvanized steel joint", Journal of Materials Processing Technology **263**, 21 –32 (2019) (cit. on p. 66).
[96]A. Reeb and K. A. Weidenmann, "Influence of heat treatment on microstructure and mechanical properties of the interface in an EN AW-6082/1.4310 composite extrusion", Composite Interfaces **24**, 779–800 (2017) (cit. on p. 66).
[97]C. Theron et al., "First phase formation at interfaces: Comparison between Walser-Bené and effective heat of formation model", Materials Chemistry and Physics **46**, 238 –247 (1996) (cit. on p. 67).
[98]G. Eggeler, W. Auer and H. Kaesche, "On the influence of silicon on the growth of the alloy layer during hot dip aluminizing", Journal of Materials Science **21**, 3348–3350 (1986) (cit. on p. 67).
[99]M. Reza-E-Rabby et al., "Joining thick section aluminum to steel with suppressed feal intermetallic formation via friction stir dovetailing", Scripta Materialia **148**, 63 –67 (2018) (cit. on p. 67).
[100]H. J. Springer, "Fundamental Research into the Role of Intermetallic Phases in Joining of Aluminium Alloys to Steel", PhD thesis (Ruhr-University Bochum, 2011) (cit. on p. 67).
[101]J. E. Nicholls, "Hot-dipped aluminium coatings", Anti-Corrosion Methods and Materials **11**, 16–21 (1964) (cit. on p. 67).
[102]K. Zhang et al., "New evidence for the formation and growth mechanism of the intermetallic phase formed at the al/fe interface", Journal of Materials Research **28**, 3279–3287 (2013) (cit. on p. 67).
[103]G. Ghosh, *Al-Fe-Si (Aluminium - Iron - Silicon)*, edited by G. Effenberg and S. Ilyenko, Online, accessed 2019-06-16 (cit. on pp. 67 sq.).
[104]M. M. Sharma, J. D. Tomedi and T. J. Weigley, "Slow strain rate testing and stress corrosion cracking of ultra-fine grained and conventional Al–Mg alloy", Materials Science and Engineering: A **619**, 35 –46 (2014) (cit. on p. 68).
[105]L. Zhang and Y. Du, "Thermodynamic description of the Al–Fe–Ni system over the whole composition and temperature ranges: Modeling coupled with key experiment", Calphad **31**, 529 –540 (2007) (cit. on p. 68).

[106] A. Szczepaniak, "Investigation of intermetallic layer formation in dependence of process parameters during the thermal joining of aluminium with steel", MA thesis (RWTH Aachen University, 2016) (cit. on p. 69).
[107] S. Cui et al., "A coupled experimental and thermodynamic study of the al-cr and al-cr-mg systems", Journal of Alloys and Compounds **698**, 1038 –1057 (2017) (cit. on p. 69).
[108] F. Barbier, D. Manuelli and K. Bouché, "Characterization of aluminide coatings formed on 1.4914 and 316l steels by hot-dipping in molten aluminium", Scripta Materialia **36**, 425 –431 (1997) (cit. on p. 69).
[109] V. P. Dybkov, *Growth kinetics of chemical compound layers* (Cambridge International Science Publishing, Cambridge, UNITED KINGDOM, 1995) (cit. on p. 69).
[110] G. Vourlias et al., "Reinforcement of al–fe–ni alloys with the in situ formation of composite materials", Journal of Alloys and Compounds **483**, 14th International Symposium on Metastable and Nano-Materials (ISMANAM-2007), 178 –181 (2009) (cit. on p. 69).
[111] M. Cabibbo, "Mechanical Properties and Dislocation Boundary Mechanisms during Equal-Channel Angular Pressing (ECAP)", in *Handbook of mechanical nanostructuring* (John Wiley and Sons, Ltd, 2015) Chap. 7, pp. 143–162 (cit. on p. 70).
[112] G. Mrówka-Nowotnik, J. Sieniawski and M. Wierzbiñska, "Intermetallic phase particles in 6082 aluminium alloy", Archives of Materials Science and Engineering **28**, 69–76 (2007) (cit. on p. 70).
[113] J. Li et al., "Intermetallic phase selection during homogenization for aa6082 alloy", Philosophical Magazine **94**, 830–846 (2014) (cit. on p. 70).

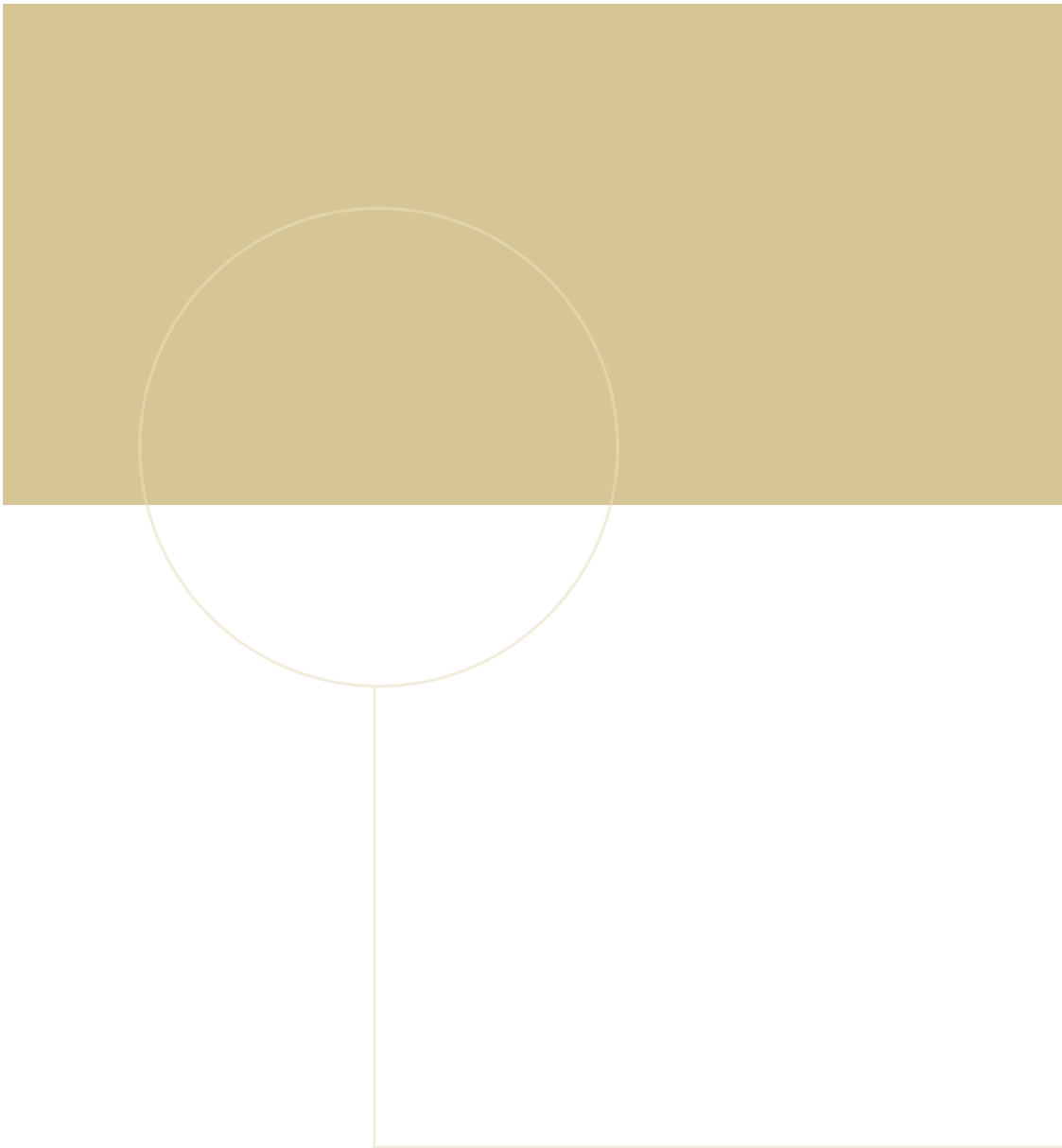

NTNU

Kunnskap for en bedre verden